A Thesis for the Degree of
Doctor of Philosophy

Ray Based Skull Compensation for Transcranial Focused Ultrasound

Changzhu Jin

Department of Ocean System Engineering
GRADUATE SCHOOL
JEJU NATIONAL UNIVERSITY

2017.08

Ray Based Skull Compensation for Transcranial Focused Ultrasound

Changzhu Jin
(Supervised by Professor Dong-Guk Paeng)

A thesis submitted in partial fulfillment of the requirement
for the degree of doctor of philosophy
2017.06
This thesis has been examined and approved by

Thesis director, Il-Hyoung Cho, Professor, Dept. of Ocean System Engineering

---

Dong-Guk Paeng, Professor, Dept. of Ocean System Engineering

Min Joo Choi, Professor, Biomedical Engineering Department School of Medicine

---

Kang-Lyeol Ha, Professor, Dept. of Physics

Juyoung Park, Research Director, Medical Device Development Center

Date _____

Department of Ocean System Engineering
GRADUATE SCHOOL
JEJU NATIONAL UNIVERSITY

Author's address: Dept. of Ocean System Engineering
Jeju National University
102 Jejudaehak-ro
Jeju-si, Jeju Special Self-Governing Province
South Korea
Email: yustchang@jejunu.ac.kr

Supervisor: Dong-Guk Paeng, Ph.D.
Dept. of Ocean System Engineering
Jeju National University
102 Jejudaehak-ro
Jeju-si, Jeju Special Self-Governing Province
South Korea
Email: paeng@jejunu.ac.kr

Reviewers: Il-Hyoung Cho, Ph.D.
Dept. of Ocean System Engineering
Jeju National University
102 Jejudaehak-ro
Jeju-si, Jeju Special Self-Governing Province
South Korea
Email: cho0904@jejunu.ac.kr

Min Joo Choi, Ph.D.
Biomedical Engineering Department School of Medicine
Jeju National University
102 Jejudaehak-ro
Jeju-si, Jeju Special Self-Governing Province
South Korea
Email: mjchoi@jejunu.ac.kr

Kang-Lyeol Ha, Ph.D.
Dept. of Physics
Pukyong National University
45 Yongso-ro, Daeyeon 3(sam)-dong
Nam-gu, Busan
South Korea
Email: hakl@pknu.ac.kr

Juyoung Park, Ph.D.
Medical Device Development Center
Daegu-Gyeongbuk Medical Innovation Foundation
88 dongnae-ro
Dong-gu, Daegu
South Korea
Email: opedoors@gmail.com

ABSTRACT

The numerical compensation of skull bone induced phase aberration significantly recover the focal quality in the transcranial focused ultrasound (TcFUS). In spite of the high accuracy of a full wave simulation approach, it is not feasible for this technology to be adopted in a clinical environment because of long computation time. However, the over-simplified method that was implemented in the current clinical system is incapable of elevating the focal temperature on some of patients with thicker skull because of the lack of acoustic model in the clinical system. This thesis investigates to develop a phase compensation algorithm operating in real-time with reasonable accuracy. A visualization platform utilizing the Open Graphics Library was constructed and the ray method was implemented based on Snell's Law. Three homogeneous layers containing water-skull-brain media were adopted. The registration between the developed software and the clinical system was achieved by localizing the fiducial points embedded in the skull fixed frame. The phase compensation considering refraction was derived by implementing ray method on scanned skull CT volume of two human cadaver skulls. The focal quality was measured by a hydrophone scanning on the focal plane to confirm the results from the developed software with ray method. Finally, the proposed phase correction was verified by the improvement of focal pressure and focal spot location compared to the case without phase correction or with phase correction without refraction accounted. These results will be useful for patient screening, treatment planning, and for during treatment, and analysis even after treatment in a clinical environment as well as transducer design.

TABLE OF CONTENTS

LIST OF FIGURES

Chapter 1

INTRODUCTION

Focused ultrasound (FUS) is an attractive technique to noninvasively treat deeply seated brain tissue leaving collateral structure unaltered. Recently, the thermal ablation treatment for essential tremor was approved by Food and Drug Administration (FDA) in the United States and the treatment is commercially available for patients. The main challenge of this technology is the skull bone, which significantly attenuates and scatters the acoustic beam. In addition to experimental approaches, the numerical simulation studies have been highly investigated in the past twenty years, and the technology becomes more matured. Despite its high accuracy of full wave simulation, the long computation time make these techniques not possible to adopt in clinical environment.

The objective of this study is to develop a fast simulation tool based on ray method to compensate skull-induced aberration with a reasonable accuracy. The overarching theme of the studies was improvement in computation time of the phase correction with a more realistic acoustic ray model than the one implemented in clinical system from empirical approach. In this work, emphasis was placed on two factors: the importance of refraction in the phase correction, the impact of wave velocity in the skull bone to the phase correction.

Chapter 2 provides an overview of the focused ultrasound in the brain applications as well as a review of the compensation studies and the treatment protocol used in clinical environment. In Chapter 3 the registration method used in studies is described. In Chapter 4 to 6, the developed ray based software and the experiment evaluation for phase correction was described. The discussion was described in Chapter 7 and the limitations were listed in Chapter 8. Finally, the conclusions were summarized in Chapter 9 and the applicable future studies were listed in Chapter 10.

1.1. Brain tumor

According to the 2014 World Cancer Report, tumors of the nervous system account for less than 2% of all cancers but have a marked impact on cancer morbidity and mortality [1]. Glioblastomas are the most common and most malignant central nervous system neoplasms, for which the three-year survival rate is less than 3% due to their resistance to radiation and chemotherapy [2]. In addition to primary tumors, studies suggest that brain metastases may develop in up to 19% of lung cancer patients [3], 5% of anywhere [3], and 30% of breast cancer patients [4].

Treatment options for brain tumors include surgical removal or destruction of the tumor using heat, radiotherapy, and chemotherapy, or a combination of two or more of the modalities. For surgical treatment, complete or partial resection of the tumor was performed to remove as much as possible. This has all the risk of open surgery, including bleeding, sensory and motor weakness, and neurologic injury. The radiofrequency ablation is the most commonly used nonsurgical treatment for brain tumors. This stereotactic approach typically uses small lesions, which can limit the accuracy of energy delivery and the effectiveness in larger lesions. It also contains all the risks of invasive procedures. As a non-invasive approach the Gamma Knife is very attractive, but the defect is significant [4-6]. Ionizing radiation is problematic, especially in pediatric patients. There is also a delayed response to treatment, risks to long-term cognitive abilities, and oncologic risks. Chemotherapeutic approaches for treatment of brain cancers have the limitation of inability to deliver drug because the blood-brain barrier prevents the drugs from reaching the cancerous cells.

Ultrasound (US) has several advantages, which make it well suited as diagnostic and therapeutic tool in the human tissue. First, it is nonionizing and can be used non-invasively. As a diagnostic modality, ultrasound equipment is less expensive than Computed Tomography (CT) or Magnetic Resonance Imaging (MRI) devices and has the advantage of portability.

These features make it much more accessible, although its usage in the brain is limited because of the skull bone. However, it is possible to circumvent this limit with the help of advanced electrical control and modern computing power. This will be discussed in the following section.

1.2. Skull bone and mathematical models

1.2.1. Wavelength and skull thickness

The use of ultrasound in the brain presents several unique challenges. The skull bone (see Fig. 1-1) is the biggest barrier of ultrasound in the brain. The skull is comprised of an outer layer of dense cortical bone, which encapsulates a porous trabecular bone center. Skull bone is heterogeneous, and has asymmetric geometry.

The longitudinal speed of sound in the skull bone varies with location and frequency, but is on average approximately 2900 m/s [7, 8] twice that of water. Both speed of sound and attenuation increase with increasing density of the trabecular bone [9]. As a result, sound passing through the skull undergoes inhomogeneous phase shifts, resulting in a defocusing of the beam. Refraction effects arising from non-normal incidence of the ultrasound on the skull further distort the beam profile [10].

In addition to dephasing of the beam, the insertion loss of the skull is very high. This is due to a combination of factors. First, the acoustic impedance of bone differs significantly from both water and soft tissue, resulting in high reflective losses at the tissue-bone interface. The reflective losses can vary from approximately 30-80% at normal incidence [7]. At low frequencies (approximately 500 kHz and lower), reflective losses dominate the total loss observed through human skull bone [7]. At higher frequencies scattering and absorption play a greater role, making it very difficult to transmit frequencies greater than 1 MHz through the

skull bone [7]. The absorptive losses raise an additional concern. Because bone absorbs ultrasound energy at a much higher rate than the surrounding tissue, there are the potential hot spots, particularly at the scalp/bone interface where the ultrasound energy is the highest. In therapeutic processes, this means that the temperature at the bone interface could surpass the temperatures achieved at the transducer focus, even when low frequencies are employed [11].

Distortion of the ultrasound beam increases with frequency as the phase shifts become significant relative to the small wavelengths associated with higher frequencies [10]. Multiple reflections can also occur between the transducer and the skull, contributing to phase distortions at the focus [12]. Thus the skull bone presents a major obstacle for therapeutic ultrasound. The following sections will discuss the techniques to compensate the skull-induced aberration.

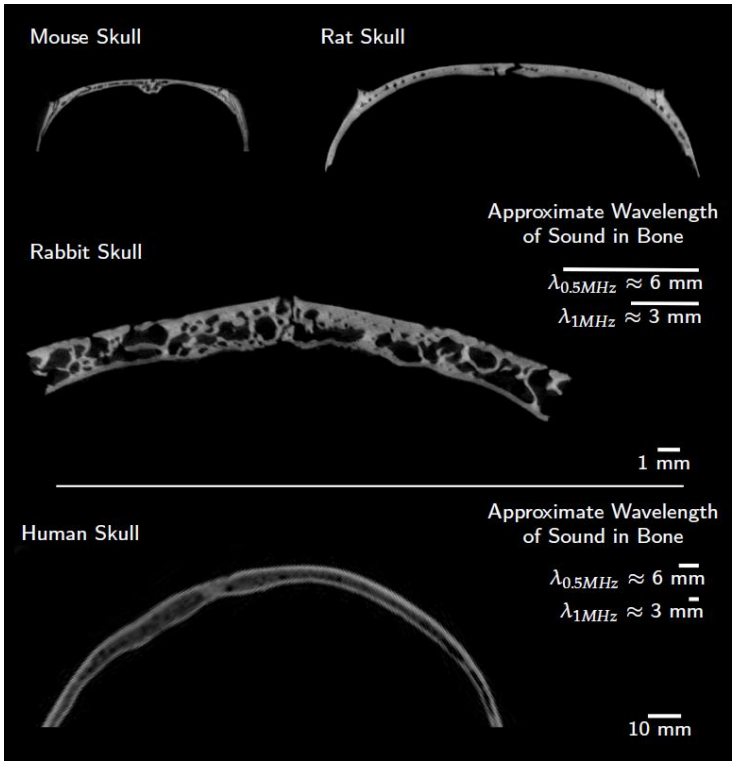

Fig. 1-1 The wave length vs. the skull bone in CT image. The upper half are micro CT images of fragments of mouse, rat and rabbit skulls showing relative sized and lower half is CT image of human skull bone [10].

1.2.2. Mathematical model

The mathematical models describing the propagation of acoustic waves in biological body can be typically categorized into beam model and full-wave models[13]. The derivation of the equation on each model is outside the scope of this section. Thus, a general overview of these mathematical models will be described.

1.2.2.1. Acoustic beam models

The fundamental concept of acoustic beam models is an approximated mathematical depiction of acoustic wave propagation. It is easier to understand and implement numerically than the full-wave models. The simplicity has resulted in a widespread usage and a large number of proposed extensions and improvements to the original models. The Rayleigh-Sommerfeld (RS) integral and the angular spectrum method (ASM) are the typical methods.

Rayleigh-Sommerfeld model

Two fundamental assumptions were adopted in the RS model: that the vibrating surface of the piezoelectric element, is flat and part of an infinite rigid baffle, and that the generated acoustic waves are propagating within an infinite, homogeneous, linear, and isotropic media [14-16]. Prior to the calculation, the surface of any arbitrarily shaped transducer or array is subdivided into a finite number of point sources. In a similar manner, the area or volume of the medium where the acoustic pressure is required is sampled to a number of observation points. The total acoustic pressure at each point can then be calculated as the algebraic sum of all contributions [16, 17]. Some extensions to improve the shortcoming of original RS model were proposed. The Tupholme-Stepanishen model, more commonly known as the impulse-response model [18, 19] was introduced in order to account for diffraction effects at the edges

of the vibrating piezoelectric element which is not feasible with the original RS model. The layer-based inhomogeneity model complements the original RS model with Snell's law, thus permitting for reflection and refraction of the acoustic waves to be taken into account [14]. An alternative formulation of the RS model, named the fast nearfield method (FNM), has been proposed to compute the nearfield region in case of simple transducer shapes. This method simplifies the double integral calculation in the RS model to a fast converging single integral, which is then evaluated using Gauss quadrature [20-22].

Angular spectrum method

The ASM model was first introduced in the field of Fourier optics [23]. This model involves the calculation of an acoustic field's spectral components on an initial plane and propagation of the plane through space by multiplication of each spectral component with an appropriate phase propagation factor [24]. The ASM, usually requires the initial help of the RS model in order to calculate the acoustic wave field from an arbitrary transducer onto a source-plane, and then propagates through its own computation domain. A rapid computation performance could be achieved by permitting of the calculation of the acoustic pressure on an entire plane through a single inverse FFT operation [25]. Various approaches have been proposed to address the majority of limitations restricting the use of the ASM in realistic simulations. The inability to model nonharmonic wavess, e.g., broadband waves or pulses with the ASM could be improved by running separate ASM simulation based on derived frequency components by taking one-dimensional FFT on broadband excitation signals. The summation of each pressure field by an inverse FFT yields the final pressure field [26, 27]. The inability to model wave propagation in heterogeneous media could be overcome by assigning a different speed of sound for each plane where the wave is calculated on [28]. The ASM model does not account for energy loss during its propagation. However, by replacing the real valued wavenumber with a complex number it is possible to account for absorption and attenuation effects [25, 27]. As mentioned

above for RS model, by combining Snell's law with ASM it is possible to account a refraction effect [27]. The foremost drawback of the ASM method is its inability to model wave propagation in a medium exhibiting 3D spatial inhomogeneities. Recently, a hybrid angular spectrum method (hASM) was introduced to address this limitation [25].

1.2.2.2. Full-wave model

Linear acoustic pressure wave equation

In contrast to an acoustic beam model, a full-wave model provides more accurate and realistic depictions of acoustic wave propagation. The most fundamental full-wave model of acoustic wave propagation is the linear acoustic pressure wave equation (LAPWE) which is derived from three fundamental equations of fluid dynamics. These are Euler's equation, the continuity equation and the constitutive equation. The Euler's equation of motion in fluid provides a nonlinear relation between acoustic pressure and particle velocity. The conservation of mass equations, states that the rate of mass flowing into a fixed volume is considered equal to the increase of mass inside the volume. This equation yields a relation between the medium's equilibrium density and the particle velocity. Being a full-wave model, the LAPWE model can account for all the wave propagation phenomena, which include reflection, refraction, diffraction and scattering. However, there are three major limitations of LAPWE. As this model discards high-order terms, nonlinear propagation phenomena cannot be accounted for. Since this model is derived from fluid dynamics equations, the resulting partial differential equation can only account for longitudinal waves. Another downside to the LAPWE is that it does not account for energy absorption [29-31]. The external force, such as mass injection, body force and turbulence sources could be included in source terms and this method is referred to as a convected LAPWE [24, 32]. The lossy LAPWE model which includes lossy term in the right-hand side of the linear continuity equation is used in the

derivation of LAPWE [29]. The shear wave on skull bone and the nonlinearity near the transducer surface could be accounted by adding an additional elastic Westervelt-Lighthill euation (WLE) model [33].

1.3. Transcranial Focused ultrasound (TcFUS)

1.3.1. Treatable neurological disease using TcFUS

Focused ultrasound is a platform technology that can produce multiple biological effects on pathological brain tissue through either thermal or mechanical means. These effects are dependent on the nature of the tissue (e.g. muscle vs. bone) and the ultrasound parameters (power, duration, and mode-continuous versus pulsed) [34]. The applicable mechanisms using focused ultrasound on neurological disease is illustrated in Fig. 1-2. As Fig. 1-2 shows, thermal ablation and neuromodulation could be utilized as therapeutic means to treat many brain diseases. A large and growing number of clinical applications for focused ultrasound are in various stages of research, development and commercialization [34] and they are summarized in Fig. 1-2. The availability of a variety of biomechanisms creates the possibility of treating a variety of disorders. We do not make any attempt to discuss the detail of each mechanism and its biological effects in this study. An overview of focused ultrasound's biological effects is introduced in this reference [34].

Development stage: conceptual → Pre-clinical → Anecdotal → Pilot Trials → Pivotal Trials → Outside US Approvals → FDA Approvals → US Reimbursement

Mechanism	Neurological Disease								
	Alzheimer's Disease	Epilepsy	Essential Tremor	Intracerebral Hemorrhage	Ischemic Stroke	Neuro Muscular Disorders	Neuropathic Pain	Parkinson's Disease	Psychiatric Disorders
Tissue Disruption									
Thermal Ablation		■	■			■	■	■	■
Mechanical Destruction		■							■
Drug Delivery									
Sonoporation								■	■
Increased Vascular Permeability	■							■	
Drug Delivery Vehicles	■							■	
Other Mechanism									
Neuromodulation		■	■			■	■	■	■
Immunomodulation	■								
Clot Lysis				■	■				
Stem Cell Homing	■							■	

Fig. 1-2 The development stage of the focused ultrasound on various neurological diseases and corresponding mechanism.

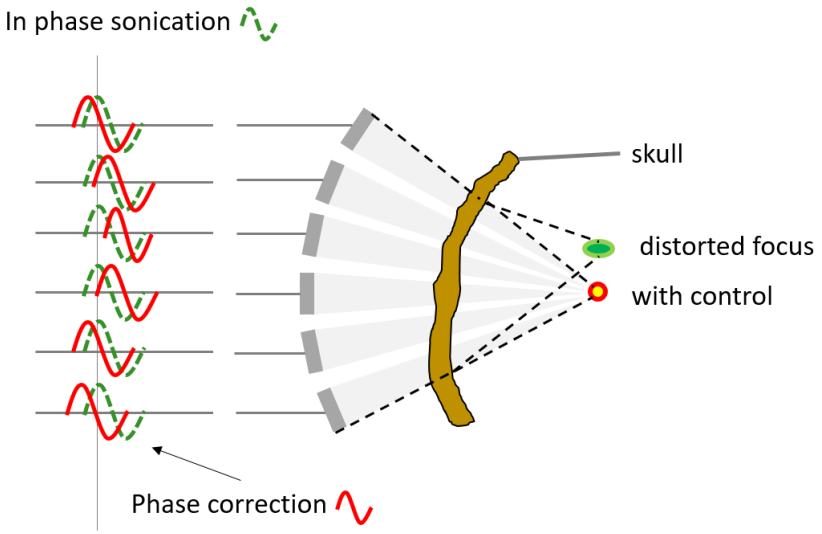

Fig. 1-3 The correction of skull induced phase abberation. The focal spot generated under in phase sonication usualy has a oblique and off-target concentration. A precisely tuned phase delay on each channnel of array transducer could improve the focal spot location.

1.3.2. Focal spot aberration by skull

The foremost barrier when treating the brain with TcFUS is the skull. The complex heterogeneous nature of the skull, which is multi-layered, liquid-filled and porous, causes non-negligible distortion of the focal quality. It is well known that less than 10 percent of the acoustic energy penetrates through the heterogeneous skull structure. Depending on the skull property along the beam path, the wave emitted from each channel in the transducer array experiences a different delay. In this scenario, an in-phase (simultaneous) sonication may cause an unpredictable distortion. As shown in Fig. 1-3, the in-phase sonication through the skull may result in a shifted and distorted focal spot. A nicely tuned phase delay for each channel could shift the focal spot back to targeted location (see Fig.1-3). The technique to refocus the focal spot is called skull compensation or phase correction. Different from other FUS applications in the soft tissue, skull compensation is crucial when treating the diseased target in the brain. In the following section, we will briefly introduce the compensation techniques proposed in the literature.

1.3.3. Skull compensation studies

Focused ultrasound treatment of the brain began in the early 1950s with the precursor works of Professor Fry [35]. Later, FUS treatment with craniotomy was adopted to treat 50 patients affected by Parkinson's Disease in 1960 [36]. However, easier infection during and after this invasive operation makes it inappropriate for multiple target and repetitive treatment. Another option, using lower sonication frequency and longer wavelength, may minimize the interference of the skull refraction. However, lower frequency also decreases the cavitation threshold, thus leaving a strict requirement for cavitation monitoring and control. Moreover, decreasing the frequency results in enlarged and blurred focal volume, which may decrease

heating precision. As the technology has been developed, the scientists found that a solution to these problems is to use large, multi-element transducer arrays with several hundred to over a thousand elements, where each element is driven with an optimized phase and amplitude. The large transducer surface permits the acoustic energy to be distributed on the skull surface, thus diminishing the local deposition of ultrasound energy on the scalp and bone. The ability to drive the transducer elements individually with appropriately corrected phases and amplitudes allows compensation of focal distortion effects [37].

Previously, the compensation study for skull-induced phase correction ranges from purely analytical or numerical calculations of the required aberration corrections to entirely experimental approaches, with a varying degree of invasiveness, usability, and success. Time reversal techniques, like the implanted hydrophone[38-40] and the 'acoustic stars'[41], undoubtedly provide the highest refocusing quality. However, this invasive approach could result in undesirable tissue damage and unlikely to be utilized in clinics for multi-targeting treatment. Analytical calculations or simulations to derive phase and amplitude correction are entirely non-invasive and already being employed on modern TcFUS systems. However, despite their speed and ease of use, the purely analytical methods are inherently limited as they do not account for the entire range of wave propagation phenomena[37], unlike full-wave simulation-based techniques. Simulation-based technique [42, 43] can account for most of the physical phenomena, e.g. reflections, refractions and attenuation that occur during wave-propagation, while some models can even account for non-linear wave propagation, cavitation and shear waves. However, the high complexities, heterogeneous anatomical structures and the higher acoustic frequencies may require huge amount of computation resource to allow such simulations to run in viable time frames especially when accounting for non-linearity and shear waves. MR acoustic radiation force imaging (MR-ARFI) [44-46] is entirely non-invasive and has demonstrated the ability to produce high quality focusing. This technique exhibits the unique characteristic of directly monitoring acoustic pressure, and offers the possibility of

closed-loop control of transcranial sonication. Nonetheless, MR-ARFI is still in its initial stage and requires hours of measurement in the presence of the patient and the careful management of the transducer element grouping and activation[37].

The adoption of available technique is highly dependent on the strategy of the manufacturing company and the strategy is highly influenced by the demand from actual users – clinical surgeons. A non-invasive technique with a real-time or quasi-real-time functionality to provide rapid estimation for better treatment planning may increase its adoption rate and be more attractive for clinical usage. From the aforementioned technique, the best scenario is to combine the fast performance of analytical techniques and the accuracy of simulation techniques. However, there is always a trade-off between physical accuracy, simulation time and computational resources. In this study, a ray based phase correction technique was developed to compute pressure to the focal area and its verification was performed using hydrophone measurement.

1.4. The treatment protocol

The treatment protocol is well documented in literature [47-49]. The workflow of the treatment protocol is illustrated in Fig.1-4. A treatment flow is summarized with some limitations in this section.

Prior to the treatment day, pre-treatment planning images need to be obtained. These include a CT scan of the entire cranium and an MRI to define the target. These pre-treatment MR images are registered for delineation of the target [48]. On the treatment day, a stereotactic frame is fixed to the patient's head using local anesthesia. The frame-pins are placed as low as possible over the lateral orbits, just above the eyebrows, and in the occipital bone at or below the level of the external occipital protuberance. A circular elastic membrane with a central

opening is stretched to fit tightly around the head and placed as low as possible on top of the stereotactic frame [48]. This preparation process takes approximately 15 to 30 minutes. After pre-test of the transcranial MR guided focused ultrasound (TcMRgFUS) device using a gel phantom, a patient then is positioned supine, head first on the MR table. The stereotactic frame is locked to the MR table to maintain a constant position between the patient and the transducer [48].

Low power sonication, resulting in sub-therapeutic heating in the 40-45 ºC range, is performed to localize the focal spot using MR thermometry. Phase correction is used to steer the beam within a small range of a few millimeters. For larger changes in focal spot position, the transducer is physically moved, while the patient stays fixed in a frame that is mounted to the MR table and is only in contact with transducer system through the flexible membrane and water [48]. After the focal spot is sufficiently steered to the target, sonication is performed with sufficient power to achieve a planned target temperature such as 55-60 ºC. During the cooling periods of several minutes between each sonication treatment, magnetic resonance images may be acquired. Moreover, since the patients are fully awake during the entire intervention procedure, the cooling period are used for interviews and neurological examinations [47]. Both optimal coverage of the target and clinical feedback from patients play a role in determining treatment. Total treatment time spent on the MR table, including positioning, imaging, planning, sonication and post MR imaging is typically four hours. This could be fallen to as low as 2 hours of table time in some experienced centers, not including frame placement and post-operation imaging.

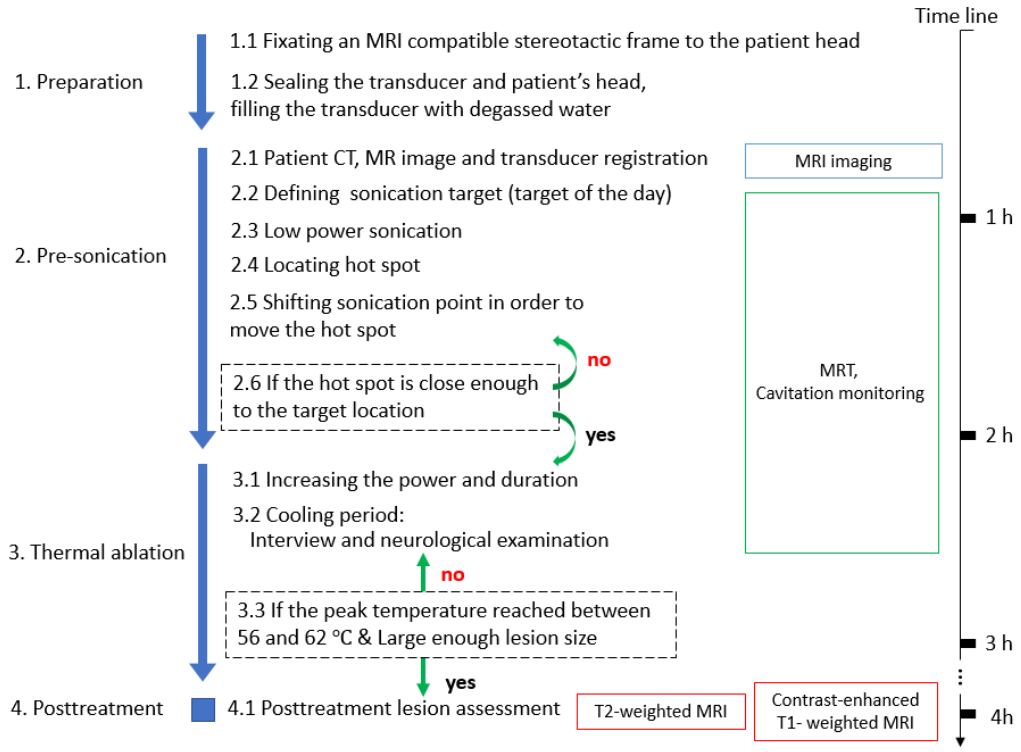

Fig. 1-4 The time table of treatment protocol in MR guided FUS essential tremor traetment with estimated time.

The abovementioned treatment time is typically for an ideal case. The treatment time can easily be extended for various reasons. An unintentional movement of the patient during sonication could rewind the treatment to the initial registration stage which could easily take an additional hour to shift the focal spot of the target. Due to individual differences, the thickness and acoustical properties of the skull are significantly different between patients. The phase correction is estimated from the path of each ray crossing the skull from the transducer elements to the focus [48]. However, difficulty elevating peak temperature on thick skull cases has been reported and the skull density ratio showed a positive relation to the peak achievable temperature [50]. A planning tool, with fast computation of phase correction and is based on a more realistic acoustic model could circumvent the limits. The treatment could be accelerated and the untreatable target could be ablated using optimization of transducer-patient placement with a fast simulation tool.

Chapter 2

MATERIALS AND EXPERIMENT SETUP

In this chapter, the hardware setup of the experiment will be presented and the software-hardware registration process described in detail. The experiment was implemented at the Focused Ultrasound Center at the University of Virginia.

2.1. Experiment preparation-hardware setup and system wiring

The degassed water (the remaining oxygen level less than 1.1%) was prepared using collected tap water before wiring the hardware system. The treatment bed (Fig.2-1.3) was undocked from the MRI system and moved toward the door of MR room with the power cable connected to the transducer amplifier (Fig.2-1.4). The FUS transducer (Fig.2-1.2) was carefully detached from the treatment bed and placed in the AIMS III scanning tank (AST3-L, ONDA, CA, US). The transducer was mounted on a purpose built frame which was fixed inside of the scanning tank in order to keep the transducer face up and rigidly fixed. The scanning tank was kept waterless during whole experiment and the transducer was filled with degassed water. The portable degassing suitcase (Fig.2-1.7) was utilized as a pump to feed the degassed water into the transducer. During the experiment, the FUS work station (Fig.2-1.8) was utilized to setup the inputs of each sonication.

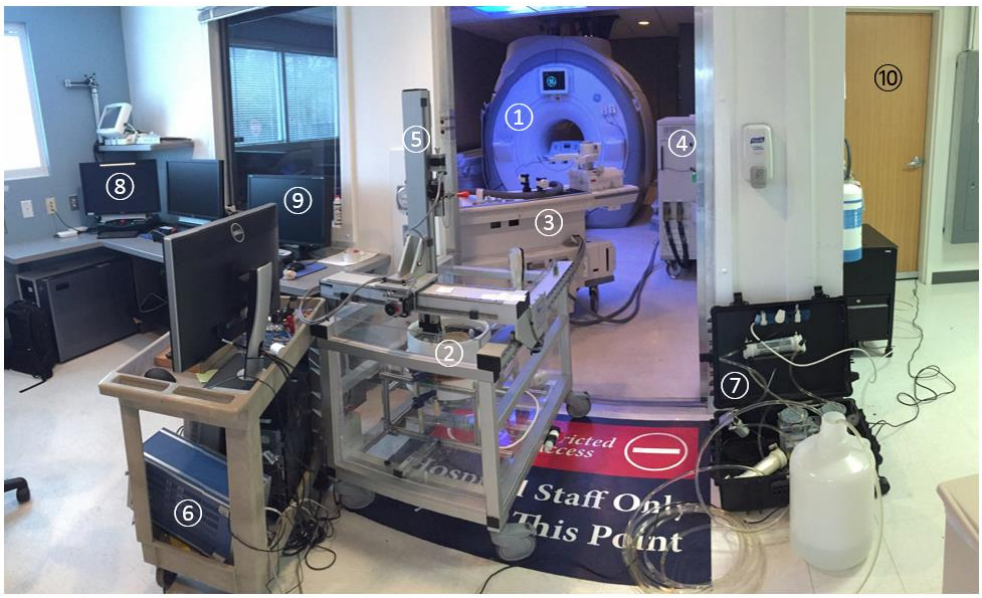

Fig. 2-1 Hardware system setup and wiring. ①3T GE MRI imaging system ② InSightec, ExAblate 650 kHz focused ultrasound transducer ③ Focused ultrasound patient treatment bed ④ Amplifier of transducer ⑤ XYZ positioner ⑥ Positioner guide system ⑦ Portable degassing suitcase ⑧ Work station of FUS system ⑨ Control PC of MRI imaging system ⑩ Machine room

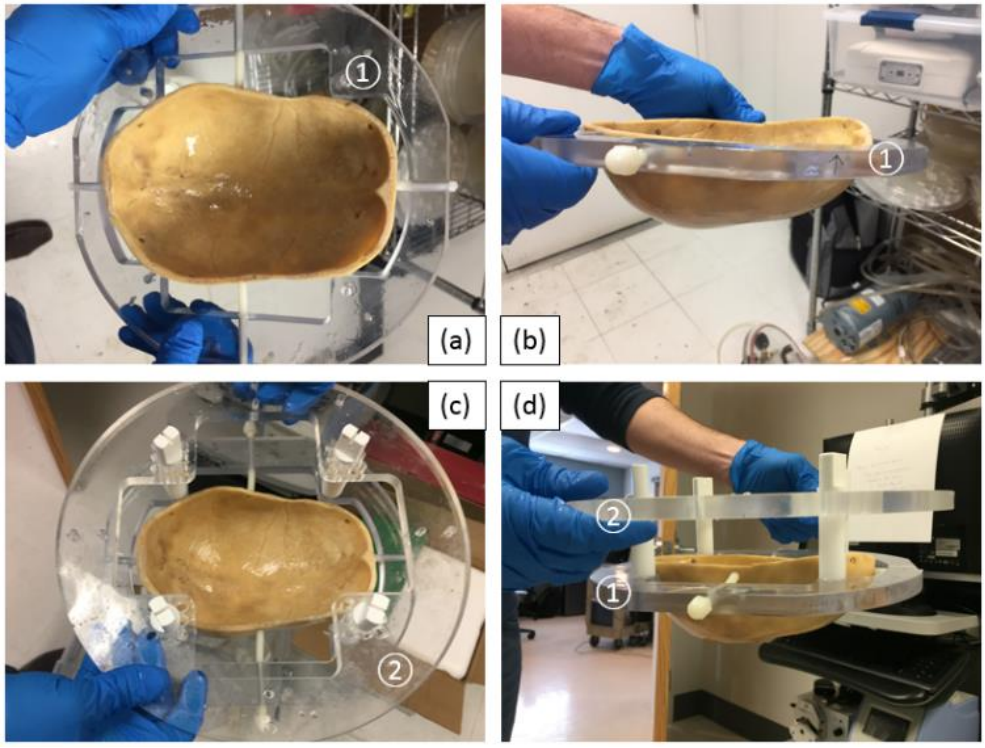

Fig. 2-2 The skull frame to mount the skull into the FUS transducer. (a) Superior and (b) left view of skull-frame (marked as ①) mount (c) Superior and (d) left view after connect skull-frame to assembly base (marked as ②), four 40mm long connecting rod was utilized to connect the skull-frame to assembly base

2.2. Skull-frame setup on the FUS transducer

The cadaver skull was mounted on a polycarbonate frame using four polyvinyltoluene (PVT) screws from four directions (Fig.2-2.a) and then put into a degassing cylinder. One-hour skull degassing was performed before attaching the skull-frame to the assembly base. Four 40 mm connecting rods were utilized to secure the skull-frame on the assembly base and then the whole assembly was kept in the degassed water. A silicone grease was smeared on the groove of transducer edge and the top-hat reservoir (in Fig.2-2.2, white container) was attached on the transducer.

2.3. Supporting pad removal on the CT image

A skull-frame image volume was acquired using the CT scan feature in a Gamma system (Leksell Gamma Knife Icon, Elekta Inc, CA, US) with the CBCT setting as shown in Table 1.

A supporting pad was placed under the skull-frame during CT imaging in order to level the frame to the X-axis of the CT image. Undesired voxels were also captured in this CT image because of this supporting pad. The skull frame CT image will be utilized in ray tracing simulation and the voxels formed by the supporting pad may provide incorrect refraction of the ray tracing. These voxels are required to be removed and a filtered version of the CT image was created. A semi-automatic image processing algorithm was developed using an active mask to remove undesired voxel in CT images. The boundary of the active mask was interactively calculated based on manually defined seed points on each image frame. First, one central seed point needs to be defined which requires approximate placement on the center of the skull cap in CT image. Then, two seed points which were placed few pixels below the bottom face of the frame need to be defined and this will give an angle limitation for the edge

searching process (Fig.2-3.a). A searching ray may emit from the defined central seed point and across the skull cap until reaching a defined length. The number of rays was arbitrarily defined as 9 and it can be changed depending on the requirement. The intensity along each ray was collected. A simple peak finding process provides the inner and outer layer location of the skull from the intensity data. The outer layer is used as a minimum guide to the active tracing edges.

Since the skull cap has a non-linear shape and radius is changing along the horizontal axis in sagittal plane (Fig.2-3.b), the tracking edge could be defined by adding an amount of pixel value to the detected inner edge on Sagittal plane. In order to derive the tracking edge from detected inner skull layer an ellipsoidal fitting was applied to get a smooth cap shape. In addition, the ellipsoid cap was shifted by few pixels to make a guideline for the tracing edge computation in the coronal plane (Fig.2-3.c). A guide line was used as the radius of the tracing edges and the final mask was formed based on the tracing edges, manually defined seed points and the bottom boundaries of the image below two seed points. The processed image was saved as a new series of DICOM images and the 3D surface was reconstructed per the following section.

Table. 1 The cone beam computed tomography (CBCT) setting for skull-frame CT imaging in Leksell Gamma Knife Icon system

CTDI [mGy]	Voltage [kV]	Current [mA]	Pulse Length [ms]	Number of projections
6.3	**90**	**25**	**40**	**332**

The 3D structure of the skull with a frame was reconstructed using the isosurface function in the medical image processing software Amira 5.2 (FEI Visualization Sciences Group, Bordeaux, France) and the reconstructed surfaces before and after removal were illustrated in Fig.2-4.

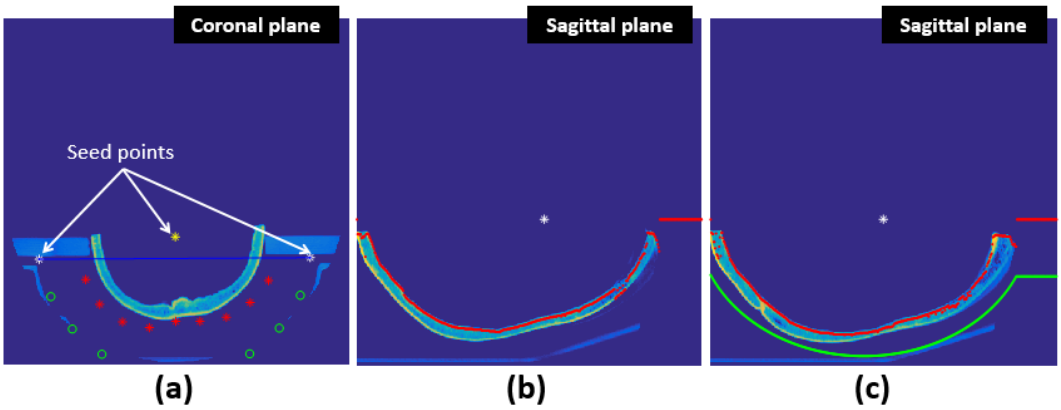

Fig. 2-3 The work flow of support pad removal from the CT image (a) Three seed points were manually defined (two white star point and one yellow star point). The red star points denote the actively tracked edge points which will utilized as boundary of the removal mask (b) The detected inner layer of skull cap was marked using red dots (c) A ellipsoidal shape fitting was applied on the detected skull layer and shifted a certain distance to create a guide line to the active tracker on Coronal plane

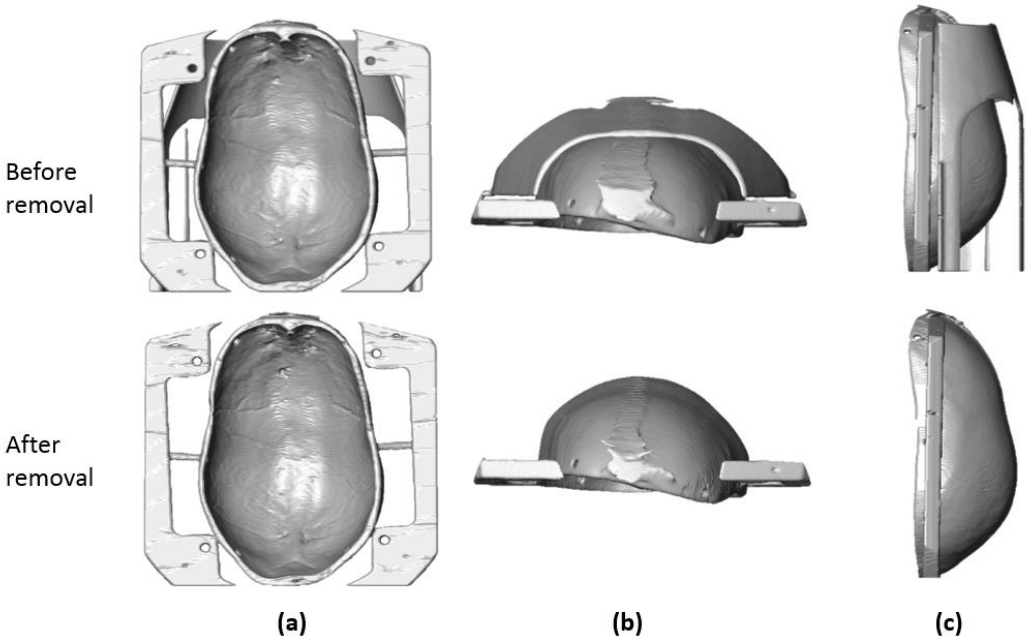

Fig. 2-4 The reconstructed skull-frame volume from CT image before and after remove the supporting pad (a) cranial view (b) frontal view (c) lateral view

2.4. Fiducial point coordinate in CT image

The fiducial points in CT images have distinct and relatively large voxel intensity and a known image volume. These features can be utilized while computing the central position of fiducial points in the image coordinates. An image processing technique (Fig.2-5) was developed for finding and localizing the centroid of the fiducial points imbedded in the skull mounting frame from a computed tomography (CT) image volume.

The default DICOM series data were stored as consecutive images on coronal plane as shown in Fig. 2-5.a. Since the fiducial points within the skull mounting frame were placed at a parallel plane to the transverse plane of skull, it is more convenient to process the image on the transverse plane. The DICOM images were imported in computer memory using Matlab and the transverse plane images were separated to four parts to ensure that each of them contains one fiducial point (Fig. 2-5.a). The fiducial point with highest pixel value (brightest) was visible on the corner of the skull mounting frame (Fig. 2-5.a1~a4). A threshold based edge searching algorithm was implemented on four separated image volumes and a sample line (vertical dashed line in Fig. 2-5.a1) to show the intensity difference between different materials was plotted in Fig. 2-5.b1. The threshold was defined as 5850 based on the pre-investigation on three cutting planes (on Sagittal, Coronal and Transverse plane) which all intersect the fiducial point. The intensity of the fiducial points in this version of CT image has a saturated maximum value of 6000 and this limits the precision of central location detection based on pure image intensity. A candidate 3D volume for a fiducial point could be reconstructed based on the detected threshold-based edges as shown in Fig. 2-5.b2~b4. It assumes that the geometrical center of this 3D edge volume represents the fiducial point. The derived fiducial points (red dot) with the closest CT image plane were shown in Fig. 2-5.c. The CT image derived fiducial points are listed in Table 2. However, these coordinates need to be transformed to a measurement based coordinate system and this will be discussed in a following section.

Then a registration between the skull-frame structure and FUS transducer could be achieved by using a derived transformation matrix.

Table. 2 CT image derived fiducial point coordinate in CT image domain. The voxel size is 0.5 x 0.5 x 0.5 mm^3. This coordinate serves as ananchor to allow the registration between different systems.

Point #	X axis	Y axis	Z axis
P1	**31.0831**	**73.2729**	**298.9306**
P2	**349.9560**	**59.1668**	**306.3435**
P3	**363.7277**	**378.8297**	**304.7568**
P4	**44.2427**	**392.7406**	**397.1311**

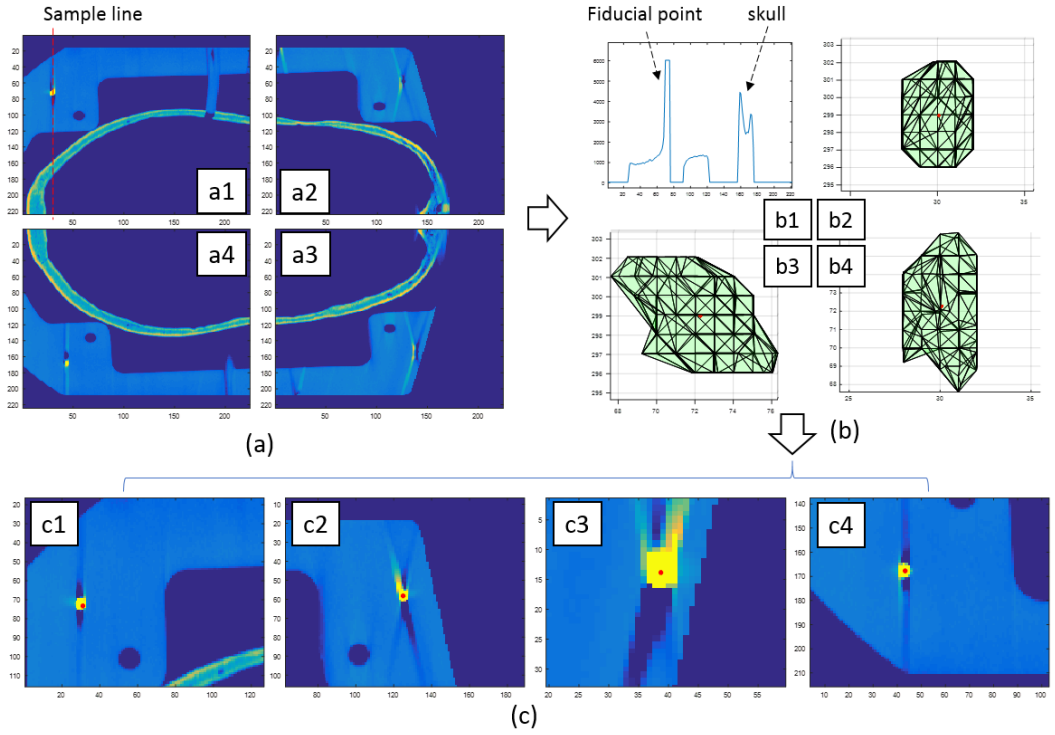

Fig. 2-5 The image process to localize the fiducial points in CT image. A threshold of 5843.3 on CT image was utilized to find the fiducial points.

2.5. Fiducial point coordinate in transducer system

An INI configuration file is placed in the 'ExportData' folder on InSightec workstation. This configuration file contains information about the 3D location and surface area of each transducer channel. S portion of the geometry data is shown in Table 3.

Table. 3 Portion of 650 kHz FUS transducer geometry file. Total of 1024 channel coordinates and surface areas were stored in an INI configuration file in the workstation folder '\EportData\XX-XX-XX_ANx\WSFiles\Site\SiteInifiles\XdIni'

Channel #	3D Coordinate [mm]			Surface Area
	X	Y	Z	Square [mm^2]
XCH0	82.5241	7.8761	24.8625	124
XCH1	72.302	7.8012	18.6807	124
XCH2	61.1608	7.9406	13.1391	124
XCHN	…	…	…	…

The numerical simulation estimates the focal quality of the FUS sonication and requires a detailed geometry of each element in the transducer. The data stored in the configuration file provides such information, and it can be used in the reconstruction process to define transducer geometry which can be subsequently utilized as a boundary condition of numerical simulations. The pattern of transducer elements on two different views was plotted in Fig.2-6.

Based on the CAD sketch (Fig.2-7.a) of the transducer, the skull mounting frame and the top-hat reservoir, it is possible to derive the central coordinate of fiducial points. Eight fiducial points were imbedded in the skull-mounting frame. However, only four fiducial points were visible in the skull-frame CT image. This is an artifact of a small scan volume of the Leksell Gamma Knife CT scanner. A CT scanner with larger scan volume is desirable to provide a full capture of the skull-frame structure. This would also increase the accuracy of registration with the help of eight, rather than four, registered fiducial points from CT.

The coordinates of a fiducial point on X and Y axes (horizontal plane) could be easily derived from a measured schematic of the FUS transducer setup, but the relative heights between fiducial centroid and the transducer are not described in the sketch. Since we know that the radius of the fiducial points is 1mm, the length from fiducial centroid to lower plane (Fig.2-7.b) of the skull-mounting frame could be geometrically derived as shown in Fig.2-7-c. Note that, the detailed geometry of actual FUS transducer was not permitted to be distributed and is not included in this paper because it is considered to be protected corporate intellectual property. Fig. 2-7.a is a simplified sketch and it does not represent the actual scale of FUS transducer. Finally, the fiducial point coordinates in the FUS transducer domain were derived and listed in Table. 4.

Table. 4 Fiducial point coordinate derived from transducer CAD and measurement.

Point #	X coordinate	Y coordinate	Z coordinate
P1	-80	80	137.3
P2	80	80	137.3
P3	80	-80	137.3
P4	-80	-80	137.3

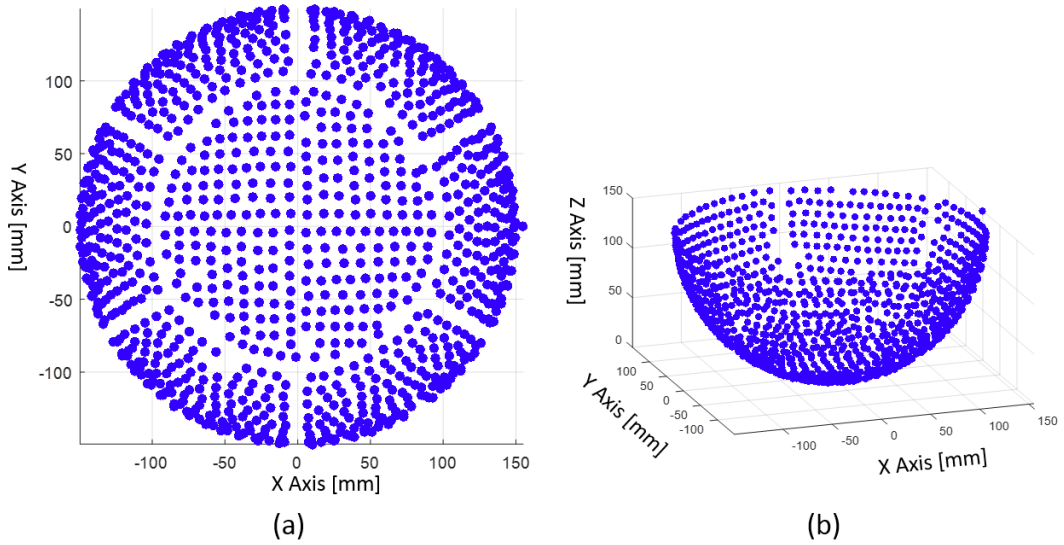

Fig. 2-6 The pattern of 1024 channels in hemisphere 650 kHz FUS transducer. (a) XY plane view of the transducer (b) oblique bird eye view of the plotted transducer

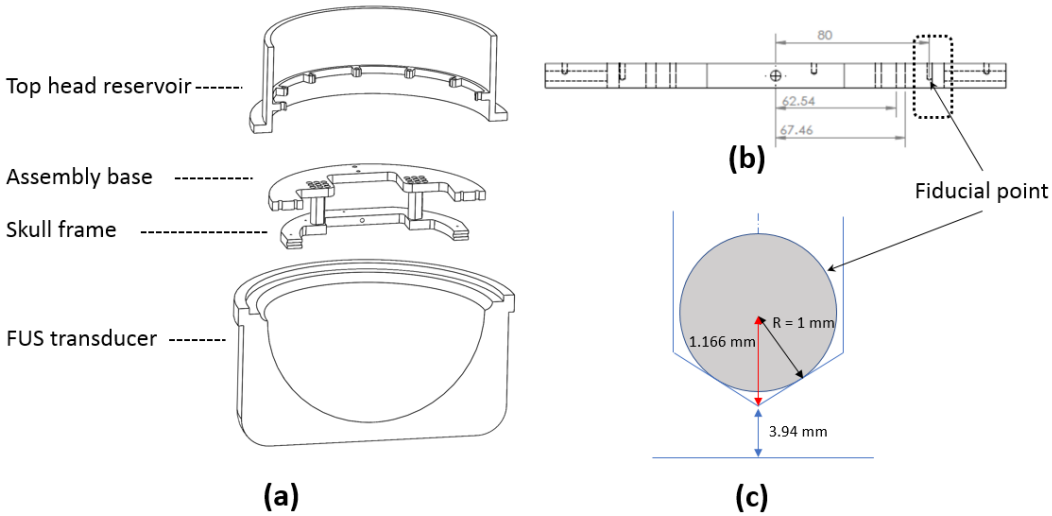

Fig. 2-7 (a) A CAD sketch of transducer, skull assembly, skull frame and top-head reservoir (b) The sectional view of the skull frame which imbedded 8 fiducial point. (c) The sketch illustrates the relative heights between the geometrical center of fiducial point and the lower face of the skull frame

2.6. Skull-frame CT and FUS transducer registration

Since the voxel size (0.5 x 0.5 x 0.5 mm^3) of CT was precisely defined and the unit of transducer coordinate is in millimeter, the transformation between CT and transducer data is much simpler and only the rotation matrix may be involved.

In linear algebra case, the singular value decomposition (SVD) is a factorization of a real or complex matrix. Formally, the singular value decomposition of an m by n real or complex matrix M is a factorization of the form $U\Sigma V^*$, where U is an m by m real or complex unitary matrix, Σ is a rectangular diagonal matrix with non-negative real numbers on the diagonal, and V is an n by n real or complex unitary matrix [51, 52].

$$M = U\Sigma V^* \tag{2.1}$$

In the special, when M is an m by m real square matrix with positive determinant, U, V^* and Σ are real m by m matrices as well, Σ can be regarded as a scaling matrix, and U, V^* can be viewed as rotation matrices. Thus, the expression $U\Sigma V^*$ can be intuitively interpreted as a composition of three geometrical transformation; a rotation or reflection, a scaling, and another rotation or reflection.

Since, the data size of transducer is much smaller than the CT image it is more efficient to define transducer coordinate as A matrix. The SVD was computed in Matlab software using a SVD function as bellow,

$$[U, \Sigma, V] = \text{SVD}(FP_{CT}, FP_{Transducer}) \tag{2.2}$$

where FP indicates the fiducial point coordinate.

The rotation matrix

$$R = UV^* \tag{2.3}$$

and translation matrix

$$T = -R \cdot (A_{centroid})' + (B_{centroid})' \tag{2.4}$$

were computed and the final transformation was implemented based on following formula

$$B = R \cdot A' + T \tag{2.5}$$

Finally, a composite figure of CT skull-frame image and transducer element was plotted in Fig.2-8. In order to give a better see-through view, only half of the transducer was plotted intentionally. This result may contribute a better localization and understand of in-vitro skull experiement and also provide a geometrical configuration of experiment setup for numerical simulation.

2.7. Further coordinate configuration

The coordinate configuration between software-hardware systems was investigated to provide a clear lookup data. As shown in Fig.2-9.a, this configuration combined a coordinates system of the transducer in workstation, patient perspective direction, and hydrophone scanning domain in AIMS system. This configuaration provides key imformation to the hardware-software registration in the follwing study .

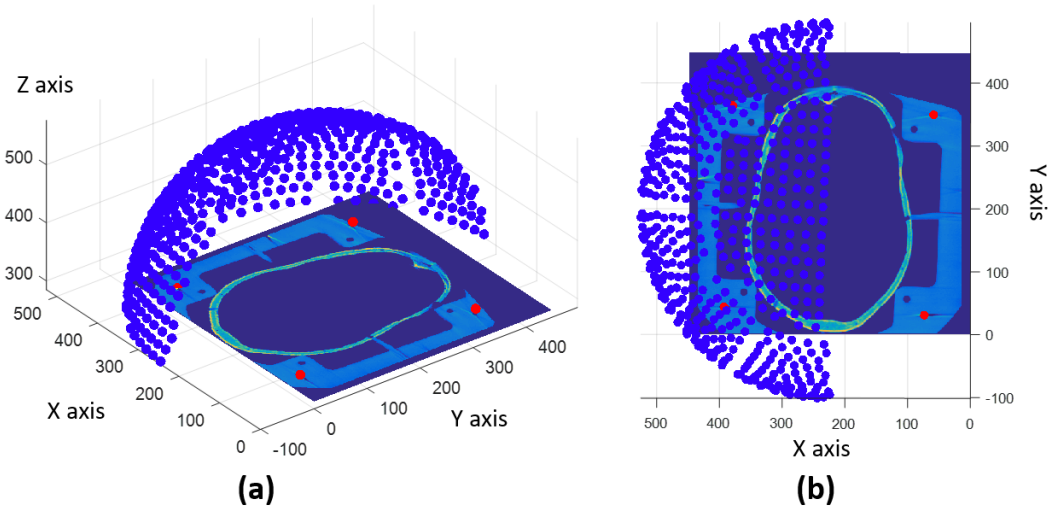

Fig. 2-8 Registration of CT image and transducer pattern. (a) Bird eye view of the composite plot of FUS transducer and skull-frame CT image. The fiducial point was painted as red dot (b) A caudal view of the composite plot was illustrated. Note that only half of the transducer channel were plotted

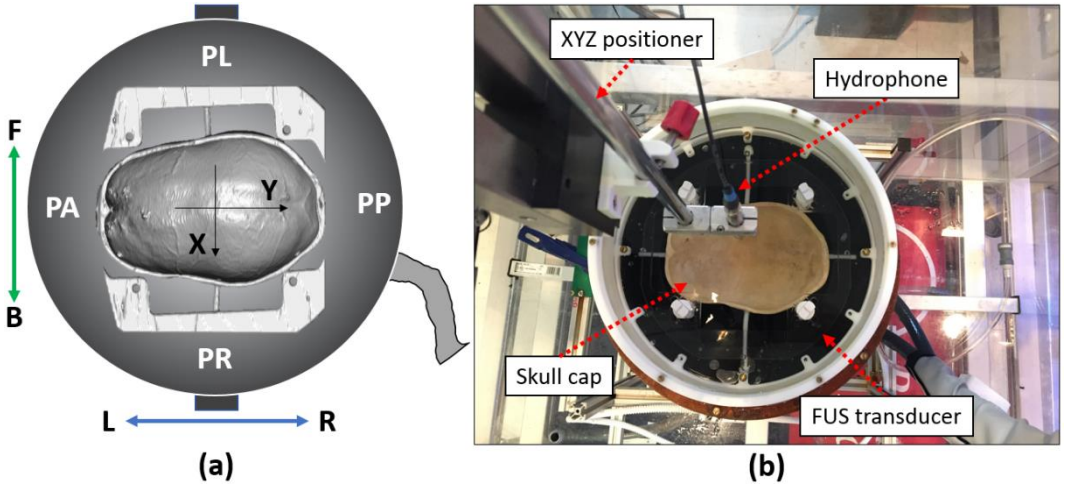

Fig. 2-9 The coordinate system configuration. (a) The coordinate of hydrophone scanning domain was marked as front (F), Back (B), left (L) and right (R); The patient perspective direction was plotted as patient anterior (PA), patient posterior (PP), patient right (PR) and patient left (PL); The transducer coordinate was marked using X and Y arrows. (b) The look down view of FUS transducer with skull-frame setup.

Chapter 3

RAY TRACING SOFTWARE

3.1. The infrastructure of the software

A user-friendly software was developed to visualize the rays on the focal target from transducer elements and to compute the pressure near the focal area. In this chapter, the basic concept of the developed software is presented. The infrastructure of this software was developed by Dr. Snell and Mr. Quigg in Focused Ultrasound Foundation (Focused Ultrasound Foundation, Charlottesville, Virginia, US) at its early stage [53]. This dissertation is an extension of the software to include pressure computation and experimental verification of this software.

In computer graphics, ray tracing is a technique for generating an image by tracing the path of light emitted from a source through each pixel in an image plane and simulating the effects of its encounters with virtual objects [54, 55]. The technique is capable of producing a high degree of visual realism may be used in an analogous way to simulate a wide variety of acoustical effects, such as reflection and refraction, scattering, and dispersion phenomena [56].

The software platform to perform the ray tracing was developed using Java language in NetBeans IDE (Oracle Corporation, Redwood City, CA, US). The main and heavy computation was solved in the graphics processing unit (GPU) using an open graphics library (OpenGL, Silicon Graphics, CA, US). OpenGL is a cross-language, cross-platform application programming interface (API) for rendering 2D and 3D vector graphics. The API is typically used to interact with a GPU to achieve hardware-accelerated rendering and computation.

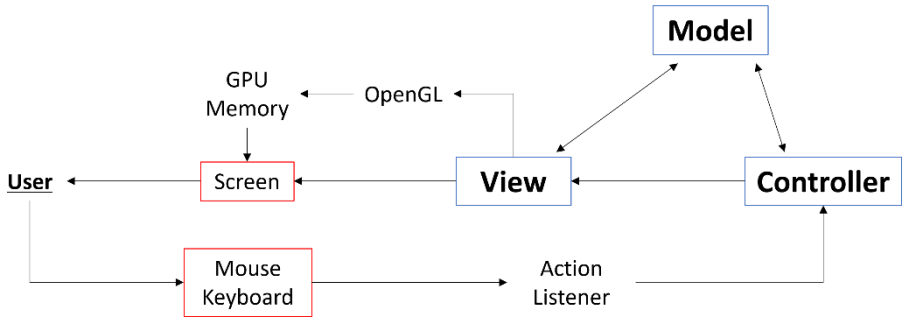

Fig. 3-1 The simplified model-view-controller (MVC) pattern used in this study. The corel of MVC triangle was maintained to keep the indivisual model independent. The mouse and keyboard listen to the user's input and interprets this order to the controller. Then the controller manages the predefined work flow and plot the result on the screen to the users.

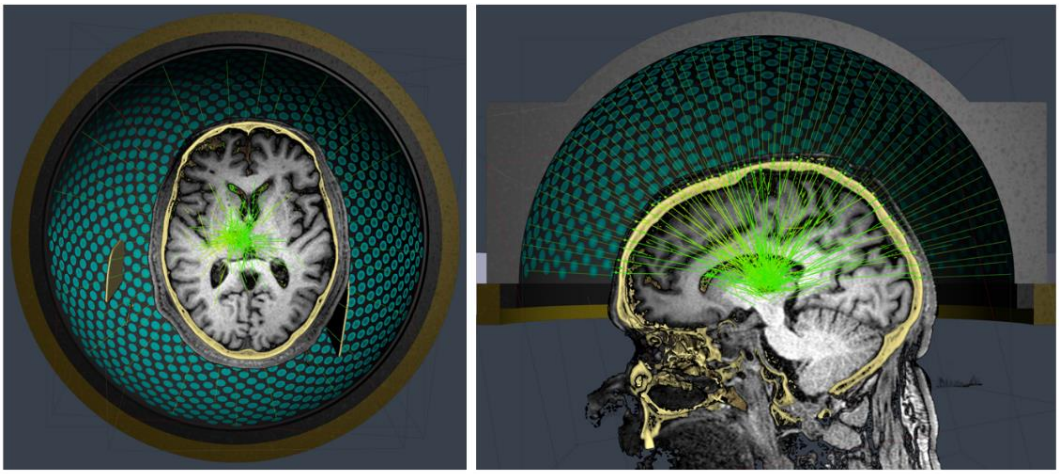

(a) (b)

Fig. 3-2 Preview of the developed ray tracing software with patient-specific CT and MRI data. The MR and CT image were registered and the 3D scene could be observed in arbitrary location and angle.

The software was designed to strictly obey the objective oriented programming (OOP) protocol, which provides a highly flexible and extendable feature. A clear model-view-controller (MVC) pattern (see Fig.3-1) was implemented to separate the coherent connection between each functional module. As shown in Fig.3-1, the triangle connection of MVC pattern provides a flexible foundation to appended modules.

An action listener was designed to pass corresponding attribute to the MVC domain by interpreting the user's input through mouse and keyboard. The instant parameter and the data generated in the MVC pattern was processed by central processing unit (CPU) and this process occupies the memory in the random-access memory (RAM). On the contrary, the CT and MRI data was loaded directly into the memory in the GPU to reduce the computation load from CPU. The vertex shader and fragment shader was coded in OpenGL shading language in order to project the 3D data to 2D screen. A compute shader was utilized to contain the main computation work as well as the ray tracing algorithm. Furthermore, the manual registration on CT and MRI data could be achieved in developed software. Thanks to the flexibility of the software, it is possible to append more functional modules. Such as the manual registration module for MRI and CT image and treatment data replay module. The source code of this software, expect for the proprietary module of the manufacturer, will be available as an open source project. Thus, the details about the code are not included in this dissertation. A preview of the developed domain is illustrated in Fig.3-2.

In the following section, the basic of computer vision techniques to implemented ray tracing are introduced. The intersection point detection between wave beam and skull surface, and the skull surface normal vector estimation are described.

3.2. Ray-skull collision detection

Since the emitted plane wave is propagated along a beam in the medium, the path of the wave can be illustrated as a line as shown in Fig.3-3.a. After a period of time, the wave may arrive at the skull surface and define a collision point on the skull. However, in reality a large contact area between wave front and skull surface is involved. In this study, we only consider the collision point (marked as green point in Fig.3-3.a) lying on the central axis of the beam, and the skull as well as the subcutaneous tissue were neglected during collision detection.

The source location (beam star point) $p_i(x, y, z)$ could be extracted from the transducer parameter INI file created by the system manufacturer. A geometric center oriented vector $\vec{v}(i, j, k)$ was utilized to represent the wave beam and illutrsated using red dot line in Fig. 3-3.b. The small integer or span of gradient was defined as 0.1 mm. The coordinate of the vector end point $p_{i,n}$ could be defined as follow

$$p_{i,n} = p_i + 0.1 \times n \times \vec{v} \tag{3.2.1}$$

The corresponding CT value $f_{(p_{i,n})}$ on the point $p_{i,n}$ was collected and compared to the predefined threshold τ_{skull} which binarizes the CT data to skull and non-skull volume. An iterative increase of n was utilized to search the collision point that satisfies $f_{(p_{i,n})} \geq \tau_{skull}$. The detected collision represents the intersection between wave beam and skull outer layer. The similar concept was utilized to detect the second collision that represents the intersection point between inner layer and refracted wave beam. Care should be taken while defining the skull threshold because the proposed collision detection method is highly sensitive to this value.

3.3. Surface normal estimation

The surface normal based on pre-detected collision point is crucially required to compute incident angle that will serve in refraction angle computation (Fig.3-4). One might expect that

algorithm to find the boundaries of the objects directly from the intensity values in the image volume by using a threshold. However, when the boundaries have complicated shapes, this is difficult. The edge of the surface is a small area in the image volume where the local levels are changing rapidly. An edge operator is a mathematical operator with a small spatial extent designed to detect the presence of a local edge in the image volume. The gradient at a Cartesian coordinate location is defined as

$$\nabla G = \left| g_x \;\; g_y \;\; g_z \right|^T \tag{3.2.2}$$

and the magnitude of the gradient is given by

$$g_{(n_x,\, n_y,\, n_z)} = \sqrt{{g_x}^2 + {g_y}^2 + {g_z}^2} \tag{3.2.3}$$

Three 3D gradient operators, or masks, to do the computation, capitalizing the ideas of Zucker and Hummel where all the 26 neighborhoods which associated with each voxel are involved in computing the gradient vector components. The mathematical foundations to derive three basic functions that define their local operator was introduced by Zucker and Hummel [57]. One common form of the 3D Sobel operator that approximates the first derivatives g_y, g_y and g_z using the $3 \times 3 \times 3$ filter is shown in Fig. 3-4. The surface normal was defined as follow

$$\boldsymbol{n} = normalize(\; f_{(p_{i,n})} * g_x \;, f_{(p_{i,n})} * g_y \;, f_{(p_{i,n})} * g_z \;) \tag{3.2.4}$$

The threshold T in Eq. 3.2.2 could be utilized during segmentation of volume data to binary structure of the object. In other words, it could provide skull surface extraction from CT data set. In this study, we did not attempt to implement this technique for segmentation, but rather for normal vector estimation. The normal vector of skull surface based on detected collision point could be derived by normalizing the resulting vector after applying gradient operators on three axis as described in Eq.3.2.4.

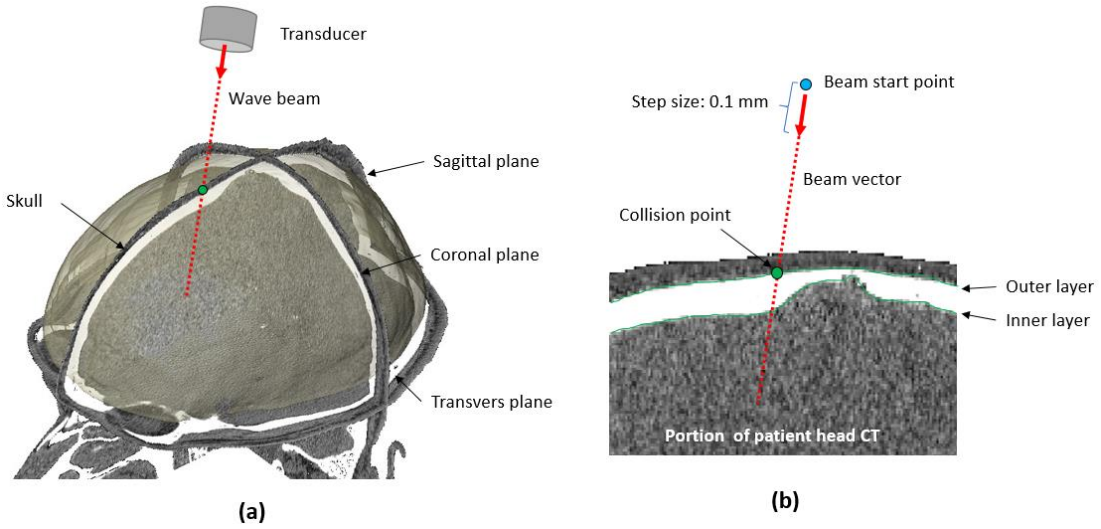

Fig. 3-3 (a) The 3D illustration of the relative possition between skull structure and wave beam of single transducer channel. (b) The collision detection along ray path. A 0.1mm step size was utilized in collision detection. The brighter pixel represents higher intensity and darker pixel rerpents lower intensity in CT image.

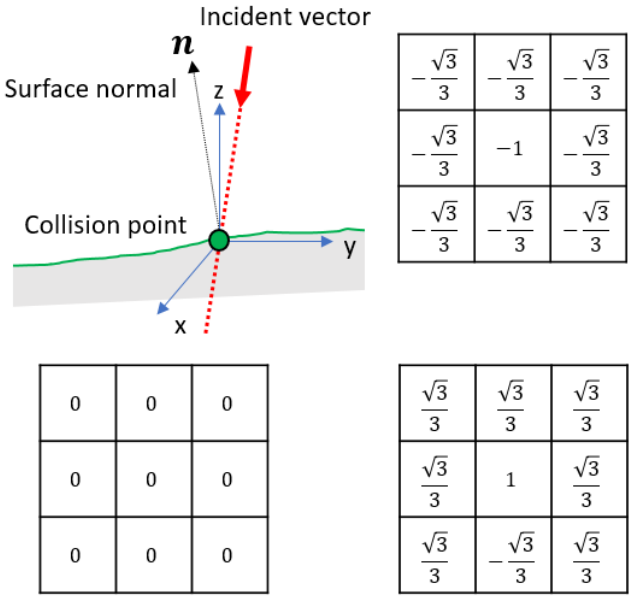

Fig. 3-4 The surface normal was estimated using 3D Zucker-Hummel edge operator. There requires three set of basis functions to derive the gradient on XYZ axis. The $3 \times 3 \times 3$ edge basis function, which is $g_x(x, y, z)$, for X axis was plotted.

Chapter 4

RAY BASED FOCAL QUALITY ESTIMATION

4.1. Introduction of ray method

Ray based models have been used for many years in underwater acoustics. Ray theory originally emerged from optics where it was used to understand the propagation of light even before the more fundamental equations for light propagation (Maxwell's equations) were known [58]. The ray theory could be derived from full wave equation as follow.

The Helmholtz equation in Cartesian coordinate **x** = (x,y,z),

$$\nabla^2 p + \frac{\omega^2}{c^2(x)} p = -\delta(x - x_s) \tag{4.1.1}$$

Where c(x) is the sound speed and ω is the angular frequency of the source located at x_s. The solution of Helmholtz equation in the form

$$p(x) = e^{i\omega\tau(x)} \sum_{j=0}^{\infty} \frac{A_j(x)}{(i\omega)^j} \tag{4.1.2}$$

This is called ray series which are divergent, but in certain cases it can be shown to be an asymptotic approximation to the exact solution. A is the amplitude vector of j order. Taking derivatives of the ray series, it obtain

$$p_x = e^{i\omega\tau} \left[i\omega\tau_x \sum_{j=0}^{\infty} \frac{A_j}{(i\omega)^j} + \sum_{j=0}^{\infty} \frac{A_{j,x}}{(i\omega)^j} \right] \tag{4.1.3}$$

and

$$p_{xx} = e^{i\omega\tau} \left\{ [-\omega^2(\tau_x)^2 + i\omega\tau_{xx}] \sum_{j=0}^{\infty} \frac{A_j}{(i\omega)^j} + 2i\omega\tau_x \sum_{j=0}^{\infty} \frac{A_{j,x}}{(i\omega)^j} + \sum_{j=0}^{\infty} \frac{A_{j,xx}}{(i\omega)^j} \right\} \tag{4.1.4}$$

Thus, the Laplacian of the pressure could be written as follow

$$\nabla^2 p = e^{i\omega\tau}\left\{[-\omega^2|\nabla\tau|^2 + i\omega\nabla^2\tau]\sum_{j=0}^{\infty}\frac{A_j}{(i\omega)^j} + 2i\omega\nabla\tau\sum_{j=0}^{\infty}\frac{A_j}{(i\omega)^j} + \sum_{j=0}^{\infty}\frac{\nabla^2 A_j}{(i\omega)^j}\right\} \tag{4.1.5}$$

Substituting this result into the Helmholtz equation and equating terms of like order in ω, it obtains the following infinite sequence of equations for the functions and $\tau(x)$ and $A_j(x)$,

$$\begin{aligned} O(\omega^2) \quad &: \quad |\nabla\tau|^2 = c^{-2}(x) \\ O(\omega) \quad &: \quad 2\nabla\tau\cdot\nabla A_o + (\nabla^2\tau)A_o = 0 \\ O(\omega^{1-j}) \quad &: \quad 2\nabla\tau\cdot\nabla A_o + (\nabla^2\tau)A_o = -\nabla^2 A_{j-1}, j = 1,2,\ldots \end{aligned} \tag{4.1.6}$$

Where $O(\omega^2)$ for $\tau(x)$ is known as the Eikonal equation. The remaining equations for $A_j(x)$ are known as the Transport equation [58].

As shown in Eq. 4.1.6, the linear partial differential equation (PDE) was converted into a nonlinear Eikonal equation and an infinite series of Transport equation. At this point, the standard simplification made is to ignore all but the first term in the ray series, which is high frequency approximation. The limit is $\omega \to \infty$ and this leads to geometric ray theory.

The family of rays which are perpendicular to the wavefronts of $\tau(x)$ as shown in Fig. 4-1. The Eikonal equation

$$|\nabla\tau|^2 = c^{-2}(x) \tag{4.1.7}$$

The ray trajectories on each coordinate could be [58]

$$\frac{d}{ds}\left(\frac{1}{c}\frac{dx}{ds}\right) = -\frac{1}{c^2}\nabla c \tag{4.1.8}$$

To obtain the pressure field there is a need to associate a phase and an amplitude with each ray. The phase was obtained by solving the Eikonal equation in the coordinate system of the rays. The original nonlinear PDE has been reduced to a linear ordinary differential equation which is solved to yield

$$\tau(s) = \tau(0) + \int_0^s \frac{1}{c(s')} ds' \tag{4.1.9}$$

The integral term in this equation is the travel time along the ray, so from a physical point of view the phase of the wave is simply delayed in accordance with its travel time. This will be utilized to compute the arrival phase of each channel and compute a compensation phase to correct focal spot.

By solving the transport equation, the amplitude associated to each ray can be computed. Recall the transport equation

$$2\nabla\tau \cdot \nabla A_o + (\nabla^2\tau)A_o = 0 \tag{4.1.10}$$

Since the ray is perpendicular to the wave front, we can rewrite the above equation as

$$\frac{2}{c}\frac{dx}{ds} \cdot \nabla A_o + (\nabla^2\tau)A_o = 0 \tag{4.1.11}$$

The first term represents a directional derivative along the ray path so that

$$\frac{2}{c}\frac{dA_0}{ds} + (\nabla^2\tau)A_o = 0 \tag{4.1.12}$$

This represents the amplitude changes along a ray in relation to the spreading of a ray tube. In order to make this statement precise, a Jacobian can be utilized

$$J = \left|\frac{\partial X;}{\partial(s,\theta,\varphi)}\right| = \begin{vmatrix} \frac{\partial x}{\partial s} & \frac{\partial x}{\partial \theta} & \frac{\partial x}{\partial \varphi} \\ \frac{\partial y}{\partial s} & \frac{\partial y}{\partial \theta} & \frac{\partial y}{\partial \varphi} \\ \frac{\partial z}{\partial s} & \frac{\partial z}{\partial \theta} & \frac{\partial z}{\partial \varphi} \end{vmatrix} \tag{4.1.13}$$

Where θ and φ are respectively the declination and azimuthal take-off angles of the ray. The final result for the solution of the transport equations is [58]

$$A_o(s) = A_o(o)\left|\frac{c(s)J(0)}{c(0)J(s)}\right|^{1/2} \tag{4.1.14}$$

There require initial conditions to solve Eq. 4.1.8. Assuming the initial condition as $\tau(0) = 0$, $s = 0$ and treat the wave is traveling in homogeneous medium. Then we could obtain

$$x(s) = x_s + s(cos\theta cos\varphi, cos\theta sin\varphi, sin\theta) \tag{4.1.15}$$

Thus the rays are simply straight lines emitting out from the source as shown in Fig. 4-1. The Jacobian determinant in Eq.4.1.13 is transformed to

$$J(s) = -s^2 cos\theta \tag{4.1.16}$$

Thus, Eq.4.1.14 becomes

$$A_o(s) = \frac{1}{4\pi}\left|\frac{c(s)cos\theta}{c(0)J(s)}\right|^{1/2} \tag{4.1.17}$$

Combining this result with Eq. 4.1.9, we obtain the pressure field as

$$\mathrm{P}(s) = \frac{1}{4\pi}\left|\frac{c(s)cos\theta}{c(0)J(s)}\right|^{1/2} e^{i\omega\int_0^s \frac{1}{c(s')}ds'} \tag{4.1.18}$$

By applying a measurement-based empirical approach, the geometrical spreading loss term could be replaced by a measured beam spread angle with Gaussian beam pattern. Additionally, the attenuation and transmission loss terms are required and this will describe in the Section 4.2. The phase term in Eq. 4.4.18 is the summation of the beam travel time in water-skull-brain layers. The travel time can be derived from ray length divided by the wave speed.

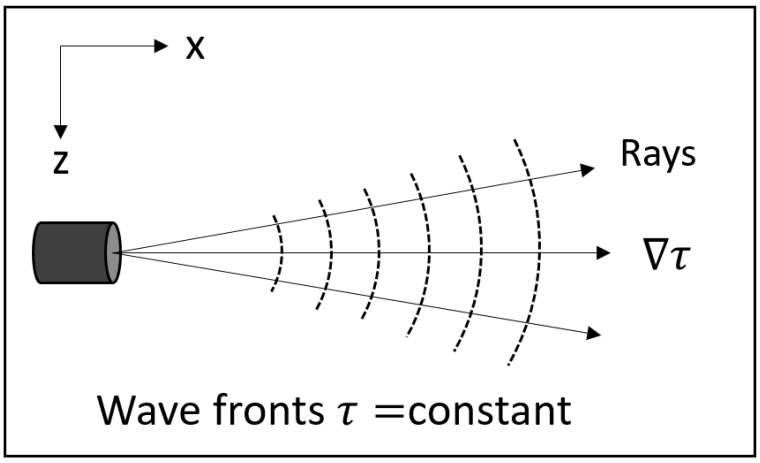

Fig. 4-1 The penetration of plane wave through water-skull-brain medium. (a) The wave beam pass through outer and inner layer of the heterogeneous skull bone. (b) The transmission and attenuation loss of plane wave during penetration of skull bone.

4.2. Focal pressure estimation (Empirical approach)

The abovementioned methods are still in development stage and most of them suffer from large computational cost requirements. The verification of numerous parameter settings should be carefully done. An omnipotent model which could account nonlinearity of nearfield, inhomogeneous tissue property, thermal effect on the tissue and the shear wave in the skull should be developed in order to fully represent the FUS phenomenon. As the objective of this study is not to develop a comprehensive simulation model but to develop a tool which could be utilized as a fast pre-estimation tool with compromised estimation accuracy. In this section, the basic concept of ray based focal pressure estimation will be introduced.

4.2.1. The traveling plane wave model

By assuming a homogenous material property and a constant wave velocity of the medium, the linear, lossless wave equation for the propagation of sound in fluids could be derived as below (LAPWE).

$$\nabla^2 p - \frac{1}{c^2}\frac{\partial^2 p}{\partial t^2} = 0 \tag{4.2.1}$$

This equation could be utilized to represents the propagation of harmonic wave propagating in a homogenous medium with period T and has a temporal dependence given by $e^{i\omega t}$, where $\omega = 2\pi/T$ is the angular frequency and $c = \lambda/T$. The solution of the above wave equation to travel to a positive x direction for a plane wave could be described as following function.

$$p(x,t) = P_0 e^{i(kx-\omega t)} \tag{4.2.2}$$

Where, P_0 is initial pressure and $k = 2\pi/\lambda$ is wave number. By considering real term only, the exponential term could be replaced by cosine function as below.

$$p(x,t) = P_0 cos(kx - \omega t) \quad (4.2.3)$$

This function is representative for the plane wave traveling through a homogeneous medium and a simulated spatiotemporal pressure field is plotted in Fig.4-2.

As shown in top left of Fig.4-4, the propagating plane wave in the space-time domain could be visualized. The attenuation of the acoustic wave in the medium was not considered in this case. An additional exponential term with appropriate attenuation coefficient could account for the lossy medium. The travelling plane wave along a beam path with attenuation term is simulated and illustrated in Fig.4-2.L3 and Fig.4-2.L4. Since a phased array transducer contains hundreds of elements, travel time t, which represents the phase difference from each channel should be included in the pressure along a beam path from a single channel *i* as shown in the following function.

$$p_i(x,t) = P_0 e^{-\alpha x} cos(kx - \omega t) \quad (4.2.4)$$

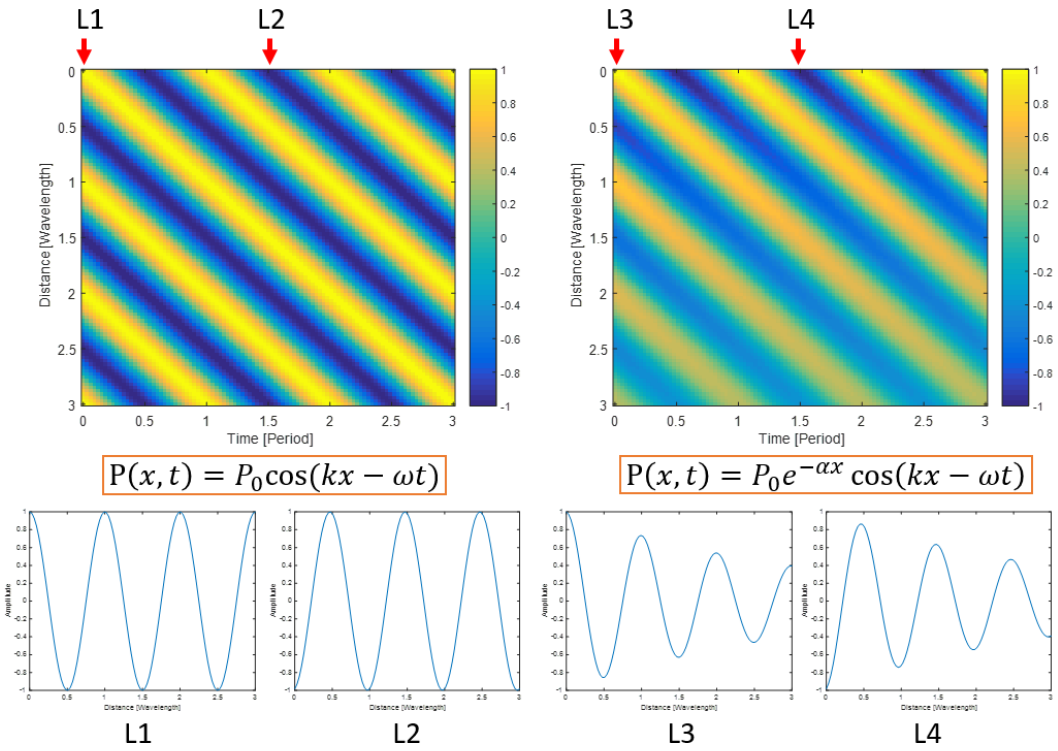

Fig. 4-2 The attenuation simulation of planar wave in longgitudinal propagation. A homogeneous medium assumption was defined. A 100 kHz sinusoid signal is utilized and the initial pressrue was 1. The speed of sound was defined as 1540 m/s and α was defined as -200 to visualized a significant decay.

Snell's law

Snell's law (also known as Snell-Descartes law and the law of refraction) is a formula used to describe the relationship between the angles of incidence and refraction, when referring to light or other waves passing through a boundary between two different isotropic media, such as water, glass, or air (see Fig.4-3). Snell's law states that the ratio of the sines of the angles of incidence and refraction is equivalent to the ratio of phase velocities in the two media, or equivalent to the reciprocal of the ratio of the indices of refraction [59, 60].

$$\frac{sin\theta_1}{sin\theta_2} = \frac{c_1}{c_2} = \frac{\lambda_1}{\lambda_2} = \frac{n_2}{n_1} \tag{4.2.5}$$

There are several ways to derive Snell's law, such as the Fermat's principle [61] and using translation symmetry considerations [62].

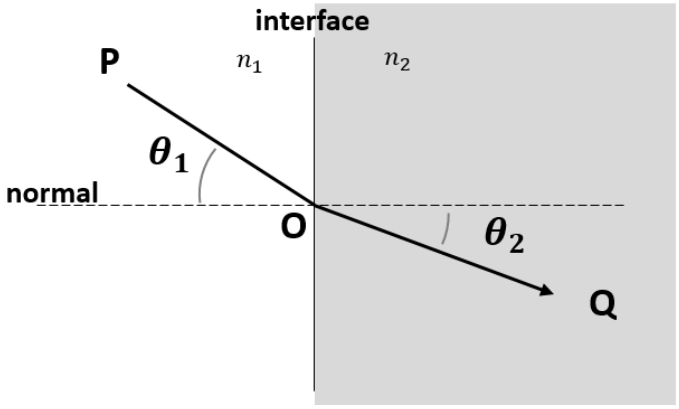

Fig. 4-3 The sketch of a wave penertrating a boundary between two media. The wave is transmitted from a point P through the intersection O and refracted to point Q [63]. The refraction angle is derived with known incident angle and the wave velocity of two materials.

4.2.2. Near field boundary (NFB)

The ultrasound intensity along the beam is affected by constructive and destructive wave interference and this leads to extensive fluctuations in the sound intensity near the source and is known as the near field. Because of acoustic variations within a near field, it can be extremely difficult to accurately evaluate pressure field within this area. The pressure waves are combined to form a relatively uniform front at the end of the near field (or Fresnel region). The area beyond the near field is called the far field (or Fraunhofer region). In the far field, the beam spreads out in a pattern originating from the center of the transducer. The transition between the near field and the far field occurs at a distance, N, and is sometimes referred to as the 'natural focus' of flat transducer [64, 65].

A 650-kHz sound wave has a wave length of 2.3 mm in the 18 ºC water.

$$\lambda = \frac{1481\ \ [m/s]}{650000\ \ [Hz]} = 0.0023\ \ [m] \tag{4.2.6}$$

The simplified near field boundary (NFB) can be derived using the following equation [64]

$$N = \frac{D^2}{4\lambda} or\ \ N = \frac{r^2 f}{c} \tag{4.2.7}$$

Where N denotes the near filed length or transition from near field to far field, D is diameter of the transducer and F is the frequency of the transducer. c is the velocity of sound in the material and it is 1481 m/s in this case.

$$N = \frac{r^2 f}{c} = \frac{(6.0117 \times 0.001\ \ [m])^2 \times 650000\ \ [Hz]}{1481\ \ \left[\frac{m}{s}\right], in\ \ 30℃} = 0.0159\ \ [m] \tag{4.2.8}$$

The derived NFB is 15.9 mm and an attention on this value is paid during following measurement.

4.2.3. The pressure along ray path

In this study, the ray tracing was adopted to simulate the wave beam refraction through three different layers (such as water, skull bone and brain tissue). The refraction angle was computed based on Snell's law. The trajectory of the whole beam through three layers was separated to three sub segments as shown in Fig.4-4. An additional segment, which is the closest vector from target point to a third ray segment, was computed and defined as a fourth ray segment.

The computation of final pressure contribution from single transducer to the target point could be divided into two steps. The first part is computation of the attenuation and transmission loss along the ray until it reaches P_{32} point. Then, the lateral pressure from P_3 to target point is computed based on the measured pressure profile. It is assumed that the superposition of the pressure contribution from every transducer channel to the target point is the final pressure on the target point. It could compute a volumetric pressure distribution by changing the location of the target point in a defined volume.

The phase of propagating wave arrive to P_3 could be derived on each transducer channel as well. This information is crucial while computing the phase for the phase correction to efficiently superpose pressure to the target point. This will be discussed in detail in the latter sections.

As abovementioned, the simulation volume was simplified as a homogeneous three-layer structure. The acoustic wave was emitted from the surface of transducer and traveled through media of water, skull bone and brain. The refraction phenomenon could be accounted by implement the Snell's law on traveling plane wave model. The sketch of the travelling wave on three-layer model was illustrated in Fig.4-4.

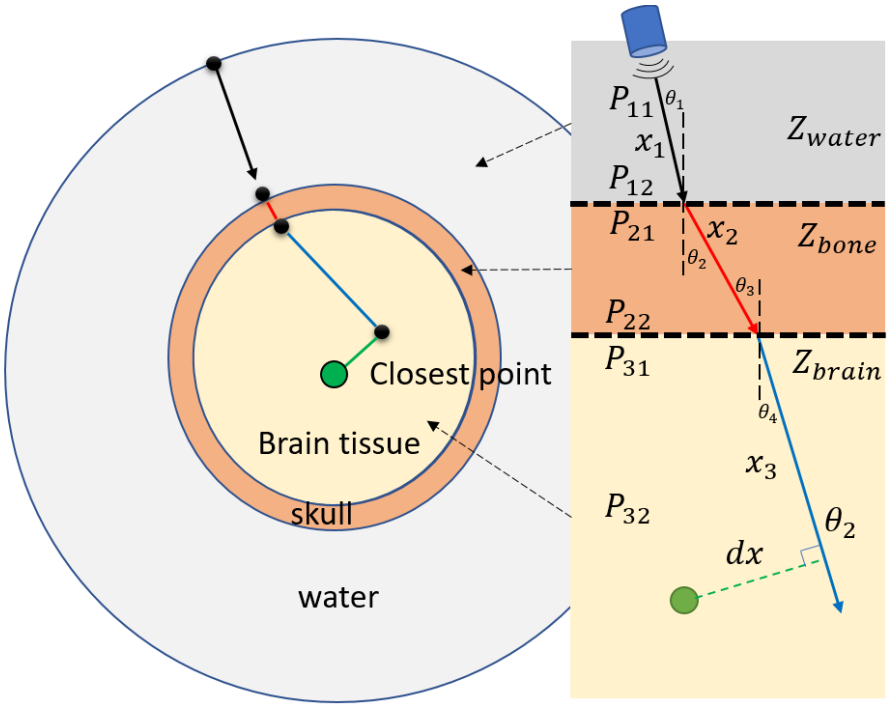

Fig. 4-4 The three-layer model used in proposed ray method. Two major refractions were accounted with a homogeneous medium assumption on water-skull-brain model. The closest distacne from target point to the second refracted ray, dx, was treat as the lateral distance from center of the beam.

By assuming the pressure emitted from the surface of transducer is P_{11}, it is possible to compute the pressure contribution from the single channel to the observation point (green dot in Fig.4-4). A total of two coupled refractions and reflections, on the outer and inner skull layers, could be accounted along the beam path on this model. Only the refraction and transmission on each layer was taken into account and the reflected wave was ignored because of its negligible contribution to the propagating wave. Thus, the pressure of plane wave traveled to the outer surface (point P12 in Fig.4-4) could be represent as following equation.

$$P_{12}(x_1, t) = P_{11} e^{-\alpha_w(\omega) x_1} e^{i(k_w x_1 - \omega t)} \tag{4.2.9}$$

Where, $\alpha_w(\omega)$ is the acoustic attenuation coefficient in the water and k_w is the wave number in the water. The ray segment from P_{11} to P_{12}, which is the ray path in the water, was represented as x_1 and the phase of the plane wave travel on this path could be derived from traveling time *t*. The initial pressure was defined as P_{11}.

The reflection coefficient of the wave, R_{12} travelling from water to skull could be computed by using the following function.

$$R_{12} = \frac{\rho_2 c_2 \cos\theta_1 - \rho_1 c_1 \cos\theta_2}{\rho_2 c_2 \cos\theta_1 + \rho_1 c_1 \cos\theta_2} \tag{4.2.10}$$

The incident angle and refraction angle were denoted by θ_1 and θ_2, respectively. The density and velocity of each medium was represented by ρ and c with the corresponding material numbering. Then, the transmission coefficient of the wave could be written as following.

$$T_{bobr} = 1 + R_{12} \tag{4.2.11}$$

The variation of the reflection and transmission for this case was simulated and plotted in Fig.4-5. The density and wave speed in simulation were defined as 1482 m/s and 1000 kg/m^3 in water, and 3900 m/s and 1900 kg/m^3 in the skull, respectively.

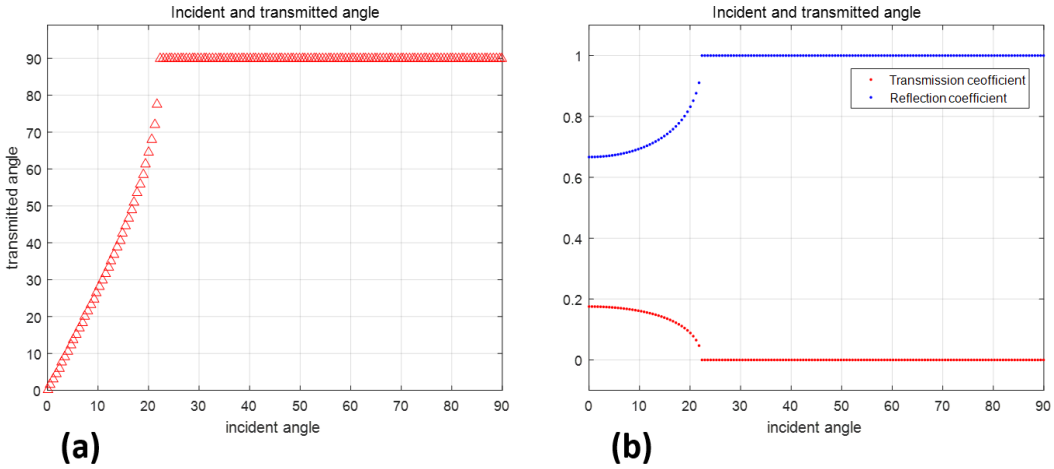

Fig. 4-5 The variation of transmission and reflection coefficient while wave propagate from water to skull was simulated by defining the incident angle as a variable a) The transmission angle based on Snell's law. b) The variation of transmission coefficient and reflection coefficient. The density and wave speed were defined as 1482 m/s and 1000 kg/m^3 in water, and 3900 m/s and 1900 kg/m^3 in the skull, respectively.

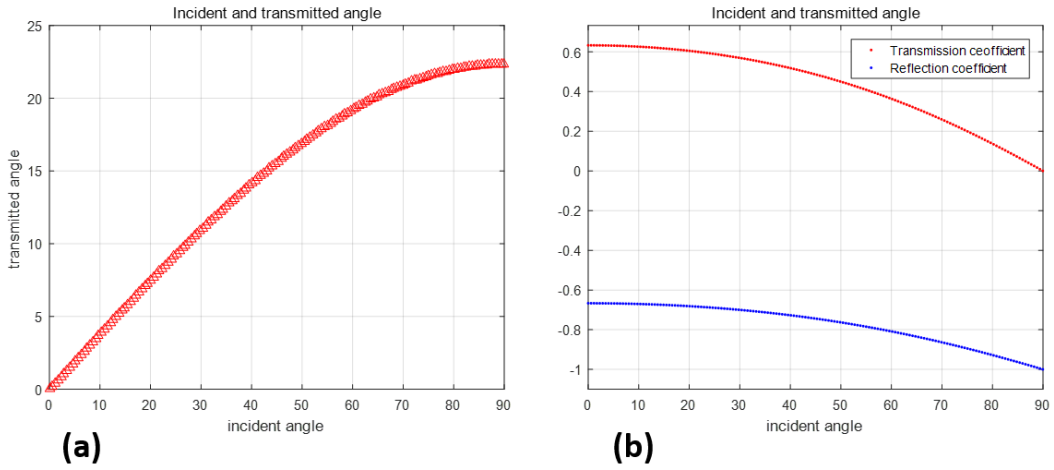

Fig. 4-6 The transmission angle calculated based on Snell's law while wave propagate from skull to brain with derived transmission and reflection coefficient. a) The transmission angle become saturated while the incident angle is greater than the critical angle b) A uniform amplitude of the coefficient while the incident angle is greater than critical angle was simulated. The density and wave speed were defined as 1482 m/s and 1000 kg/m^3 in water, and 3900 m/s and 1900 kg/m^3 in the skull, respectively

It should be noted that, the reflection and refraction coefficients described above were the case of the wave travelling from a medium of high speed of sound to lower speed of sound. The opposite case is from water to bone. The relation between reflection coefficient and transmission coefficient is a form as below.

$$T_{wb} = 1 - R_{23} \tag{4.2.12}$$

Thus, the reflection coefficient becomes [66] and the simulated result was plot in Fig. 4-6

$$R_{23} = \frac{\rho_3 c_3 \cos\theta_3 + i\rho_2 c_2 \cos\theta_4}{\rho_3 c_3 \cos\theta_3 - i\rho_2 c_2 \cos\theta_4} \tag{4.2.13}$$

If the amplitude of the reflection coefficient is 1 while the incident angle θ_3 is greater than the critical angle and the wave reflects totally,

$$|R_{23}| = 1 \;\; while \;\; \theta_3 > \theta_c \tag{4.2.14}$$

Thus, the pressure on P_{32} (which is the projection of observer point to the ray segment x3) could be represented as below.

$$\begin{aligned} P_{32}(x,t) = P_{11} e^{-\alpha_w(\omega)x_1} e^{i(k_w x_1 - \omega t)} \cdot (T_{wb}) \\ \cdot e^{-\alpha_{bo}(\omega)x_2} e^{i(k_{bo} x_2 - \omega t)} \cdot (T_{bobr}) \\ \cdot e^{-\alpha_{br}(\omega)x_2} e^{i(k_{br} x_3 - \omega t)} \end{aligned} \tag{4.2.15}$$

Where, α_{bo} and α_{br} are the attenuation coefficients of wave in the bone and brain, respectively. The pressure P_{32} presents the central peak pressure of the closest point on the acoustic beam to the observer point. The final single channel contributed pressure to the observer point could be derived by extracting the corresponding pressure value from beam profile on lateral direction. It is possible to derive the contributed pressure on the observer point based on central pressure if the lateral beam profile is known. In the following section, the attenuation coefficient in water and the beam divergence angle with and without skull were acquired based by hydrophone measurement. These measured parameters will be implemented into the ray tracing solver to perform the focal pressure estimation.

4.3. Measurement based calibration

The attenuation along the ray and the beam divergence angle are key parameters to predict the focal quality of focused ultrasound sonication. The appearance of skull bone may alter the attenuation and the beam width with refraction. The objective of this section is to investigate the effects of skull bone on alteration of beam divergence angle and the pressure decay along beam direction in order to increase accuracy of ray approximation.

The transducer channel 71 was utilized to emit 3W of electric power (1.95W acoustic power) because this channel was physically located in the most bottom of the hemisphere transducer. The pressure field without skull was acquired on various scanning planes (in Fig.4-7.a, scanning depth = 140mm, scanning plane number = 15). In order to define exponential decay of pressure amplitude along beam path, fifteen cross-sectional planes were scanned along the beam direction of the selected transducer channel. The location of the selected channel was estimated based on the channel pattern figure from the work station software. However, the spherical shape of the transducer and the linear scanning limit of the AIMS system make it difficult to perfectly scan a perpendicular cross-section along the beam path. Thus, a sufficiently large scanning area (61mm by 61mm) which could cover focal shift caused by the oblique angle between the scanning path and the beam direction was defined (Fig.4-7.b). A maximum value from the measured 2D pressure field was collected as a representative pressure of the corresponding distance from transducer. A peak pressure on the median filtered image was also collected for comparison study (Fig.4-7.b).

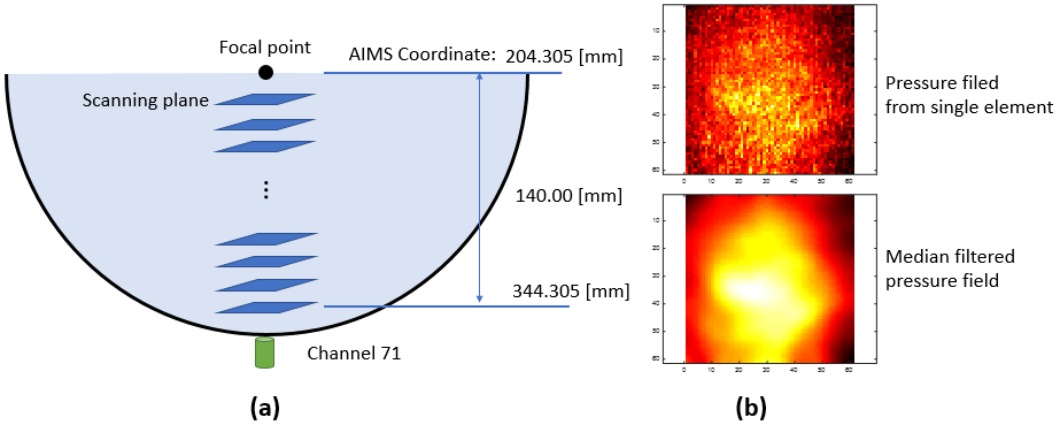

Fig. 4-7 (a) The sketch of scanning plane and selected transducer channel (b) the hydrophone scanned pressure filed and medial filtered pressure field from one of the scaned data.

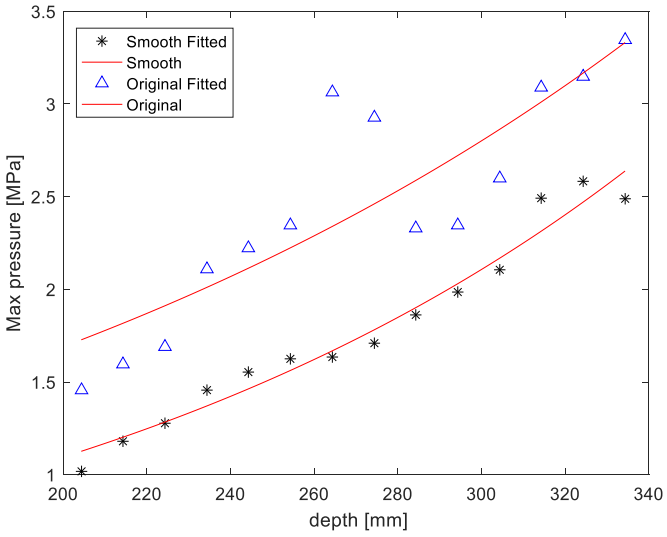

Fig. 4-8 The measured pressure decay of single element beam profile. The scaning volume start from focal plane to the closest scannable plane and the total depth of scane was 130 mm.

As Fig.4-8 shows, the measured pressure decay follows an exponential curve on both non-filtered and filtered case. The exponential coefficient α of fitted curves from non-filtered and filtered case is 0.0655 Np/cm and 0.0505 Np/cm respectively and this value is corresponding to 0.569 dB/cm and 0.439 dB/cm. This measured coefficient was used in the ray tracing simulation of focal quality estimation study.

The relationship between actual acoustic pressure and sonication power was studied. In order to define the relationship, we placed the hydrophone on a closest plane in the far field that is approximately 23 mm from selected transducer element.

Ten cross-sectional scans were acquired under various sonication pressure setting (from 0.5W to 4W). The electrical power and acoustic pressure relationship was derived and plot in Fig.4-9. The filtered curve, of course, shows lower value of peak pressure than the original scanned data. A saturation of maximum pressure was observed when the electrical power was greater than 2W, and the peak acoustic pressure remains at 3.69 MPa and 2.95 MPa for non-filtered and filtered case, respectively. This is crucially important during numerical simulation was imported as the initial condition of simulations.

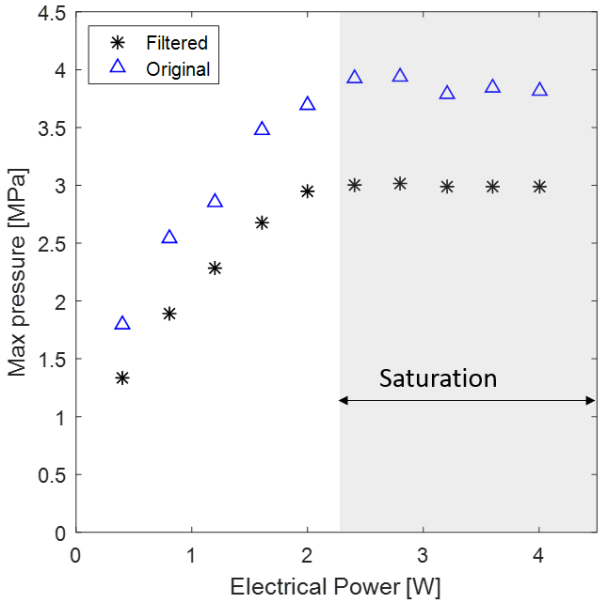

Fig. 4-9 The relationship of electrical power and actual acoustic pressure. A saturation of maximum pressure could be observed while the electrical power was greater than 2W.

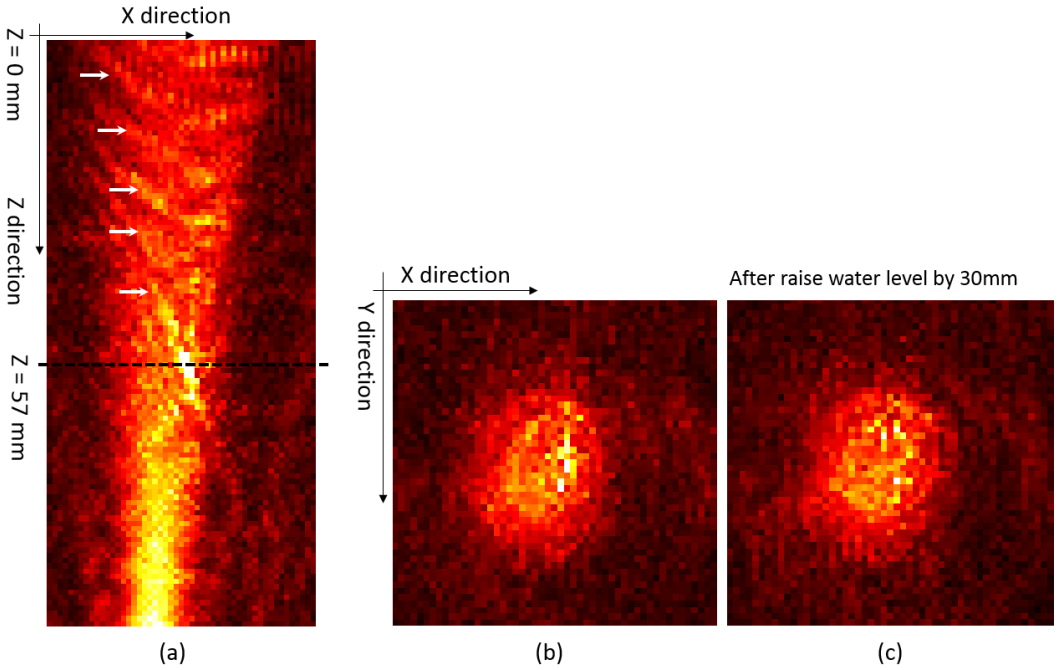

Fig. 4-10 (a) Longitudinal pressure field along beam path of single element, the disturbance pattern captured in hydrophone scaned preesure field were marked as white arrow (b) XY plane pressure field on Z=57 mm depth (c) XY scan after raise water level by 30 mm

A relatively large amount of fluctuation was observed in the measured pressure curve from the depth 260 mm to 280 mm in Fig. 4-10. An investigational scanning was performed in the longitudinal direction along the beam path (see Fig. 4-10-a). A high peak value was captured by this scan which is even higher than the maximum pressure value which was measured on the closest cross-sectional plane from the transducer face. An additional cross-sectional plane was scanned after raising the water level by 30mm to confirm if the high peak value still exists or changes (Fig. 4-10.c). As Fig.4-10.b and Fig.4-10.c show, the pattern of the high peak was changed by water level shifting and this result proves that the high peak is a superposition of a reflection wave from the water surface and the propagating wave from transducer. This also explains the reason for the existence of an unknown pattern which is marked using white arrow in Fig.4-11.a. Appropriate changing of the computation window on digitized signal train in the raw data could remove the reflection effect and improve the pressure field measurement which provided a smoother figure as Fig.4-11 shows.

To our knowledge, the 2D hydrophone scan data was constructed by collecting certain amount of signal while the needle hydrophone was stopped at a predefined location then shifted to the next location to collect another signal train. The maximum voltage data from a signal train was multiplied by a calibration value, the voltage to pressure ratio, and the result was mapped to a 2D image.

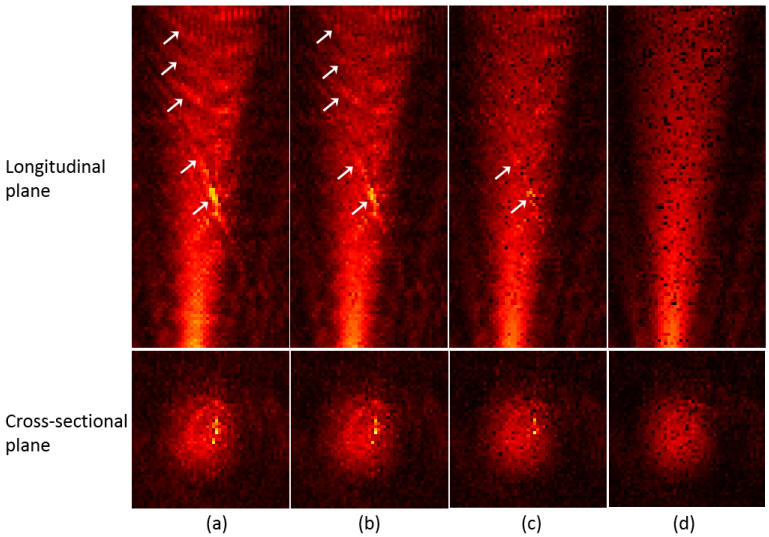

Fig. 4-11 Reconstructed pressure field from hydrophone scanned raw data. The upper row is longitudinal scan data and lower row is cross-sectional scan data which is the same data as shown in Fig.26. The window size used in four cases were (a) full data (b) 25 sample (c) 20 sample (d) 17 sample.

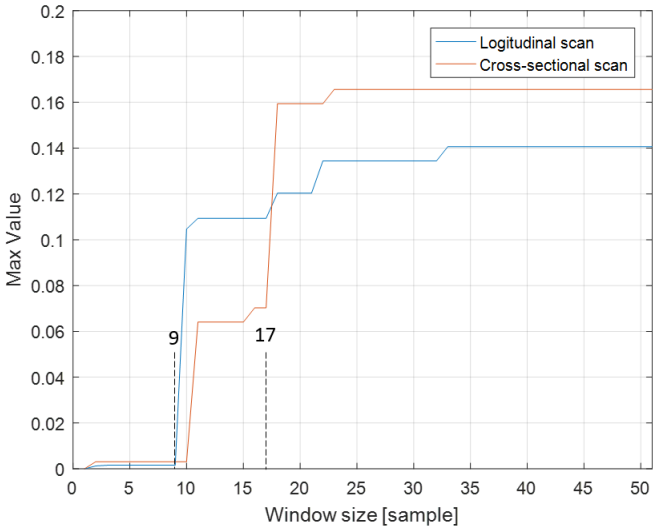

Fig. 4-12 The variation of max pixel value based on adopted window size. The shape of beam is visible start from window size 9 and the water surface reflection is start to appeared when window size larger than 17.

Theoretically, a narrowed window for calculation of the max signal may neglect the water-surface-reflected signal. A reconstruction was implemented on the raw data with various window sizes. A pixel of the 2D pressure scan was reconstructed by giving a window to the signal train and a maximum value without calibration factor was collected and mapped in the 2D domain. As Fig.4-12 shows, the patterns which were marked by white arrows were removed while the window size was decreasing. This effect was also observed in cross-sectional scan data with same processing method. Furthermore, an optimum window size (36 samples) was derived by computing the maximum value on different window size. As Fig.4-12 shows, the head of signal train was arrived when the ninth sample was digitized and the peak that from reflected pressure was appeared after sample 17.

Based on these investigations, it is clear that the abnormally high peak is a composition of multiple pressure waves that have different propagation speed. There are several possibilities to explain what causes this wave different. A superposition and constructive wave seems to be the most reasonable candidate to explain this. A superposition of propagating wave from source and water-surface-reflected wave is the most reasonable explanation. However, constructive interference with a different propagating wave with different frequency may also be a possible cause of this phenomenon. A carefully defined window size should be applied while measuring the pressure field using a hydrophone, especially when close to the water surface.

4.4. Single element pressure field measurement

The human skull was placed between activated single channel and the hydrophone. The cross-section of the acoustic beam through the skull was scanned. A comparison of the beam pattern with and without skull was described in this section. An approximate approach for divergence angle was discussed and the measurement based divergence angle was used in

subsequent simulations.

4.4.1. Single element pressure field measurement with skull

The skull assembly was carefully mounted on the extended cylinder reservoir using MR compatible screws (see Fig.4-13). A total of 10 scanning planes were acquired and the scanning range was covered by 50 mm on both X and Y axis. The scanning depth of focal plane was limited by the large aperture size of the skull and the available depth was 30 mm for 50 mm by 50 mm scanning area setup. Further deeper scanning was achieved by reducing the scan area to 30 mm by 30 mm and the total depth of scan was 40 mm. For safety reason, we iteratively shifted the hydrophone to the deepest safe position on each corner of desired scanning area and made sure the tip of hydrophone was not physically contacted with the skull bone (Fig.4-14.b).

The pressure field pattern was strongly diffused and some unknown nonlinear strips appeared in these measurements. The attenuation coefficient along the beam was not computable. This was possibly caused by the constructive wave refracted by inhomogeneous skull acoustic properties. However, a recognizable beam cross-section was captured on the entire plane as shown in Fig.4-15.

It is clear that the acoustic wave from a single element maintains a beam-like shape even after it penetrates the skull bone. It is an evidence to support the feasibility of the ray method to estimate the focal quality of FUS sonication. Thus, the beam dispersion angle from this data could serve as guidance for the lateral pressure pattern. The -6dB beam width was derived from these measurements and the beam spread angle was presented in following section.

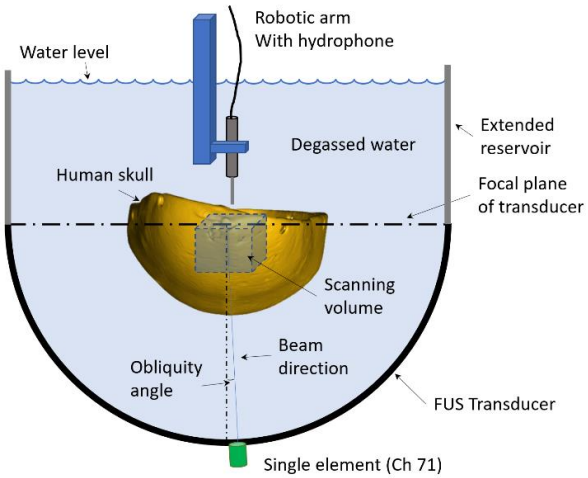

Fig. 4-13 The sketches of the experiment setup. A single transducer channel was activated to emit 650 kHz acoustic wave. A robotic arm controlled hydrophone scan was implemented on the focal plane as shown in figure.

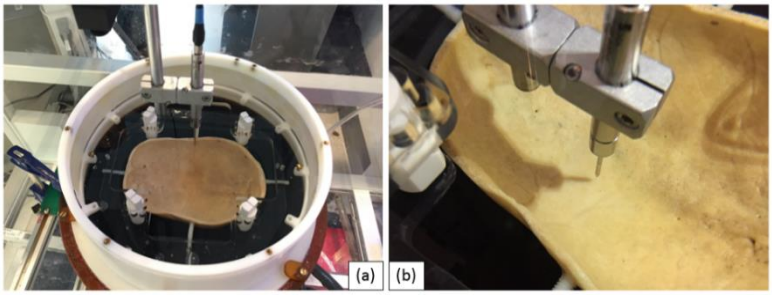

Fig. 4-14 (a) Secure the skull assembly to the top head reservoir which fastened on the top of the FUS transducer (b) Iteratively move the hydrophone to the corner of the scanning plane to make sure that there is no contact between hydrophone tip and skull bone

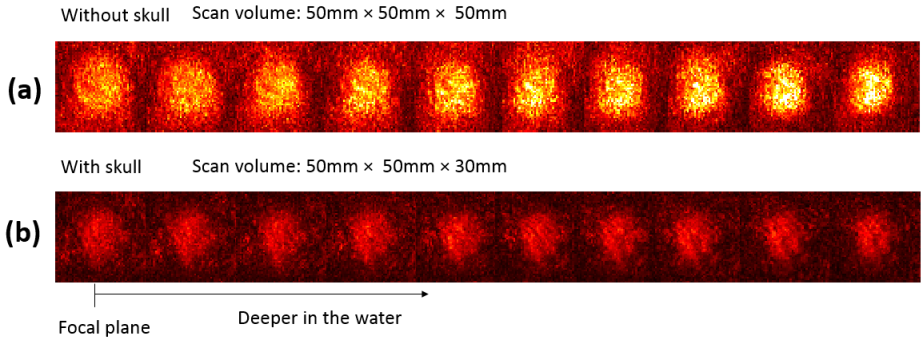

Fig. 4-15 (a) The cross-sectional scan of single element beam without the skull placed between transducer and hydrophone. The scanning area was 50 mm by 50 mm on XY plane and the scanning depth was 50 mm on Z axis (b) The cross-sectional scan of single element beam with skull placed between transducer and hydrophone. The scanning area was 50 mm by 50 mm on XY plane and the scanning depth was 30 mm on Z axis

4.4.2. Simplified transducer beam spread (Approximation)

The energy in the beam spreads out as it propagates through the medium. The phenomenon is usually referred as a beam spread but sometimes as a beam divergence or ultrasonic diffraction. Beam spread is a measurement of the whole angle from side to side of the main lobe of the sound beam in the far field. Beam divergence is a measure of the angle from one side of the sound beam to the central axis of the beam in the far field. Therefore, beam spread is twice the beam divergence [67] The beam spread is largely determined by the frequency and diameter of the transducer. Beam spread is greater for a low frequency transducer than for a high frequency transducer. As the diameter of the transducer increases, the beam spread will be reduced [68].

For a flat piston source transducer, an approximation of the beam spread is calculated as a function of the transducer diameter, frequency, and the sound velocity in the liquid or solid medium. The derived angle represents a measure from the center of the acoustic axis to the point where sound pressure is decreased by a half (-6dB) to the side of the acoustic axis in the far field.

$$d = 12.6 \text{ mm}; \quad sin\theta = 1.22\frac{\lambda}{d} = 1.22\frac{v}{df} \tag{4.16}$$

$$\theta = \text{asin}\left(\frac{1.22\lambda}{d}\right) = 0.26 \ \ radian = 14.9 \ \ degree \tag{4.17}$$

As a result, the beam divergence angle from centerline to a point where signal is half pressure is 14.9 degrees.

4.4.3. Beam divergence measured from single element

A median filter was applied on the measured pressure field and a -6dB contour based on the peak pressure value was computed to derive the radius of beam (Fig.4-16). The mean value of the distance from centroid to each contour edge was treated as the radius of the beam. The radius of each plane was collected with and without skull. The slope angle of the fitted line was assumed as the beam angle (Fig.4-17). Note that the scanning depth (50 mm) for non-aberrated case (without skull placed) was 10 mm deeper than the aberrated case (with skull attached) and the radius plotted in Fig.4-17.

As result, the derived radius from various scan planes was well fitted by a line, and the beam angles of aberrated (with skull) and non-aberrated (without skull) cases were 10.86 degree and 13.21 degree, respectively. These are smaller than the angle computed based on the simplified approach. This measurement-based angle was implemented in the ray simulation which could serve as a guide line for the beam pattern computation in the lateral beam direction. The refraction under different incident angle may also affect the beam refraction angle and the beam divergence. A fixed transducer-hydrophone setting with various incident angle by tilting the skull cap could be helpful for further confirmation of the correlation between incident angle and beam divergence. Further, it is also desirable to correlate the CT image derived skull intensity with the bema divergence.

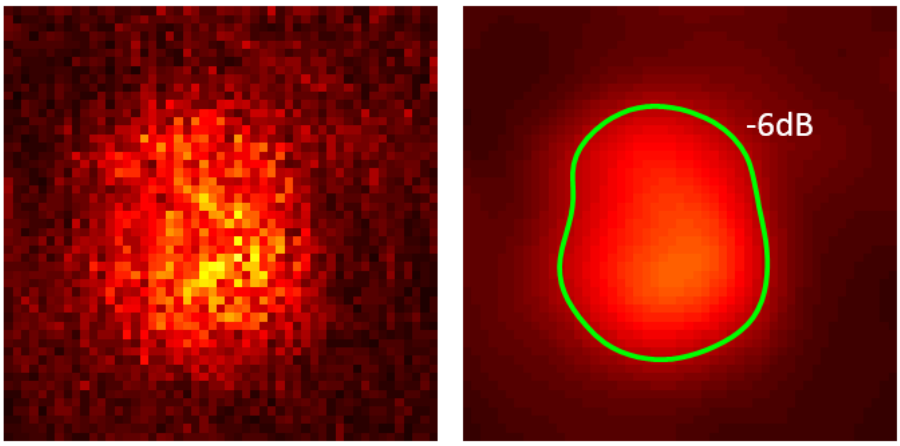

Fig. 4-16 (a) Hydrophone measured pressure field on Z=40 mm plane (b) Median filtered pressure field with -6dB contour based on the peak pressure value.

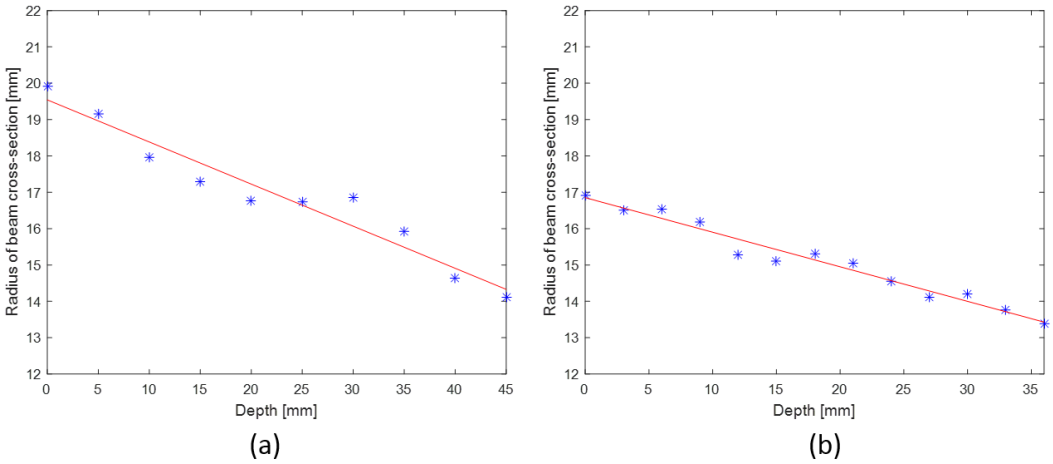

Fig. 4-17 (a) The beam divergence angle without skull (b) the divergence angle after refracted by skull bone

4.5. Focal Pressure estimation simulation

The focal pressure simulation using the ray method was implemented based on the measured data. Water, skull and brain tissue were all treated as a homogenous medium and the speed of sound, density and attenuation coefficient were referred from literature [69] except the density of skull bone. The sound speed in skull bone was utilized as the optimized value from phase correction experiments. The divergence angle of 13.21 degrees was utilized as a guidance to the lateral pressure pattern. The parameters in Table 5 were imported to a ray based simulation model and the computed focal pressure distribution was illustrated in Fig.4-18. An arbitrary central and frontal targets were selected to show the difference of focal pressure pattern between two extreme cases.

Table. 5 The parameters used in ray simulation and phase correction computation. The divergence angle was measured from single channel sonication

Parameters	water	Skull	Brain
Speed of sound [m/s]	1482	2750, 2150	1562
Density [kg/m3]	1000	1900	1030
Attenuation coefficient [dB/cm]	0.565	2.7	0.6
Center frequency [MHz]	0.65		
Divergence angle [degree]	13.2142		

As Fig.4-19 shows, most of the beam were able to penetrate through the skull in case A and resulted in a relatively concentrated focal spot. However, as the target point moved toward frontal direction, a considerable number of rays were not able to transmit into the brain because of the large incident angle. The decay of the focal pressure while the target point is away from the center was investigated. Ten target points were defined and the simulated peak pressures on the target locations were compared. The corresponding target location with the measured peak pressure was illustrated in Fig.4-20.

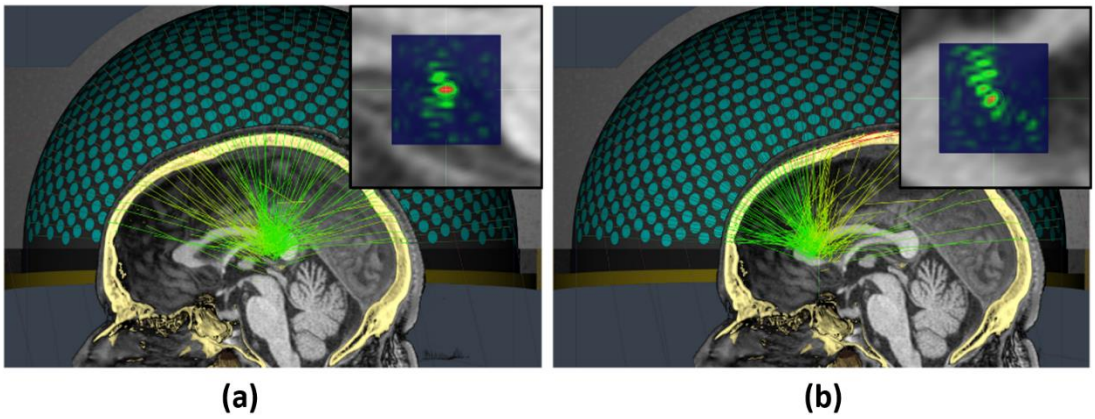

Fig. 4-18 (a) The refraction of beam when targeted at the central location (b) The refraction of beam when targetting on a frontal target.

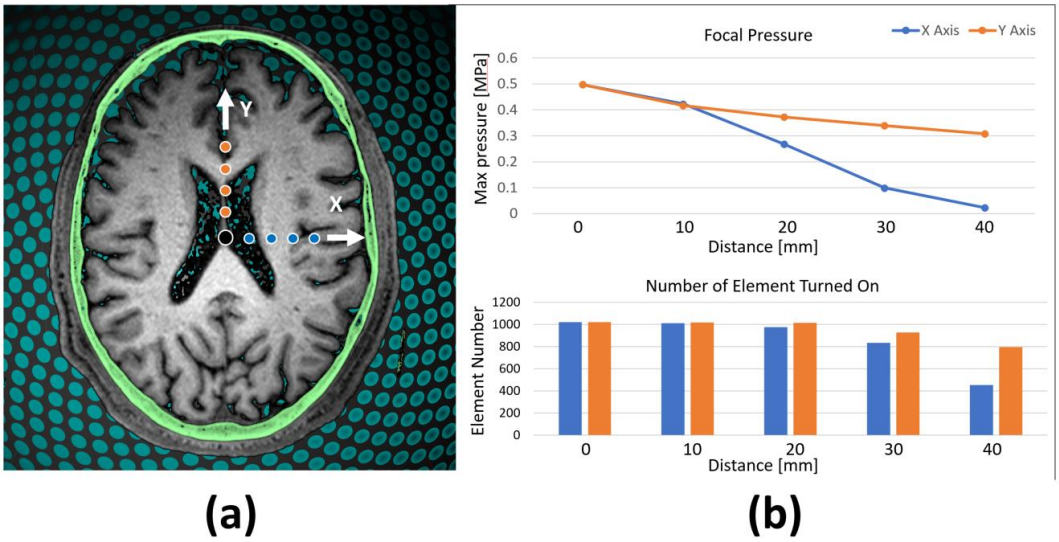

Fig. 4-19 (a) The beam divergence angle without skull attached (b) the divergence angle after refracted by skull bone

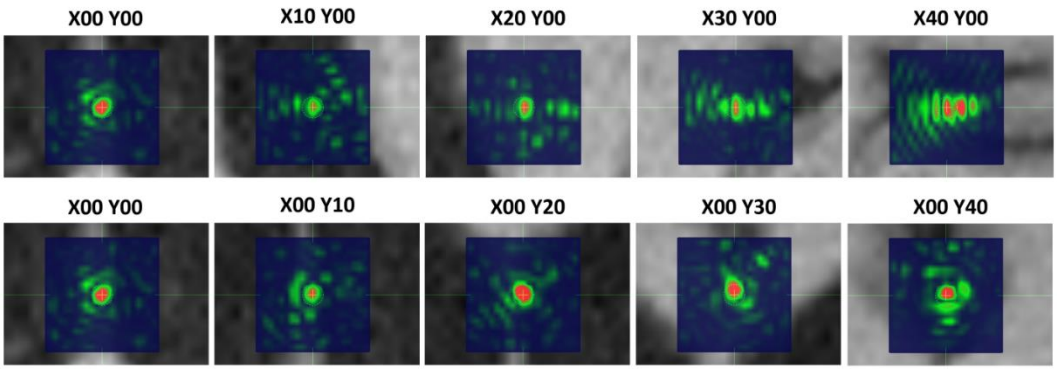

Fig. 4-20 The simulated focal pattern on 10 different target locations. The color bar was auto-scaled to emphasize the focus.

As the simulation results are shown in Fig.4-20, the focal pressure is decreased on both X and Y axes while the target moves away from the center. A greater decrease in the focal pressure on X axis could be seen in upper chart in Fig.4-19.b. The incident angle increases while moving the target toward the skull from center. The decrease of the focal pressure on both axes could be explained by the decreasing transmission coefficient caused by increased incident angle. Furthermore, the number of active transducer channels could be a reason for the pronounced decrease rate on the X-axis. As lower chart in Fig.4-19.b shows, the decrease of the focal pressure is in accordance with the decrease in the number of active channels. The ray model intentionally turns off the transducer channels which have an incident angle greater than the critical angle. This is why the target along X axis has greater rate of decrease. The simulated focal pressure on different target location is illustrated in Fig.4-20. The focal pressure pattern was more distorted on X axis than on the Y axis.

Chapter 5

RAY BASED PHASE COMPENSATION

The aberrated phase produced by the skull was corrected based on the developed ray method. A brief review of the previous study is described and then the basic concept of the ray method in this study is described in detail. The phase correction data from the ray method was imported to the FUS system. The focal pressure was scanned using a needle hydrophone and the improvement of the focal quality was discussed.

5.1. Phase compensation

5.1.1. Baseline phase

The geometrical coordinate of each channel from TcFUS transducer was measured by manufacture and stored in an INI file in the workstation of the ExAblate Neuro system. Distance from each channel to the geometrical center was calculated based on the INI file and plotted in Fig.5-1. As shown in Fig.5-1, 11 channels were referred to a single coordinate (X:155, Y:0, Z:150) and serves as a registration marker. The channel-to-center distance from the rest of the channels shows a periodic variation and this may be an initial phase difference on each channel.

The control software in the workstation on InSightec ExAblate Neuro system provides a preview of color mapped phase pattern as shown in Fig.5-2.a.

The baseline phase seems to be measured after the transducer manufacturing procedure and saved in a safety file and utilized to compensate the manufacturing error in the background. The workstation software also provides an import function to load customized phase into system. This allows us to sonicate using simulated phase from the developed software. In order

to check if the software actually loads a customized phase file, a ‘Z’ letter was mapped on the transducer pattern and the phase of the channels lie on the ‘Z’ letter was set to 1 π and the rest of the channels were set to 0 π (Fig.5-2.b). The file loaded into workstation software and the capture of the plotted phase was shown in Fig.5-2.c.

The aforementioned 11 marker channels served as an indicator to relate the transducer coordinate from two different systems (the transducer coordinate saved in INI file and the transducer plotting in InsighTec software). It allows us to pre-plot and to verify the simulated phase in a third-party software like Matlab before load this to the sonication system.

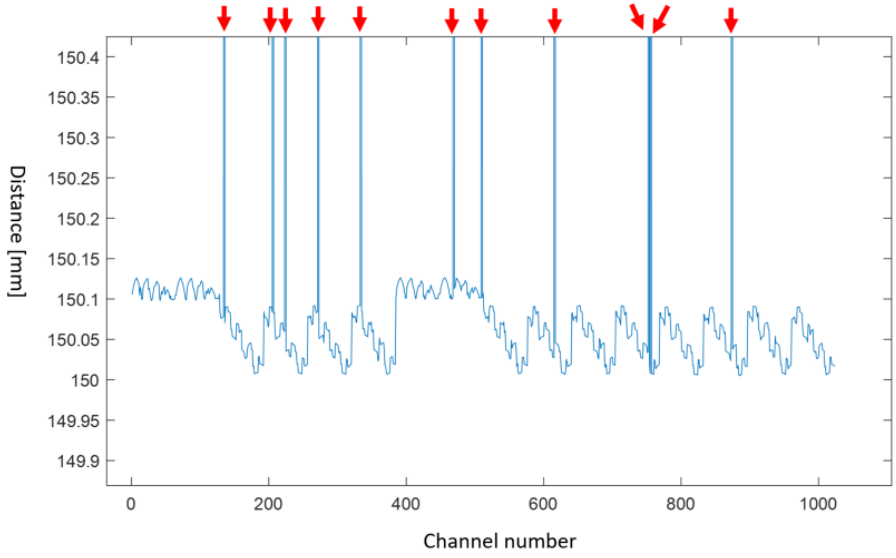

Fig. 5-1 The distance from each transducer channel to geometrical center of a hemisphere transducer. A periodic variation of the distance was visualized. This is an evidence to show the baseline difference of the distance of each transducer from the geometrical center. The geometrical reference was marked using red arrow.

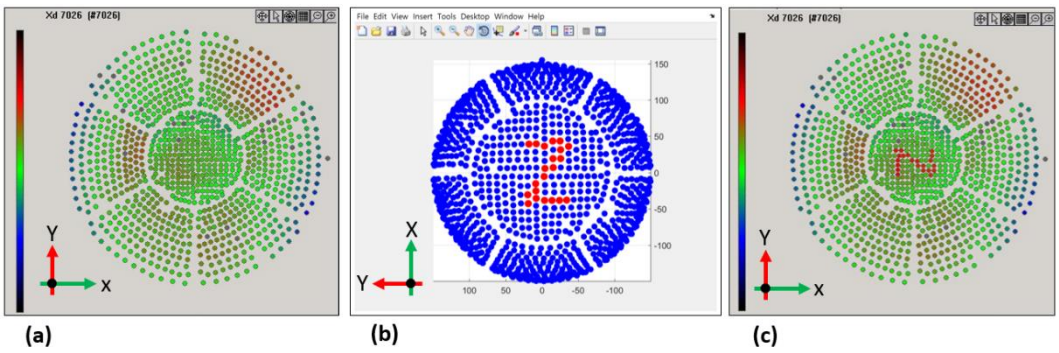

Fig. 5-2 a) The baseline phase mapping in workstation of InSightec ExAblate neuro system. The unit of the phase is Radian. b) A customized 'Z' letter mapped on transducer pattern in Matlab c) The loaded pattern with the baseline phase in the workstation software.

5.1.2. Refraction accounted phase compensation

An analytical phase compensation as used in the Insightec system was implemented using a ray tracing technique (Fig.5-3.a). For a given source location (target point), the delay term for each receiver was determined by analyzing the longitudinal sound speed profile within the skull along the ray between the source location and the center of the receiver element [42]. The skull delay term for each channel element was calculated as the difference between the trans-skull-time-of-flight estimated using this approach, which ignores both reflection and refraction effects, and the corresponding water-path case.

In this study, a phase compensation method accounting refraction phenomenon was implemented. As shown in Fig.5-3.b, the skull induced refraction could be computed in the developed ray tracing platform based on Snell's law. The dual refraction on outer and inner skull layer was captured and the phase difference from each channel was derived from the difference of the refracted ray length.

An example of ray tracing, accounting for refractions, using the developed software is plotted in Fig.5-3. The lengths of ray segments lying on the skull (red ray segment in Fig.4-6) from each channel were collected and saved as Δd. The relevant phase was computed by dividing the ray segment to pre-defined speed of sound on skull bone c_{skull} as shown below.

$$\text{phase} = 2\pi \cdot f \cdot \left(\frac{\Delta d}{c_{skull}}\right) \tag{5.1}$$

The key parameters which influence the phase computation in this proposed method are the ray segment length and the speed of sound in skull bone. The ray segment length is dependent on the refraction angle based on Snell's law. Fortunately, the refraction angle is derived from the ratio of the speed of sound from adjacent two media (water and skull bone). In other words, the skull CT image derived phase is directly and/ or indirectly related to the speed of sound in skull bone. It is well known that the acoustical parameters of skull are

varying as a function of location within the bone [7, 70, 71]. The speed of sound could be derived from skull CT image based on an empirical approach[69, 72]. However, the CT image acquired in this study does not provide the correct Hounsfield unit of image voxel and the sound speed of skull bone could not be derived from the collected CT image. An optimal wave speed was selected by an empirical approach surveying various wave speeds for skull bone. The selected optimal value was utilized and focal plane scanning was implemented on each case. Moreover, two separated wave speed of skull bone were utilized. One of them was utilized to calculate refraction angle, which directly affect Δd, and the other was utilized as c_{skull} in aforementioned formula.

The 3D transducer pattern projected on XY plane and the compensation phase computed by the refraction accounted ray method were mapped over the corresponding transducer channel location (see Fig.5-4).

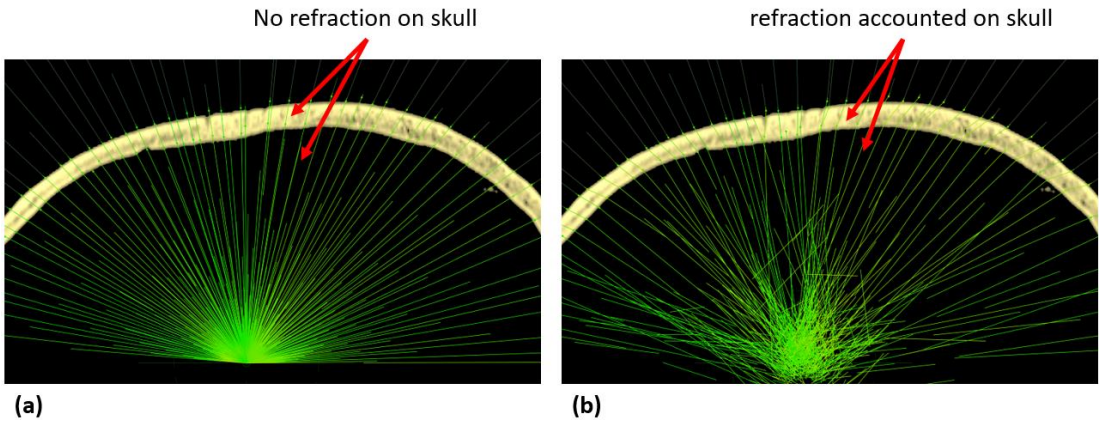

Fig. 5-3 The skull bone induced refraction was computed and visualized in developed software in 3D. The speed of sound in water and skull bone was set as 1482 m/s and 2742 m/s in these two cases.

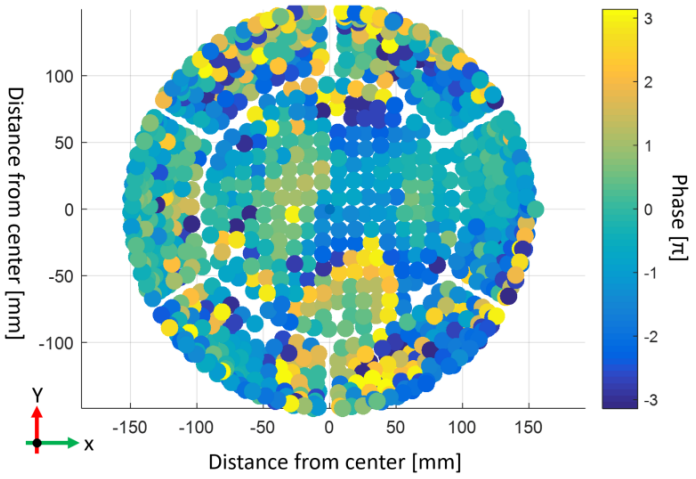

Fig. 5-4The color mapping of computed phase on corresponding channels. The range of the pahse was color mapped in $-\pi$ to $+\pi$. A summation of this pahse map and the baseline phase (see Fig.38-a) caused by manufacturing error was applied before sonication.

5.2. The focal pressure improvement

Two cadaver skulls (Department of Neurosurgery, University of Virginia, US) were used and the CT scans were acquired using GE LightSpeed VCT in hospital of University of Virginia (UVA). The volume image was saved as a DICOM file and then imported in Amira software for post-processing. The reconstructed iso-surfaces of two skulls are shown in Fig.5-5. The simulation and experimental verifications for ray based phase compensation were implemented on these two skulls.

A HNA hydrophone (HNA-0400, ONDA, CA, US) with 1 to 10 MHz frequency range was connected to a pre-amplifier (AH-2020-DCBSW, ONDA, CA, US) and the signal was digitized by an Oscilloscope (Agilent DSO7012B, Keysight Tec., US) under a codded sequence. A triggering cable from the CPC (controller PC in machine room) was connected to an Oscilloscope and the XYZ positioner was controlled by a Soniq software (Soniq 5.1 version, ONDA, CA, US) through an electric motor drive system. As shown in Fig.5-6, the XY plane (horizontal plane of transducer) scanning was implemented on two different scanning sizes, 10 mm by 10 mm and 20 mm by 20 mm. An average scanning time of 5 minutes and 20 minutes were required for 10 mm by 10 mm and for 20 mm by 20 mm, respectively.

The focal plane was searched by adjusting the scanning plane on three axes in order to capture the maximum focal pressure. Once the center line of hydrophone scanned plot lies on the focal point of FUS transducer, as shown in Fig.5-6.a and Fig.5-6.c, we can assume a registration between the AIMS system and transducer is configured.

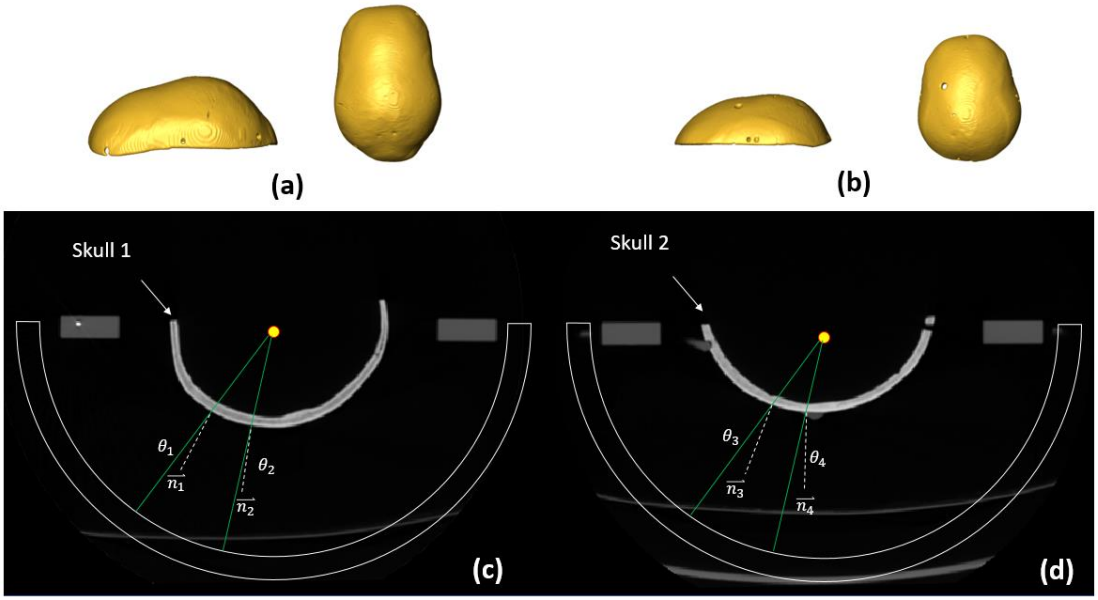

Fig. 5-5 (a)(b) The reconstructed iso-surfaces of two collected skulls. (c) The incident angle θ_1 and θ_2 in skull 1 setting has smaller value which results better transmission of the propagating wave (d) In contrast, skull 2 has relatively larger incident angle as shown θ_3 and θ_4. The normal vector of the incident angle was defined as n.

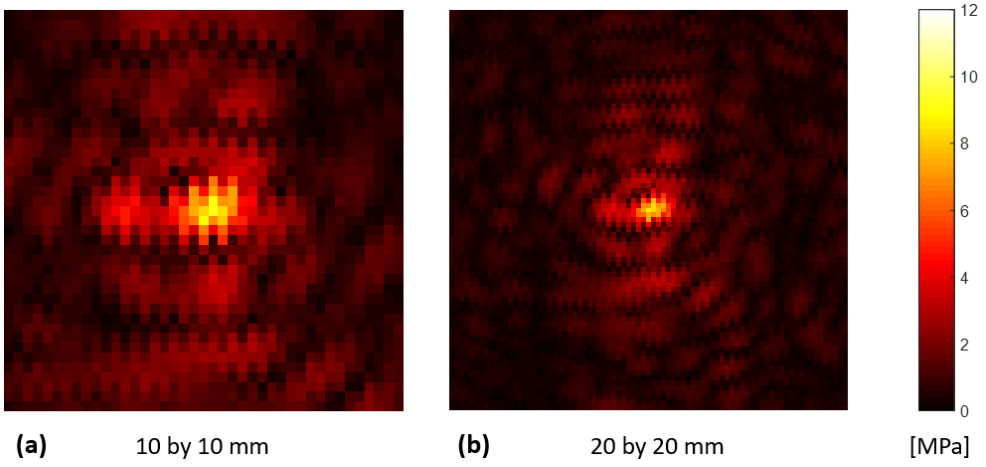

Fig. 5-6 Pressure field of focal plane measured using a hydrophone. Two different scanning scales were performed to define a feasible ROI size for a reasonable scanning time with enough coverage of the focal pattern.

Although a horizontal scanning on the XY plane is desirable, only XZ plane data were involved in following analysis and discussion. Vibration on the robotic arm while it was shifting to the next stop point during its scanning on XY plane, resulted in a fluctuating pattern on the pressure field as shown in Fig.5-6, Fig.5-6.a and Fig.5-6.b. The pressure pattern shown in the XZ plane scanning is much clearer and it does not contain any fluctuation pattern. A scanning window of 10 mm by 10 mm on XZ plane was performed on all of the hydrophone employed pressure measurements. As shown in Fig.5-7.b and Fig.5-7.d, the focal point is shifted away from the center after placing the skull between the transducer and the hydrophone. It should be noted that a low gain preamplifier setting was utilized for pre-scanning without skull and it was switched to high gain mode while scanning the pressure with the skull. It is known that the high gain mode has tenfold of amplification computed with the low gain mode. Thus, it is not appropriate to directly compare the scanned pressure in these two cases without correcting for the gain difference.

The simulated compensation phases (Fig.5-4) were saved as an ACT.INI file and loaded in the workstation software. As result, a sound velocity of 2750 m/s for refraction angle computation and 2150 m/s for travel time of refracted ray in skull bone produced the highest peak pressure with the best focal location (Fig.5-8). The sound waves emitted by each transducer element experiences the different aberration based on the specific path traversed by the beam through the skull. It is well known that the acoustical parameters of skull are varying as a function of location within the bone [7, 70]. It is therefore important to calculate the phase which can account for intra-skull heterogeneity and it may provide better representation of actual physical property of skull bone than using a homogenous property [42]. It is possible to develop a computation module based on the current software which could compute the phase based on skull heterogeneity from scanned CT image. Unfortunately, it seems infeasible to have additional experiments based on these new phase data. However, it will be carried out as a future study and the new update will be followed.

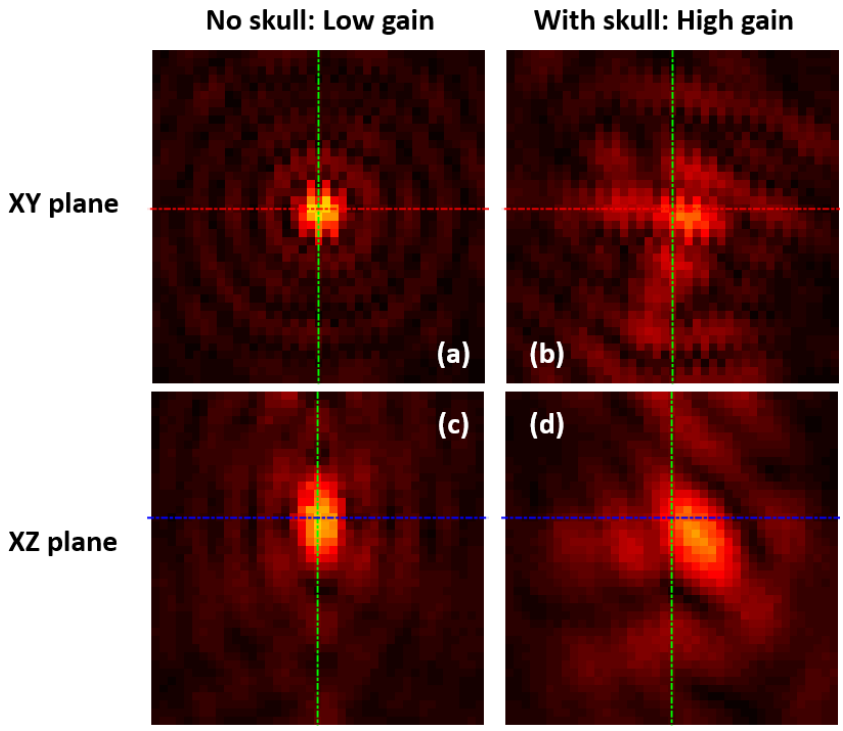

Fig. 5-7 The focal pressure measured on XY and XZ plane with and without skull placed between transducer and hydrophone. The scanning area is 10 mm by 10mm for all images. a) XY plane without skull b) XY plane with skull c) XZ plane without skull d) XZ plane with skull

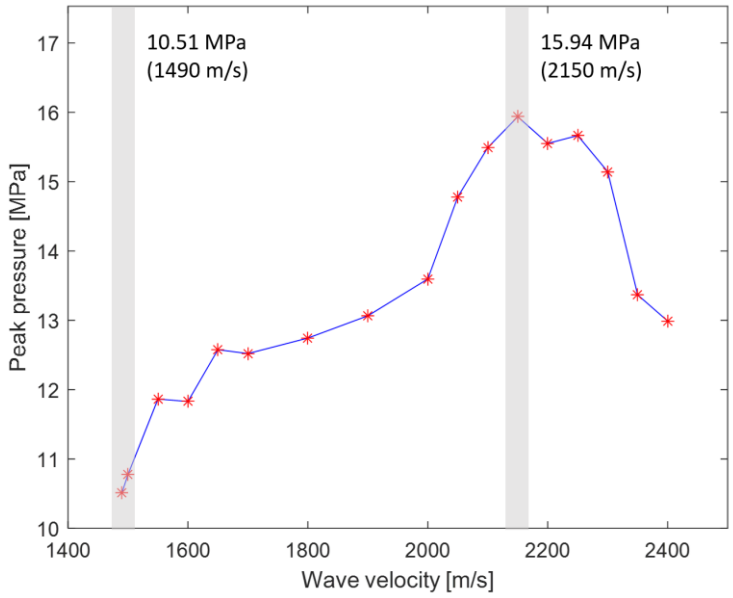

Fig. 5-8 A total of 17 sonication with hydrophone scanning were implemented on various speed of sound in bone for calculating phase delay.

Then, the comparison of phase correction with and without refraction accounted was performed on skull No.1 and the results were plotted in Fig.5-9. The phase correction without refraction was performed based on phase computation using a combination of 1482 m/s and 2150 m/s. The focal point was shifted away from geometrical focus (Fig.5-9.a) and both of these phase corrections were able to shift the focal point back to the targeting location (Fig.5-9.b and Fig.5-9.c). The ray tracing without refraction showed 12% improvement of focal pressure and a 48% improvement was achieved by refraction accounted phase correction. Apparently and theoretically, the refraction accounted ray tracing is more realistic.

Further verification experiments were implemented on both skulls in order to confirm if the refraction accounted ray tracing could provide a consistent improvement of focal location and peak pressure. Two experiments (Fig.5-10 and Fig.5-11) were implemented on both skulls and each of the experiment consumed about 5 to 6 hours for the preparation and data acquisition. The best case from various speed of sound in skull was compared with non-corrected case and plotted in Fig.5-10 and Fig.5-11.

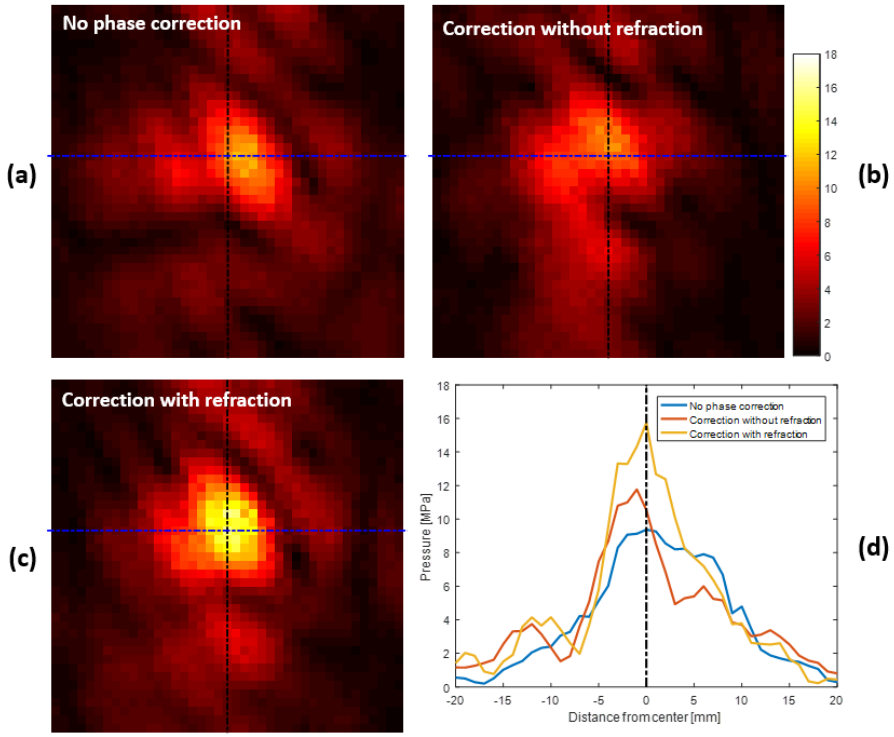

Fig. 5-9 The improved focal pressure by refraction accounted ray method in skull 1. a) Without phase correction b) Phase correction without refraction c) Correction with refraction accounted ray tracing d) The comparison of three cases. The pressure of three cases plotted in figure d were represent the pressure lies on the blue line from figure a, b and c.

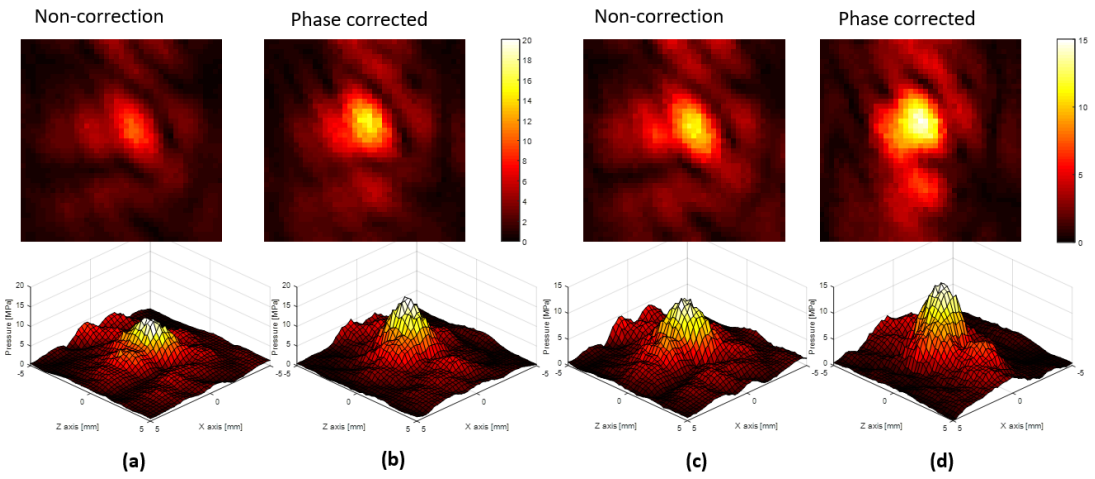

Fig. 5-10 The focal improvement using ray tracing based phase compensation on skull 1. A distinct focal pressure is visible although the skull placed in the transducer.

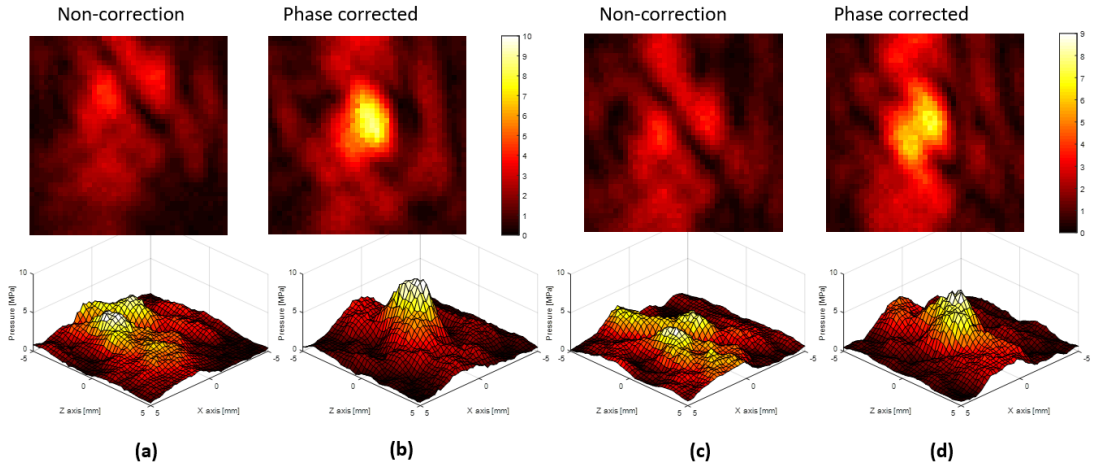

Fig. 5-11 The focal improvement using ray tracing based phase compensation on skull 2. A dispersed focal pressure distribution could be visualized in this skull setting.

A longer ray path in the skull 2 is refracted because of its greater skull thickness and this resulted in a stronger dispersal in focus than in skull 1. As the results are shown in Fig.5-12 and Fig.5-13, the focal points were all shifted back to the geometrical centers and the peak pressures were recovered on both skull compensation experiments. As shown in Fig.5-12, the peak pressure improvement on skull 1 was obtained as 55 % and 26 %, and it was even higher on skull 2, 112 % and 104 %. This obvious improvement on skull 2 is visible in Fig.5-12. Apparently, the ray based phase compensation improved the focal quality of TcFUS and produced a significant recovery (up to 112 % of improvement) of the peak pressure.

An incident angle, the angle between emitted beam from transducer element and the skull outer surface, is calculated based on Snell's law prior to the phase computation. The channel which experiences an incident angle greater than critical angle was treated as an ineffective channel and turned off during sonication. Theoretically, the angle above the critical angle is considered as total internal reflection and most of sound is reflected back to the incident medium. The nonlinearity and shear wave phenomena were out of scope in this study and a linear empirical approach was adopted. A correlation study on activated array channel number and increased focal pressure was carried out. As shown in Fig.5-13, a decreasing trend of improved pressure was followed relative to reduced active channel number on both skull experiments. A greater improvement of focal pressure was achieved on skull 2, which was sonicated with less activated channels. As aforementioned, a strongly refracted acoustic beam caused by skull 2 resulted in a blur focus with lower pressure at the focal point compared with the one by the skull 1. The lower base pressure would be the main reason why skull 2 has greater improvement of focal pressure. However, the direct comparison between two different skulls contains a controversy and more experiment data is desirable to address it more clearly.

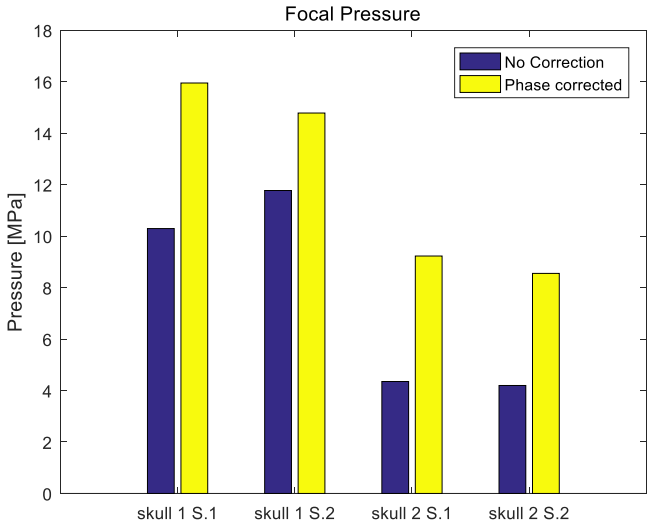

Fig. 5-12 The improved focal preassure compared with non-phase corrected case in both skull. A significant improvement of the focal peak pressure was obtained on skull 2. In contrast, the higher peak pressure was achieved in skull 1 phase compensation.

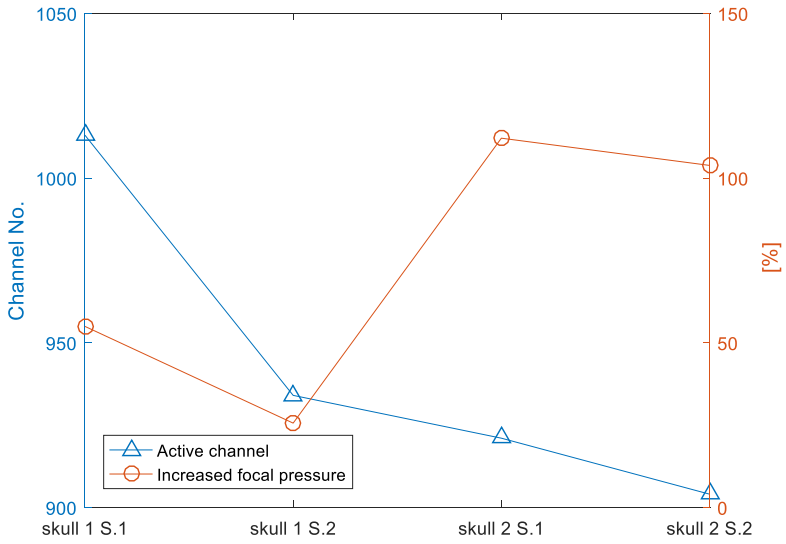

Fig. 5-13 The relation between activated channel number and the increased peak pressure. The decrease of focal pressred is in accord with the decrease of the activate channel in both skull measurement.

Chapter 6

LIMITATIONS

As a simplified algorithm, there are numerous limitations of this ray model. The assumptions of the transmitting plane wave from the linearized wave equation in fluid media could not accurately simulate the high power induced non-linearity. Since the linear wave equation was derived from a fluid media, it does not account any shear wave which is an important mean of wave propagation in the solid skull bone. This could be overcome by adding a shear model into the ray method. The speed of sound within the skull was defined as a homogeneous value. This may suffer from a large error range. The skull density derived from CT image is desirable in the future study to provide representative speed of sound traveling through the skull volume. The single ray representation of acoustic beam may result in a false refraction on the uneven and rough skull surface. By implementing a bundle of rays, it could filter out the influence from the roughness of skull surface and result in an averaged ray vector. Apparently, the improvement of focal pressure using our ray algorithm is notable. However, the focal pressure computation leaves a validation study to evaluate its accuracy. More sonication experiments are needed in the future study. For the validation of phase compensation accuracy, the hydrophone based gold standard phase correction was missing. It should be carried out in the future study to see how much energy is recovered by the ray method. Furthermore, additional phase correction experiments are desirable in order to verify the steering feature of the proposed algorithm.

Chapter 7

DISCUSSION AND CONCLUSION

7.1. Discussion

Our study was designed to develop an algorithm to rapidly compute the compensation phase in order to recover the skull induced aberration in a reasonable time frame. The algorithm developed in this study relied on several key components, including a GPU based visualization software, the CT based registration between the skull and ultrasound transducer, and the ray based plane wave model. One goal of the study was to simplify the calculations in order to expedite treatment process. Based on previous measurements with a single-element transducer, we tested a model that took skull thickness and density into account with sound refraction. Every sound beam of each transducer element refracted twice, on water-skull layer and skull-brain layer, until it propagated to the center of the brain. In our preliminary investigations, we observed a relatively large variation in the resulting focal pressure depending on sound speed. A series of experiments were implemented with iterative increasing speed of skull bone in order to acquire a representative value, although CT derived sound speed could potentially be a more elegant approach. The iterative experiment certainly obtains more optimal result than a single CT derived approximation. There is evidence that the CT based method [8] may not be accurate in all cases as simulation results were deviated in temperature by 34% compared to the observed data [73].

The configuration of the hardware-software registration introduced in chapter 2 enables the connection between our developed software to the clinical treatment system (InSightech Exablate 4000). The configuration provides valuable information to other researchers who are seeking to have a registration between their simulation tools to the hardware. Especially, the configuration figure could be served as reference data while doing animal experiment or

hydrophone employed scanning which requires a simple but accurate registration algorithm. It is encouraging that this software will be published as an open source project in the near feature. With the help of the flexible and expandable features of the developed software, various applicable research, such as testing a customized transducer, could be implemented by changing the modules or developing their own applications based on shared open source.

A practical trans-skull focusing algorithm should be able to correct the severe aberration caused by the skull. At the same time the numerical model must be computationally feasible to minimize the treatment planning time for the patient [74]. An empirical approach solving the planar propagation wave in a wave-vector-frequency domain achieved 52% improvement of focal pressure compare to the non-corrected case and the computation took 5 hours [74]. A FDTD based time reversal simulation study reported 90% recovery of the focal pressure with 2 hours of computation [75]. Recently, a phase correction study implanted in a hybrid angular spectrum method to compute the compensation phase took 45 min and it recovered 70% of pressure [73]. Apparently, the simulation model implementing a full-wave equation may provide the most accurate result, but it consumes even more computation time, e.g. 65 $\pm$ 3h, while simulating the full volume including the transducer, coupling water and patient head [76]. However, these do not seem to be practical for the clinical environment because of their long computation time. The ray tracing based method in this study recovers up to 112 percent of focal pressure when compared to non-corrected case with a real-time computation speed (less than 1 second). It does not provide the best scenario to compensate the focal pressure, but it can most likely be accepted in the practical environment which requires fast response feature. One of the feasible applications for this algorithm is the estimation of optimum transducer-patient placement after the target was defined. Although this approach may indicate limits based on its over simplification, it is noted that improved focus was still achieved at the targeted location.

The liquid-like media such as degassed coupling water and the brain tissue are expecting

to attenuate the signal through the path, but are not expected to be a major source of beam distortion [74, 77]. Thus, it is feasible to treat the water and the brain as homogeneous media on implemented water-skull-brain model with the measured attenuation coefficients. However, a strong scattering and attenuation feature of the skull bone should be paid additional attention. Since the bone consists of three distinct regions of inner and outer cortical bones and a central trabecular layer, the modeling of the skull may directly affect the simulation result. A single layer model of skull which does not account the internal refraction effects within the skull reported to achieve 52% higher focal pressure than non-corrected one [74]. In a following study from the same group, a three-layered model was compared to the single-layered model [72] and it was concluded that division into layers does not adequately improve the results over the single-layered model. Furthermore, the internal reflection is not expected to produce a major contribution to the overall phase, as studied in a previously reported experiment [12, 72]. Based on our experiment, the phase correction which incorporates refraction effects was focusing more energy to the center. The refraction model could provide realistic path information of the beam which directly influences the traveling time of the wave within the skull. Another key parameter affecting the traveling phase is the speed of sound in the skull bone. It was demonstrated [72] that CT-based models accounting for cranial heterogeneity were capable of better predicting the phase lags induced by the skull bone compared to both single- and three-layered models [78]. An empirical approach [69, 71, 72] to derive skull parameter from CT image is desirable to enhance the accuracy of the ray method in the future studies.

In most clinical applications, FUS transducers are excited at sinusoidal single frequency. If the resulting sound wave propagates linearly through tissue, then the focal pressure depends on the incident ultrasound intensity and the absorption coefficient locally. Several assumptions were required to treat the sound as a linear plane wave. The shape-amplitude proportionality principle states that the shape and amplitude of the acoustic waves at any location are

proportional to the input excitation, i.e., the source acoustic wave. The particle displacement generated by multiple acoustic sources assumed to be the algebraic sum of the displacements generated by each source, which in other words is called the superposition principle. The infinitesimal amplitudes principle states that the amplitude of the propagating wave is infinitesimally small [13]. The speed of sound in a medium, under the linear assumption, could be derived by $c = \sqrt{B/\rho}$, where B is the bulk modulus and ρ is the density. In fact, the speed and density in the above formula are the equilibrium sound speed and equilibrium density, meaning the speed and density of the medium in the absence of an acoustic wave [13]. This linearity principle is obeyed for low-pressure sonication. However, the nonlinear wave propagation and cavitation may occur under high-power sonication. When a large-amplitude single-frequency sound wave propagates through a nonlinear medium, the wave form becomes gradually shocked, resulting in the leakage of energy from the fundamental frequency into its higher harmonics [79]. The propagation speed of an acoustic wave in the nonlinear regime defined by $c = c_0 + \beta u$, where c_0 is the equilibrium speed of sound, β is called the nonlinearity coefficient, and u is the particle displacement velocity. The nonlinearity coefficient is defined as $\beta = 1 + 0.5\,B/A$ with B/A the nonlinearity parameter, an intrinsic property of each material or tissue [13]. In the context of HIFU, nonlinear effects become increasingly significant as the depth of treatment is increased, or if a region of high intensity happens to be coincident with a layer of fatty tissue [79]. The treatment for thermally ablate tissue in deep body requires relatively large sonication power to elevate the focal temperature to induce local necrosis. It is necessary to include the nonlinearity in order to fully simulate this phenomenon under high power sonication. From this perspective, the focal pressure estimation based on the proposed ray method seems not to be appropriate and requires further development in order to provide more realistic result under high power sonication. However, the clinical application, such as microbubble induced BBB opening, requires relative low energy to generate stable cavitation rather than thermally ablated target. In such a circumstance

that minimizes the nonlinearity, ray approach could find a place to implement as a reliable and fast simulation method. Another way to consider nonlinearity of high power is an empirical approach based on the measurements of pressure as a function of acoustic power. As shown in Fig.4-11, the pressure saturation over 2 W occurs for the single element transducer in the current clinical system and this saturation phenomenon is not explained yet, so that empirical results are now used for the clinical system. This empirical approach is an alternative at the moment.

The multiple reflections and standing waves may occur before the beam is fully absorbed by the brain tissue. The curved shape of the skull cavity may also act as a lens, refocusing of the beam at unwanted locations [80]. Several methods have been suggested to suppress standing waves in transcranial therapy. Hemispherical or large aperture arrays distribute the sound over a larger aperture and create a tight focus [81, 82]. Sweep frequencies have been used to reduce standing wave formation in vibroacoustography [83]. A small randomization in the frequency content of the signal for suppressing standing waves was introduced in reference [84]. In this study, the introduced ray method was not take account the standing wave and it desired to develop a model to simulate this effect in the future study. However, the phase correction algorithm may not suffer from standing wave effect.

The computation of transmission loss caused by skull was implemented as a single-layer model. Under this circumstance, one might expect that the transmission coefficient could be derived to a single formula instead of a separated model utilized as Eq. 4.2.11 and Eq. 4.2.12. The derived formula for comprehensive transmission coefficient may include a wave number term k and a ray length term l along normal axis of skull surface. In other words, the transmission coefficient may depend on the frequency and the skull thickness. However, the kl term in this study is approximately 10 which is much greater than 1. Furthermore, the attenuation loss caused by heterogeneous skull is not usually embedded in the comprehensive transmission coefficient formula and this may cause over simplication error. The simulation

of the pressure distribution inside of the skull along beam path by this approach may leave a bottleneck for the simulation such as shear wave and thermal distribution.

In clinics, the transducer channel that has an incident angle greater than the critical angle is treated as inactive channel during treatment. After manual registration by a surgeon who operates the TcMRgFUS treatment, the system turns off these channels. The number of active channel is directly related to the relative placement of the transducer and the patient. However, during treatment there is no available algorithm to predict an optimum transducer-patient placement to maximize the usage of the channels. It is reasonable to expect that the transmission amplitude is a function of the incident angle upon the skull surface [74]. Since the skull property is varying among patients, a rapid visualization tool could expect to be utilized to accelerate the treatment-planning time. One of the key features developed in this study is the fast visualization of 3D volume data with real-time method. An optimization loop combined to the developed fast ray software could be a method of choice to estimate an optimum transducer-skull placement.

7.2. Conclusion

This thesis examined the feasibility of ray-based phase correction on a clinical tcMRgFUS system. The objectives were to investigate the influence of the refraction to the phase correction, as well as to compensate the skull induced aberration using a ray method. The originality of the study can be summarized as follows:

- The registration between developed visualization software to clinical system. This expands the acceptability of this software.
- Ray accounting refraction effects provide more increased recovery of focal pressure than the non-refracted phase correction that was implemented in the current clinical system.

· The phase correction provides a real-time computation speed. This feature could be adopted into an iterative loop to estimate an optimum transducer patient setup.

The ray tracing based phase correction allow a better focusing of the focal spot as well as better recover of the peak pressure. Continuation of this work will focus on collecting more experiment data to evaluate the statistic performance of the proposed algorithm. The applicable future study is described in following section.

Chapter 8

THE FUTURE WORKS

Although this is an ongoing developing tool, there are various kinds of studies that could be applied based on the proposed ray-based software. First of all, it is possible to rapidly visualize the 3D CT and MRI volume data in the same domain. The refracted ray could be visualized in a real-time manner with different view angles and setting positions. This fast visualization feature of the software is feasible to utilize as a planning tool for experiments and even for patient treatments (Fig.8-1). The several ongoing researches based on this tool will be described in this section.

8.1. Skull density ratio computation for patient screening

It was reported that the skull density ratio (SDR) was positively correlated with maximal temperature in patient-specific and treatment-related data [85]. The SDR was defined as the ratio between the mean value in Hounsfield units for marrow and cortical bone [85]. The local density profile on the ray path through the skull segment was collected. The average ratios, SDR, between the trabecular and cortex CT value of the profile sample was derived from the density profile. However, the targeted location of the sonication was manually defined on CT image in 2D. The transducer geometry related to the CT skull was not considered and the ray used in the previous study was not employed for any transducer information. Furthermore, the refraction phenomenon was not considered so the accuracy of SDR may be suffered by over simplification.

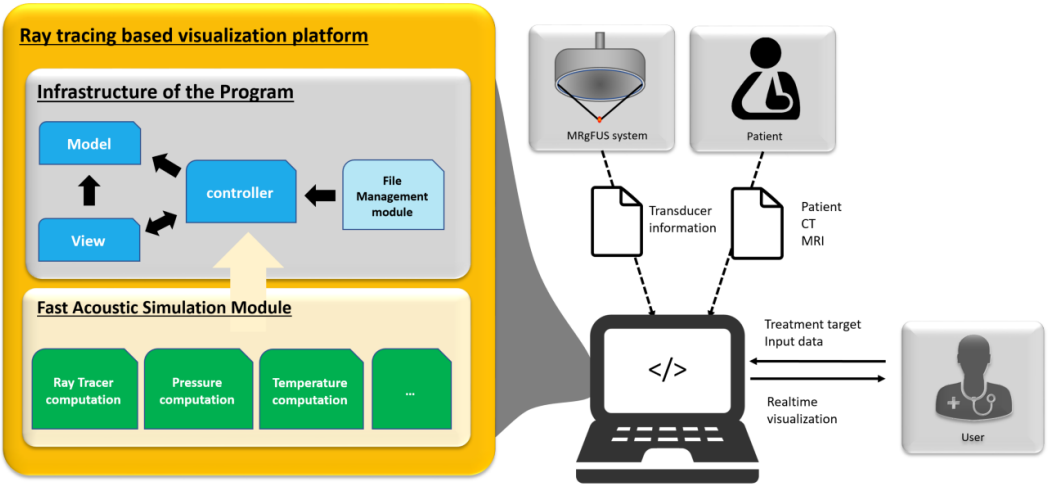

Fig. 8-1 The basic structure of ray tracing platform and the work flow of the developed software. It is feasible to extend the usage of the software to new designed researches by adding a functional module.

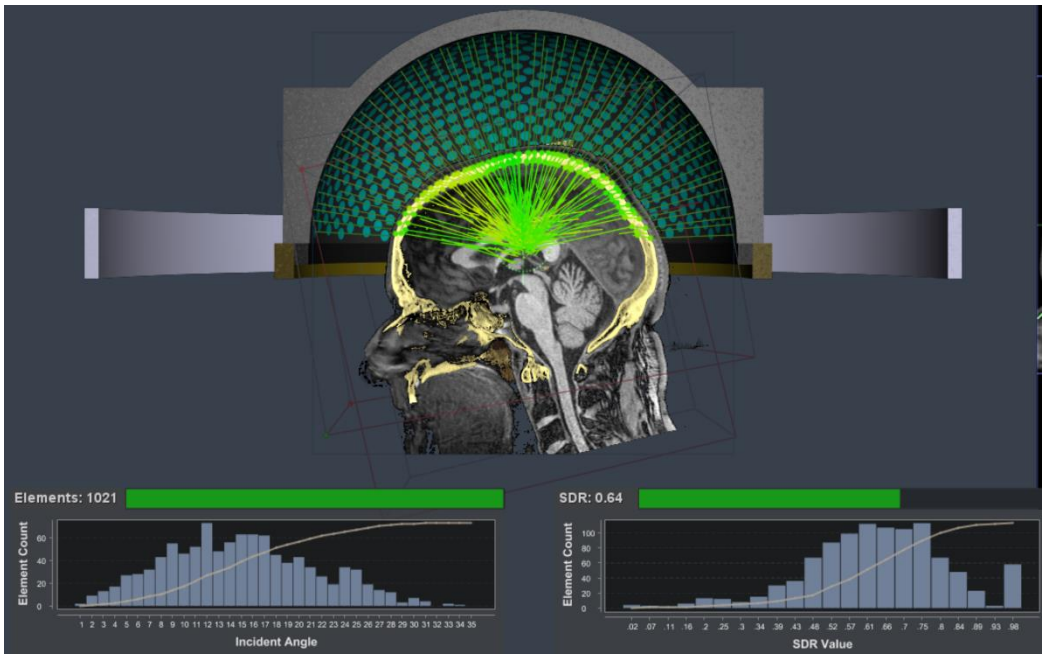

Fig. 8-2 The captured image from a graphical user interface of the developed ray tracing software. The activated transducer channel was plotted on the left bottom and the skull density ratio (SDR) was plotted on the right bottom. A varying channel number and SDR could be computed and visualized in real-time frame.

The refraction accounted ray model introduced in this study is able to calculate the SDR number in a 3D domain with real-time fashion. The ray emitted from each channel was transmitted through the skull and the skull density value was collected on each refracted ray segment lies in the skull bone. The final SDR was computed based on the skull density data as the previous study proposed [85]. As shown in Fig.8-2, the result could be illustrated in the developed software. The histogram of activated channel number and SDR number were illustrated at the bottom of the GUI. The total active channel number and the average SDR were also plotted.

It is desirable to derive the correlation between the achieved temperature ratio (the ratio between achieved temperature and targeted temperature) and SDR number based on patient specific treatment data. This study will be carried out in the future if the patient treatment data is available.

8.2. Patient screening and treatment planning tool

The longitudinal wave emitted from transducer is transmitted through the coupling medium and enters into the skull volume. The transmission coefficient for the longitudinal waves through a fluid-solid interface is dependent on the incidence angle of the insonifying wave [86]. For the incident angle beyond the critical angle, no longitudinal wave can be transmitted into the skull [87]. The sound wave of an incident angle greater than the critical angle will be converted to the transverse wave in the skull and back to longitudinal waves in the brain [87]. Therefore, the greater incident angle denotes a less transmission. Before loading a complicated full-wave simulation, a visualization tool with the incident angle on each channel is desirable and may provide a useful reference to the user for treatment planning. It is possible to visualize the activated channel comparing to the critical angle with the help of rapid computation feature of the developed software.

As shown in Fig.8-3 the skull CT from a patient could be evaluated using an incident angle mapping method. As the incident angle is indirectly representing the penetration ratio of the longitudinal wave, the color mapped incident angle could be used to pre-estimate the optimum transducer skull setup. The incident angle is highly dependent on the relative position between the ray and skull surface. It is possible to estimate an optimum transducer setting for targeted sonication location by running an iterative loop with varying position of transducer-skull setup. A statistical study on treated patient data to see the correlation between efficacy of ablated temperature and the incident angle distribution is desirable in the future study.

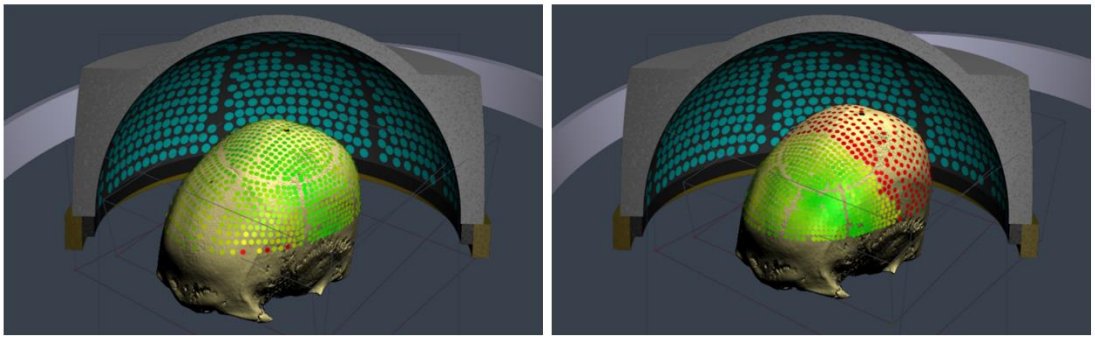

(a) (b)

Fig. 8-3 The mapping of the incident angle corresponding to each transducer. The incident angles equals or greater than the critical angle were mapped as red disks on the surface of skull where the ray intersects with the outer skull, and the incident angles under critical angle were plotted as green disks. A) The distribution of the incident angles when the sonication target lies on the center of the skull volume. B) The mapping of the incident angles when the sonication target lies on the postal side of the skull

8.3. Ellipsoidal shape FUS transducer design

Similar to the concept of the previous section, the number of activated channel could be calculated with the ray method. Obviously, the more channels were activated the higher energy get accumulated at the focus. An ellipsoidal transducer shape, which morphologically closer to the human skull, was designed and simulated to verify if this shape could improve the incident angles and increase the activated channels as well. The geometry of ellipse could be represented by following formula.

$$\frac{x^2}{a^2}+\frac{y^2}{b^2}+\frac{z^2}{c^2}=1$$

Where, the Cartesian coordinate of the points on the 3D ellipse was utilized. The ellipsoidal coefficient of each axis was defined as a, b and c. The ellipsoidal equation could be transformed to a sphere function when the value of a, b and c was equal. As shown in the previous figures, the hemisphere transducer, the transducer was defined as a hemisphere shape. Thus, the ellipsoidal shape could be transformed from a spherical shape by multiplying the corresponding axis ratios. The figure shown in Fig.8-4 represents the transformation of a spherical shape to ellipsoid shape. The ratio of axial coefficient between a sphere and ellipsoid was defined to 1:0.8 on X axis.

The activated channels which were defined based on incident angles are highly dependent on the relative location between the transducer and the skull placement. The activated channel number (ACN) could be collected at various transducer-skull setup by the moving transducer location. The color mapped ACN was plotted in the Fig.8-5. The CAN corresponding to the targeted location was mapped with color. The activated number above 700 was mapped with green volume and the value above 500 was mapped to yellow and the activated number below 300 was mapped as red color. A distribution which indirectly represents the efficiency of wave transmit could be estimated with this kind of visualization. Furthermore, a correlation study

based on patient treatment data to see the relation between the activated channel mapping (ACM) and the treatment efficiency is required.

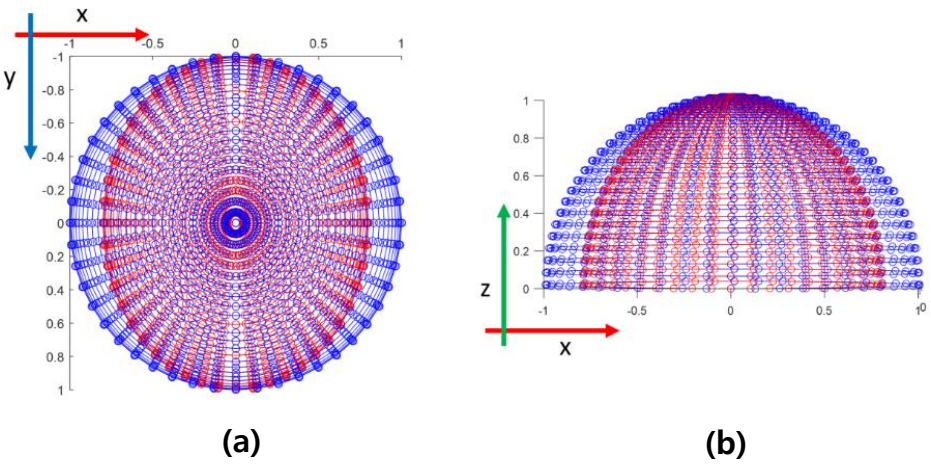

Fig. 8-4 The transformation of a sphere shape to ellipsoid one. A) The XY plane plot of the constructed 3D ellipsoidal shape with the original hemisphere B) The XZ plane plot of the constructed ellipsoid with the original hemisphere.

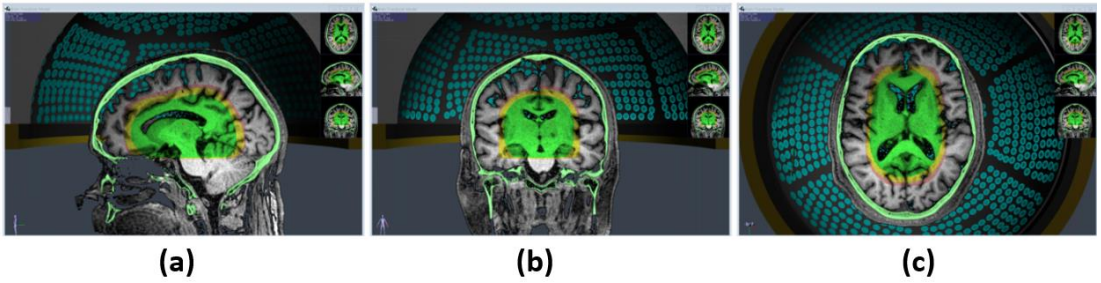

Fig. 8-5 The mapping of the incident angle corresponding to each transducer. The incident angles equals or greater than the critical angle were mapped as a red disk on the surface of skull where the ray intersects with the outer skull, and the incident angle

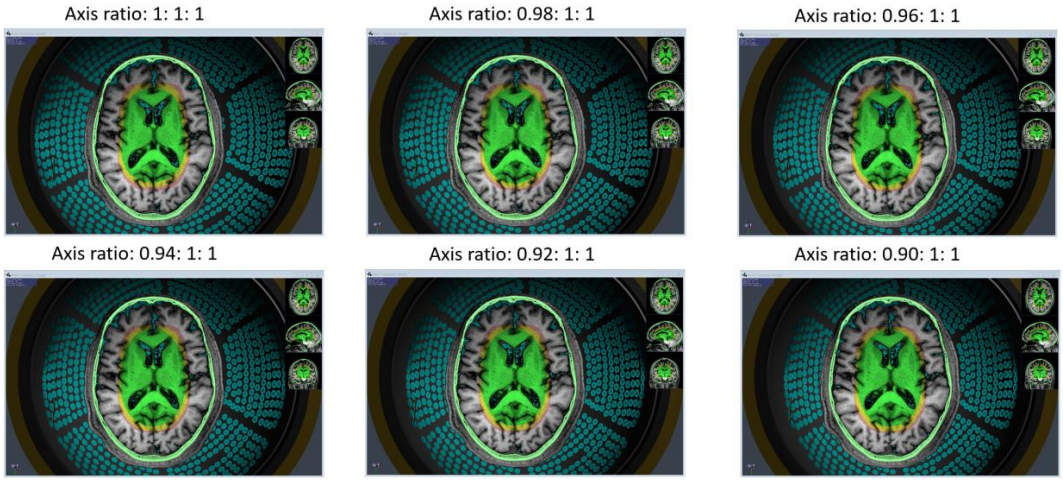

Fig. 8-6 The activated channel mapping of various ellipsoid shape. The axial ratio from 1 to 0.9 was utilized to design different ellipsoid transducer.

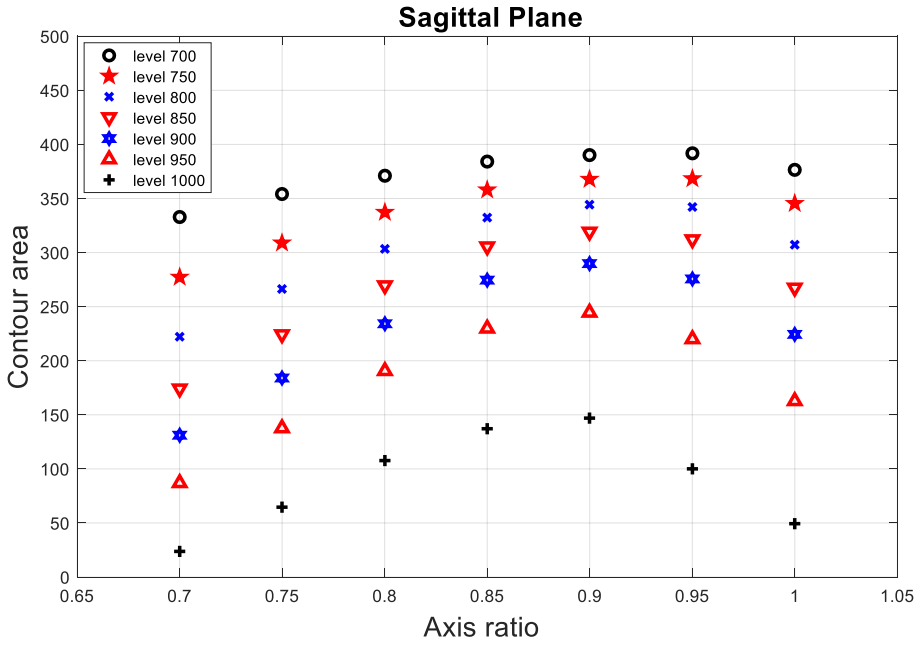

Fig. 8-7 The contour area ofdifferent contour levels in sagittal plane with the varying ellipsoid axis ratio.

The dependence of ACM distribution to the transducer shape was simulated. The ellipsoid transducer with different axial ratio was designed and the distribution of ACM was captured and illustrated in Fig.8-6.

The pixel area of the contour level was measured with different ellipsoid axis ratio to investigate that which ratio of the ACN has the maximum contour area. As the result shown in Fig.8-7, the contour area of all selected levels on sagittal plane has a peak area when the axis ratio was defined as 0.9.

The contour area was also investigated on the coronal plane (see Fig.8-8) and the transverse plane (see Fig.8-9). For the coronal case, the peak contour area was acquired when the axis ratio was 0.85. Similarly for the sagittal case the peak contour area was obtained with the axis ratio of 0.9. Apparently, the ellipsoid shape results in an improved ACN for the transmission efficacy. It is because of the skull shape used in this simulation was morphologically similar with an ellipsoid and this results in a relatively parallel plane between propagating wave and the skull surface. However, the variation of the skull shape from different subjects should be considered in future studies. More patient head CT data is required to analyze the dependence on the individual difference.

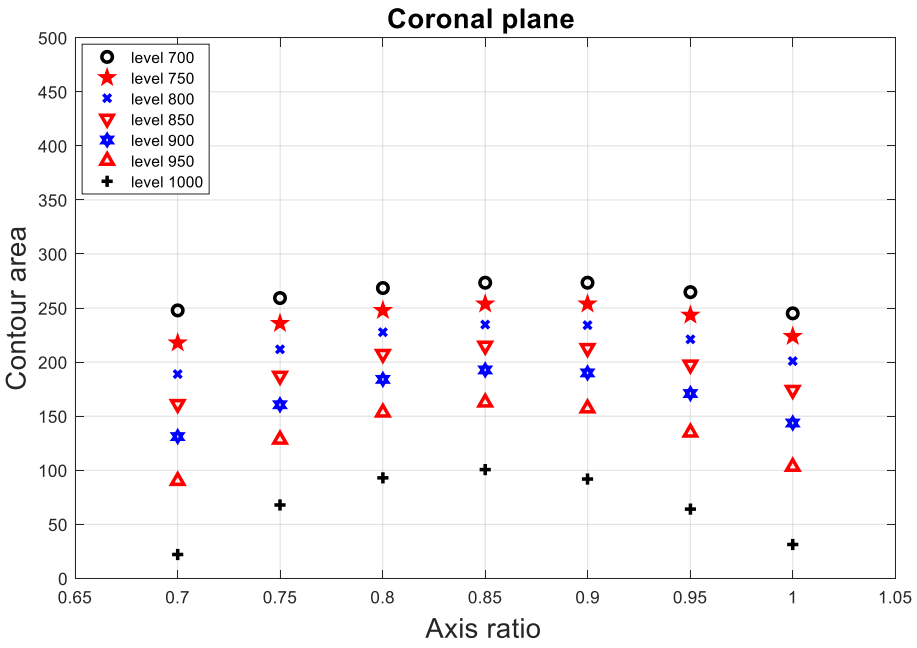

Fig. 8-8 The contour area of different contour levels in coronal plane with the varying ellipsoid axis ratio.

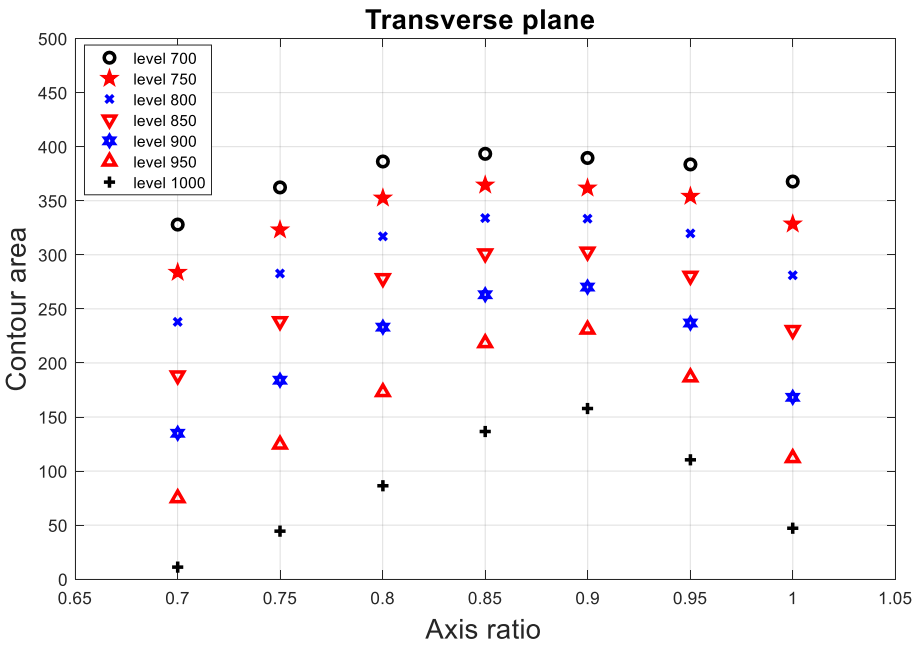

Fig. 8-9 The contour area of different contour levels in transverse plane with the varying ellipsoid axis ratio.

BIBLIOGRAPHY

[1] B. W. Stewart and C. P. Wild, *World Cancer Report 2014*. International Agency for Research on Cancer: IARC Press, 2014.

[2] P. Boyle and B. Levin, "World Cancer Report," *(World Health Organization Press, 2008),* 2008.

[3] J. S. Barnholtz-Sloan, A. E. Sloan, F. G. Davis, F. D. Vigneau, P. Lai, and R. E. Sawaya, "ncidence proportions of brain metastases in patients diagnosed (1973 to 2001) in the Metropolitan Detroit Cancer Surveillance System," *J Clin Oncol,* vol. 22, 2004.

[4] Y. Tsukada, A. Fouad, J. W. Pickren, and W. W. Lane, "Central nervous system metastasis from breast carcinoma. Autopsy study," *Cancer,* vol. 52, pp. 2349-54, Dec 15 1983.

[5] L. M. DeAngelis, J. Y. Delattre, and J. B. Posner, "Radiation-induced dementia in patients cured of brain metastases," *Neurology,* vol. 39, pp. 789-96, Jun 1989.

[6] E. L. Chang, J. S. Wefel, K. R. Hess, P. K. Allen, F. F. Lang, D. G. Kornguth*, et al.*, "Neurocognition in patients with brain metastases treated with radiosurgery or radiosurgery plus whole-brain irradiation: a randomised controlled trial," *Lancet Oncol,* vol. 10, pp. 1037-44, Nov 2009.

[7] F. J. Fry and J. E. Barger, "Acoustical properties of the human skull," *J Acoust Soc Am,* vol. 63, pp. 1576-90, May 1978.

[8] P. S., S. VW., and H. K., "Multi-frequency characterization of the speed of sound and attenuation coefficient for longitudinal transmission of freshly excised human skulls," *Phys Med Bio,* vol. 56, 2011.

[9] F. Padilla, E. Bossy, G. Haiat, F. Jenson, and P. Laugier, "Numerical simulation of wave propagation in cancellous bone," *Ultrasonics,* vol. 44 Suppl 1, pp. e239-43, Dec 22 2006.

[10] M. A. O´Reilly, "Methods for Focused Ultrasound-Induced Blood-Brain Barrier Disruption," *Publications of the University of Eastern Finland,* 2012.

[11] C. W. Connor and K. Hynynen, "Patterns of thermal deposition in the skull during transcranial focused ultrasound surgery," *IEEE Trans Biomed Eng,* vol. 51, pp. 1693-706, Oct 2004.

[12] G. T. Clement, J. Sun, and K. Hynynen, "The role of internal reflection in transskull phase distortion," *Ultrasonics,* vol. 39, pp. 109-13, Mar 2001.

[13] A. KYRIAKOU, "Multi-Physics Computational Modeling of Focused Ultrasound Therapies," *PhD thesis, University of Thrace,* 2015.

[14] X. Fan and K. Hynynen, "The effect of wave reflection and refraction at soft tissue interfaces during ultrasound hyperthermia treatments," *J Acoust Soc Am,* vol. 91,

1992.

[15] T. Kamakura, T. Ishiwata, and K. Matsuda, "Model equation for strongly focused finite-amplitude sound beams," *J Acoust Soc Am,* vol. 107, pp. 3035-46, Jun 2000.

[16] V. Nascov and C. Logofătu, "Fast computation algorithm for the Rayleigh–Sommerfeld diffraction formula using a type of scaled convolution," *Applied optics,* vol. 48, pp. 4310-4319, 2009.

[17] D. W. Herrin, T. W. Wu, and A. F. Seybert, "Case study evaluation of the Rayleigh integral method," *J Acoust Soc Am,* vol. 108, 2000.

[18] P. R. Stepanishen, "Pulsed transmit/receive response of ultrasonic piezoelectric transducers," *J Acoust Soc Am,* vol. 69, 1981.

[19] P. R. Stepanishen, "Transient radiation from pistons in an infinite planar baffle," *J Acoust Soc Am,* vol. 49, 1971.

[20] R. J. McGough, "Rapid calculations of time-harmonic nearfield pressures produced by rectangular pistons," *J Acoust Soc Am,* vol. 115, pp. 1934-41, May 2004.

[21] J. F. Kelly and R. J. McGough, "A time-space decomposition method for calculating the nearfield pressure generated by a pulsed circular piston," *IEEE Trans Ultrason Ferroelectr Freq Control,* vol. 53, pp. 1150-9, Jun 2006.

[22] D. Chen, J. F. Kelly, and R. J. McGough, "A fast near-field method for calculations of time-harmonic and transient pressures produced by triangular pistons," *J Acoust Soc Am,* vol. 120, pp. 2450-9, Nov 2006.

[23] J. W. Goodman, "Introduction to Fourier optics, 2nd edition," *Roberts & Company Publishers,* 2005.

[24] J. O. Erstad, "Design of sparse and non-equally spaced arrays for medical ultrasound," *PhD thesis, University of Oslo,* 1994.

[25] U. Vyas and D. Christensen, "Ultrasound beam simulations in inhomogeneous tissue geometries using the hybrid angular spectrum method," *IEEE Transactions on Ultrasonics, Ferroelectrics, and Frequency Control,* vol. 59, 2012.

[26] M. E. Schafer, P. A. Lewin, and J. M. Reid, "Propagation through inhomogeneous media using the angular spectrum method," *IEEE Ultrasonics Symposium,* 1987.

[27] M. E. Schafer and P. A. Lewin, "Transducer characterization using the angular spectrum method," *J Acoust Soc Am,* vol. 85, 1989.

[28] U. Vyas and D. Christensen, "Prediction of ultrasonic field propagation through layered media using the extended angular spectrum met," *J Acoust Soc Am,* vol. 130, 2011.

[29] T. D. Mast, L. M. Hinkelman, L. A. Metlay, M. J. Orr, and R. C. Waag, "Simulation of ultrasonic pulse propagation, distortion, and attenuation in the human chest wall," *J Acoust Soc Am,* vol. 106, pp. 3665-77, Dec 1999.

[30] S. Ginter, "Numerical simulation of ultrasound-thermotherapy combining nonlinear

wave propagation with broadband soft-tissue absorption," *Ultrasonics,* vol. 37, pp. 693-6, Jul 2000.

[31] S. Ginter, M. Liebler, E. Steiger, T. Dreyer, and R. E. Riedlinger, "Full-wave modeling of therapeutic ultrasound: nonlinear ultrasound propagation in ideal fluids," *J Acoust Soc Am,* vol. 111, pp. 2049-59, May 2002.

[32] R. N, N. R, and L. MC, "Efficient and accurate sound propagation using adaptive rectangular decomposition," *IEEE Trans Vis Comput Graph,* vol. 15, 2009.

[33] R. W. Graves, "Simulating seismic wave propagation in 3D elastic media using staggered-grid finite differences," *Seismological Society of America,* vol. 86, 1996.

[34] F. U. Foundation, "An Overview of the Biological Effects of Focused Ultrasound," *Focused Ultrasound Foundation's Website (www.fusfoundation.org),* 2015.

[35] M. S. W. J. Fry, J. W. H. Mosberg, W. Barnard, and M. S. F. J. Fry, "Production of Focal Destructive Lesions in the Central Nervous System With Ultrasound," *Journal of Neurosurgery,* vol. 11, p. 471, 1954.

[36] W. J. Fry and F. J. Fry, "Fundamental Neurological Research and Human Neurosurgery Using Intense Ultrasound," *IRE Transactions on Medical Electronics* vol. 7, 1960.

[37] A. Kyriakou, E. Neufeld, B. Werner, M. M. Paulides, G. Szekely, and N. Kuster, "A review of numerical and experimental compensation techniques for skull-induced phase aberrations in transcranial focused ultrasound," *Int J Hyperthermia,* vol. 30, pp. 36-46, Feb 2014.

[38] K. Hynynen and F. A. Jolesz, "Demonstration of potential noninvasive ultrasound brain therapy through an intact skull," *Ultrasound Med Biol,* vol. 24, pp. 275-83, Feb 1998.

[39] G. T. Clement and K. Hynynen, "Micro-receiver guided transcranial beam steering," *IEEE Trans Ultrason Ferroelectr Freq Control,* vol. 49, pp. 447-53, Apr 2002.

[40] K. Hynynen, G. T. Clement, N. McDannold, N. Vykhodtseva, R. King, P. J. White*, et al.*, "500-element ultrasound phased array system for noninvasive focal surgery of the brain: a preliminary rabbit study with ex vivo human skulls," *Magn Reson Med,* vol. 52, pp. 100-7, Jul 2004.

[41] J. Gateau, L. Marsac, M. Pernot, J. F. Aubry, M. Tanter, and M. Fink, "Transcranial ultrasonic therapy based on time reversal of acoustically induced cavitation bubble signature," *IEEE Trans Biomed Eng,* vol. 57, pp. 134-44, Jan 2010.

[42] G. T. Clement and K. Hynynen, "A non-invasive method for focusing ultrasound through the human skull," *Phys Med Biol,* vol. 47, pp. 1219-36, Apr 21 2002.

[43] G. T. Clement, P. J. White, and K. Hynynen, "Enhanced ultrasound transmission through the human skull using shear mode conversion," *J Acoust Soc Am,* vol. 115, pp. 1356-64, Mar 2004.

[44] N. McDannold and S. E. Maier, "Magnetic resonance acoustic radiation force imaging," *Med Phys,* vol. 35, pp. 3748-58, Aug 2008.

[45] B. Larrat, M. Pernot, G. Montaldo, M. Fink, and M. Tanter, "MR-guided adaptive focusing of ultrasound," *IEEE Trans Ultrason Ferroelectr Freq Control,* vol. 57, pp. 1734-7, Aug 2010.

[46] L. Marsac, D. Chauvet, B. Larrat, M. Pernot, B. Robert, M. Fink*, et al.*, "MR-guided adaptive focusing of therapeutic ultrasound beams in the human head," *Med Phys,* vol. 39, pp. 1141-9, Feb 2012.

[47] E. Martin and B. Werner, "Focused ultrasound surgery of the brain," *Curr Radiol Rep,* vol. 1, pp. 126-135, 2013.

[48] P. Ghanouni, K. B. Pauly, W. J. Elias, J. Henderson, J. Sheehan, S. Monteith*, et al.*, "Transcranial MR-Guided Focused Ultrasound: A Review of the Technology and Neuro Applications," *AJR Am J Roentgenol,* vol. 205, 2015.

[49] N. Lipsman, M. L. Schwartz, Y. Huang, L. Lee, T. Sankar, M. Chapman*, et al.*, "MR-guided focused ultrasound thalamotomy for essential tremor: a proof-of-concept study," *Lancet Neurol,* vol. 12, pp. 462-8, May 2013.

[50] W. S. C. e. al., "Factors associated with successful magnetic resonance–guided focused ultrasound treatment: efficiency of acoustic energy delivery through the skull," *J Neurosurg,* vol. 124, 2016.

[51] Banerjee, Sudipto, Roy, and Anindya, "Linear Algebra and Matrix Analysis for Statistics," *Texts in Statistical Science (1st ed.),* 2014.

[52] Trefethen, L. N. Trefethen, B. III, and David, "Numerical linear algebra," *Philadelphia: Society for Industrial and Applied Mathematics,* 1997.

[53] J. Snell and A. Quigg, "Visualization tools for transcranial Focused Ultrasound procedure planning, simulation and anlysis," *Focused Ultrasound Symposium,* vol. BR-24, 2016.

[54] S. Y. Byun, S. J. Byun, J. K. Lee, J. W. Kim, T. S. Lee, D. Sheen*, et al.*, "An efficient ray tracing algorithm for the simulation of light trapping effects in Si solar cells with textured surfaces," *J Nanosci Nanotechnol,* vol. 12, pp. 3224-7, Apr 2012.

[55] S. Y. Morita, Y. Nishidate, T. Nagata, Y. Yamagata, and C. Teodosiu, "Ray-tracing simulation method using piecewise quadratic interpolant for aspheric optical systems," *Appl Opt,* vol. 49, pp. 3442-51, Jun 20 2010.

[56] J. Koskela, E. Vahala, M. de Greef, L. P. Lafitte, and M. Ries, "Stochastic ray tracing for simulation of high intensity focal ultrasound therapy," *J Acoust Soc Am,* vol. 136, p. 1430, Sep 2014.

[57] S. Zucker and R. Hummel, "A 3-dimensional edge operator," *Proc. IEEE Conf. on Pattern Recognition and Image Proocessing,* 1979.

[58] F. B. Jensen, W. A. Kuperman, M. B. Porter, and H. Schmidt, "Computational Ocean

Acoustics," *Springer Science & Business Media,* 2011.

[59] K. B. Wolf, "Geometry and dynamics in refracting systems," *European Journal of Physics,* vol. 14, 1995.

[60] Rashed and Roshdi, "A pioneer in anaclastics: Ibn Sahl on burning mirrors and lenses," *Isis,* vol. 81, 1990.

[61] A. Schuster, "An Introduction to the Theory of Optics," *London: Edward Arnold,* 1904.

[62] J. D. Joannopoulos, S. Johnson, J. Winn, and R. Meade, "Photonic Crystals: Molding the Flow of Light," *Princeton NJ: Princeton University Press,* vol. ISBN 978-0-691-12456-8, 2008.

[63] Ghatak and Ajoy, "Optics (4th ed.)," *ISBN 0-07-338048-2,* 2009.

[64] L. E. KINSLER and P. FREY, "Fundamentals of acoustics," *J. Wiley Press,* 1962.

[65] J. ZEMANEK, "Beam behaviour within the nearfield of vibrating piston," *J Acoust Soc Am,* vol. 49, 1971.

[66] L. M. Brekhovskikh and O. Godin, "Acoustics of Layered Media II: Point Sources and Bounded Beams," *Springer Science & Business Media,* 2013.

[67] P. D. Nimrod M. Tole, "BASIC PHYSICS OF ULTRASONOGRAPHIC IMAGING " *Associate Professor of Medical Physics Department of Diagnostic Radiology* 2005.

[68] Krautkramer, J. a. Krautkramer, and Herbert, "Ultrasonic Testing of Materials, 4th - revised edition," *Springer Verlag,* 1990.

[69] G. Pinton, J. F. Aubry, E. Bossy, M. Muller, M. Pernot, and M. Tanter, "Attenuation, scattering, and absorption of ultrasound in the skull bone," *Med Phys,* vol. 39, pp. 299-307, Jan 2012.

[70] S. Pichardo, V. W. Sin, and K. Hynynen, "Multi-frequency characterization of the speed of sound and attenuation coefficient for longitudinal transmission of freshly excised human skulls," *Phys Med Biol,* vol. 56, pp. 219-50, Jan 07 2011.

[71] J. F. Aubry, M. Tanter, M. Pernot, J. L. Thomas, and M. Fink, "Experimental demonstration of noninvasive transskull adaptive focusing based on prior computed tomography scans," *J Acoust Soc Am,* vol. 113, pp. 84-93, Jan 2003.

[72] G. T. Clement and K. Hynynen, "Correlation of ultrasound phase with physical skull properties," *Ultrasound Med Biol,* vol. 28, pp. 617-24, May 2002.

[73] S. Almquist, D. L.Parker, and D. A. Christensen, "Rapid full-wave phase aberration correction method for transcranial high-intensity focused ultrasound therapies," *Journal of Therapeutic Ultrasound,* vol. 4, 2016.

[74] C. G.T. and K. Hynynen, "A non-invasive method for focusing ultrasound through the human skull," *Phys Med Biol,* vol. 47, 2002.

[75] F. Marquet, M. Pernot, J. F. Aubry, G. Montaldo, L. Marsac, M. Tanter*, et al.*, "Non-invasive transcranial ultrasound therapy based on a 3D CT scan: protocol validation

and in vitro results," *Phys Med Biol,* vol. 54, pp. 2597-613, May 07 2009.

[76] A. Pulkkinen, B. Werner, E. Martin, and K. Hynynen, "Numerical simulations of clinical focused ultrasound functional neurosurgery," *Phys Med Biol,* vol. 59, pp. 1679-700, Apr 07 2014.

[77] F. FJ and G. SA, "Further studies of the transkull transmission of an intense focused ultrasonic beam: lesion production at 500 kHz," *Ultrasound Med Biol,* vol. 6, 1980.

[78] R. M. Jones and K. Hynynen, "Comparison of analytical and numerical approaches for CT-based aberration correction in transcranial passive acoustic imaging," *Phys Med Biol,* vol. 61, pp. 23-36, Jan 07 2016.

[79] H. GT and C. C, "High intensity focused ultrasound: physical principles and devices.," *Int J Hyperthermia,* vol. 23, 2007.

[80] N. McDannold, E. J. Park, C. S. Mei, E. Zadicario, and F. Jolesz, "Evaluation of three-dimensional temperature distributions produced by a low-frequency transcranial focused ultrasound system within ex vivo human skulls," *IEEE Trans Ultrason Ferroelectr Freq Control,* vol. 57, pp. 1967-76, Sep 2010.

[81] S. J and H. K, "The potential of transskull ultrasound therapy and surgery using the maximum available skull surface area," *J Acoust Soc Am,* vol. 105(4), pp. 2519–2527, 1999.

[82] M. A. O'Reilly, Y. Huang, and K. Hynynen, "The impact of standing wave effects on transcranial focused ultrasound disruption of the blood-brain barrier in a rat model," *Phys Med Biol,* vol. 55, pp. 5251-67, Sep 21 2010.

[83] F. G. Mitri, J. F. Greenleaf, and M. Fatemi, "Chirp imaging vibro-acoustography for removing the ultrasound standing wave artifact," *IEEE Trans Med Imaging,* vol. 24, pp. 1249-55, Oct 2005.

[84] S. C. Tang and G. T. Clement, "Standing-wave suppression for transcranial ultrasound by random modulation," *IEEE Trans Biomed Eng,* vol. 57, pp. 203-5, Jan 2010.

[85] W. S. Chang, H. H. Jung, E. Zadicario, I. Rachmilevitch, T. Tlusty, S. Vitek*, et al.*, "Factors associated with successful magnetic resonance-guided focused ultrasound treatment: efficiency of acoustic energy delivery through the skull," *J Neurosurg,* vol. 124, pp. 411-6, Feb 2016.

[86] B. LM., "Plane wave reflection from the boundaries of solids. In: Waves in Layered Media. 2nd ed.," *NY: Academic Press,,* vol. chap 7, 1980.

[87] F. Vignon, W. T. Shi, X. Yin, T. Hoelscher, and J. E. Powers, "The stripe artifact in transcranial ultrasound imaging," *J Ultrasound Med,* vol. 29, pp. 1779-86, Dec 2010.

ACKNOWLEGEMENTS

아름다운 제주에서 박사과정을 마칠 수 있게 허락하신 하나님의 은총에 감사드리고 하나님께 영광을 드립니다. 그리고 많은 분들의 배려와 도움에 감사의 말씀 전합니다.

학자로서의 전문성과 겸손을 때론 동료처럼 때론 스승처럼 삶의 현장에서 가르쳐주신 팽동국 교수님께 감사드립니다. 논문 완성되기까지 조언을 아끼지 않으셨던 최민주 교수님, 조일형 교수님, 하강렬 교수님 그리고 박주영 박사님께 감사드립니다. 박사과정 많은 도움을 주셨던 배윤혁 교수님, 이종현 교수님, 배진호 교수님 그리고 남원호 박사에게 감사드립니다. 연구실에서 많은 시간을 함께 했던 복태훈 박사, 이재일 박사, 김주호 박사, 공치, 김정록 형, 김한수, 라기철, 현종우, 이혜빈, 김종화, 이기배, 민수홍에게 감사의 마음을 전합니다. 그리고 연구 시작하게 된 이민호, 이청아, 박병우, 최요한과 김수경 조교선생의 많은 도움이 있었습니다. 의공학 협동과정 강관석 형의 도움으로 많은 난제들을 쉽게 해결할 수 있었고 김성찬 선생의 도움에도 감사드립니다..

미국 버지니아에서의 연구를 후원해준 Focused Ultrasound Foundation 에 감사드립니다. 특별히 Neal Kassell, Tim Meakem, Rose Marry, Sarah Gray, Sarah White, Robin Jones, Anders Quigg 와 Kevin Zeng께 감사드립니다. 여러분의 도움으로 행정절차가 쉽게 진행되었고 더욱 연구에 집중할 수 있었습니다. 박사논문 주제 구상부터 실험과정을 줄곧 함께 해 왔던 John Snell, David Moore 과 Matt Eames에게 감사드립니다. 여러분을 통하여 소통하는 방법을 배웠고 연구에 대한 뜨거운 열정을 느끼게 해주셔서 감사합니다. 그리고 실험과 논문에 아낌없는 조언을 주었던 Jean-Francois Aubry과 Guillaume Maimbourg에게 감사드립니다. UVA물리학과 이승헌 교수님의 저택에 머무는 동안 교수님을 통하여 많은 것을 배웠고 진로상담 해주셔서 고맙습니다.

샬롯츠빌에 머무는 동안 많은 도움을 주었던 주병열 목사님, 강선미 집사님, 함흥식 집사님, 류지훈 집사님, 이용걸 교수님께 감사드립니다. 특별히 자주 초대해 주시고 맛있는 음식을 준비해 주신 이창순 목사님과 원미경 사모님께

감사드립니다. 진실된 나눔과 기도로 뜻깊은 시간을 보내게 된 샬롯츠빌교회 청년부 맴버들- 장재기, 류승헌, 김선우, 김현수, 지영준, 김기남, 이상윤, 김재순, 김한중, 서상원, 이창섭, 장승익, 구슬아, 주하랑 과 진미화에게 감사드립니다.

그동안 많이 의지했던 성안교회 중국어 예배부 가족들에게 감사드립니다. 특별히 오철송 목사님과 사모님의 보살핌에 낯선 외국에서의 생활에 많은 도움이 되었습니다. 그리고 함께 동역자로 섬겨왔던 엄재균 집사님, 설은영 집사님, 박미선 사모님, 김소현 집사님, 오명화, 왕징징, 정슨성, 임단이, 경림원과 주학에게 감사드립니다. 힘들고 지칠 때마다 떠오르는 YUST의 강위훈 교수님, 강성택 교수님, 문규성 교수님, 문용찬 교수님, 이대영 교수님, 정용호 교수님, 최재헌 교수님, 김영석 교수님, 조현직 교수님 그리고 Martin Groß에게 감사의 말씀 전합니다. 교수님들을 통해 보았던 비젼과 느꼈던 사랑이 지금도 저에겐 큰 힘이 되고 위로가 되고 있습니다. 오랜 친구 귀상다길과 리호, 든든한 후배 김문권 그리고 저의 많은 고민을 경청해 주었던 배국화에게 감사의 마음 전합니다.

마지막으로 한없이 부족한 저에게 인간됨의 진리를 가르쳐주신 아버님, 철없는 아들을 사랑과 헌신으로 키워주신 어머님, 누구보다 저를 이해해주고 묵묵히 응원해주었던 우리 누나에게 가장 큰 감사의 마음을 전합니다. 부족하지만 최선을 다한 이 논문을 바칩니다.

2017 년 6월

김창수